Physik-Department

Institut für Experimentalphysik E12

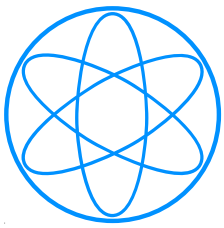

The Doppler Shift Attenuation Method Facility: Its Design, Setup and Commissioning with the ^{32}S(^{3}He,^{4}He)^{31}S Reaction

Dissertation

von

Clemens Herlitzius

Technische Universität

München

Technische Universität München
Fakultät für Physik
Lehrstuhl für Experimentalphysik E12

The Doppler Shift Attenuation Method Facility: Its Design, Setup and Commissioning with the ^{32}S(^{3}He,^{4}He)^{31}S Reaction

Clemens Herlitzius

Vollständiger Abdruck der von der Fakultät für Physik der Technischen Universität München zur Erlangung des akademischen Grades eines

Doktors der Naturwissenschaften

genehmigten Dissertation.

Vorsitzende(r):		Univ.-Prof. Dr. Norbert Kaiser
Prüfer der Dissertation:	1.	Univ.-Prof. Shawn Bishop, Ph.D.
	2.	Univ.-Prof. Dr. Stephan Schönert

Die Dissertation wurde am 27.05.2013 bei der Technischen Universität München eingereicht und durch die Fakultät für Physik am 19.07.2013 angenommen.

Abstract

The focus of this thesis lies on the design and the setup of a new experimental installation for lifetime measurements of excited states in nuclei. The setup has been installed at the Maier-Leibnitz Laboratory in Garching and employs the Doppler shift attenuation method (DSAM). The DSAM is a technique to measure the mean lifetime τ of an excited state in nuclei ranging between 10^{-15} and 10^{-12} s, before a de-excitation via γ-ray emission takes place.

Classical nova events will be chosen to highlight the importance of resonant proton capture reactions for the synthesis of specific nuclei in our universe. The rates of those reactions are important to quote reliable estimations for the composition of the ejected material and to understand the interior mechanisms driving such an event. Therefore, direct and indirect measurements in laboratories are employed to determine resonant reaction rates. These resonant rates are inversely proportional to the lifetimes of the excited states formed by the radiative capture of proton on a reactant nucleus. Those lifetimes can be determined with the method and the setup described in this thesis.

As a proof of principle of the new setup, the lifetime of the first excited state (3/2+, 1248.9 keV) in ^{31}S was determined to be $\tau = (964 \pm 19(\text{stat.})^{+311}_{-89}(\text{syst.}))$ fs.

Contents

Chapter 1

Introduction

Some of the key questions in nuclear astrophysics are how and where elements in the universe are synthesized. Figure 1.1 shows the observed present-day solar elemental abundance as a function of the atomic number and normalized to Si [Lod03]. One of these key questions is: which processes and environments are necessary to explain the observed chemical abundances? The zigzag pattern in the dependence of the atomic abundance on the atomic number in Figure 1.1 can be explained by the nuclear pairing force. The iron peak can be explained by the binding energy per nucleon as a function of the mass number, which is shown in Figure 1.2. It has a maximum for ^{56}Fe and ^{62}Ni and therefore the maximum energy per nucleon is released by their production resulting in the most stable nuclei. It becomes clear that nuclear reactions and nuclear structures are important for the comprehension of the production of the elements.

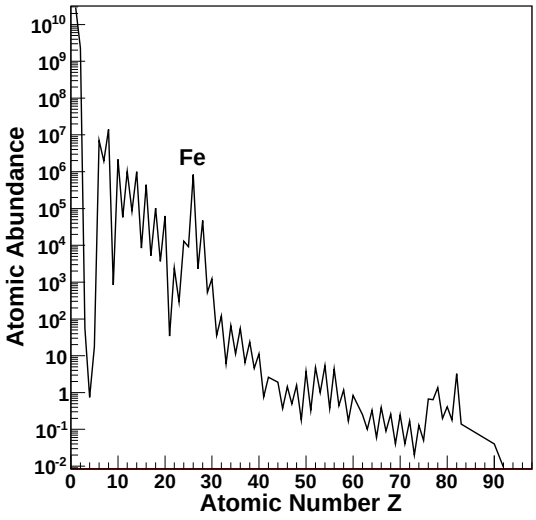

Figure 1.1: The solar atomic abundance as a function of the atomic number Z [Lod03], normalized to Si ($\equiv 10^6$). The points are connected with lines to guide the eye.

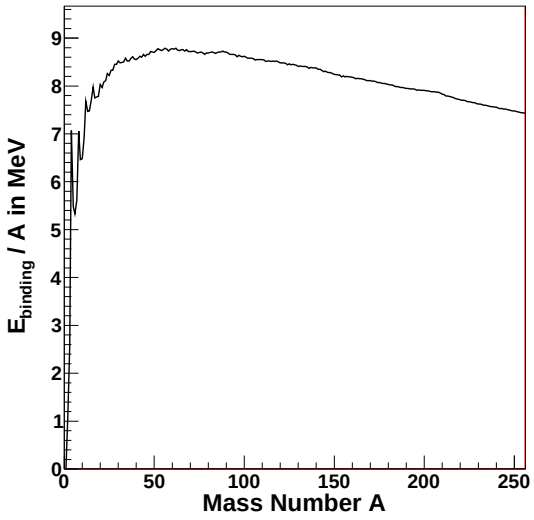

Figure 1.2: The binding energy per nucleon as a function of the nucleus' mass number A [Aud03b]. There are maxima for ^{56}Fe and ^{62}Ni. The maximum change is observed between $A = 1$ and $A = 4$.

The theory of the big bang nucleosynthesis (BBN) only explains the production of ^{1,2}H, ^{3,4}He and small amounts of Li but not heavier elements. Beyond BBN, the essential mechanisms for the production of heavier elements were identified in seminal works of [Bur57] and [Cam57]. Observations and theoretical models agree that the locations in the universe where metals (number of nucleons A $\geqslant$ 4) can be synthesized sufficiently are within various stellar environments. One such environment in which new nuclei heavier than those produced in BBN are produced is within classical nova events, which will be described in section 1.4.

1.1 The Stellar Evolution

Stars are formed, when interstellar gas clouds, mostly made up of hydrogen and helium, contract due to the gravitational force. Initially, the released gravitational potential energy is transformed to radiation and is mostly radiated to interstellar space. With more and more material accumulated, the opacity increases and the matter heats up due to the trapping of radiation [Rol88]. First nuclear reactions of light particles such as deuterium burning starts to occur for masses $M \gtrsim 0.013\ M_{\odot}$, with the solar mass $M_{\odot}$ [Ili06].

An observed star can be classified by plotting its luminosity versus the surface temperature T_{eff}, which defines the color or the spectral class of the star. The so called Hertzsprung-Russel diagram (HRD) in Figure 1.3 shows this in a snap-shot of many stars at the same time [Pow06]. Since the star's luminosity and the surface temperature change with its evolution, the position of a single star moves within the HRD during the star's lifetime. Therefore, it is possible to draw conclusions on the processes within a star from its position in the HRD.

Most of the stars are mapped in the HRD in the so called main sequence (see Figure 1.3) and undergo hydrogen burning but differ in their initial masses. Because of the main sequence mass-luminosity ($M-L$) relation, where $L \propto M^{3.5-4.0}$ [Cla83], the time evolution of such a star is very sensitive to its mass. Therefore the star's lifetime can be estimated to be $T_{\rm star} = 12 \cdot (L/L_{\odot})^{-3/4}\ 10^9$ years [Cla83]. A mass of at least M = 0.08 $M_{\odot}$ is necessary to provide enough thermal energy in the star's core to fuse protons to helium via the so called pp chain (net reaction: 4p $\longrightarrow^4$ He$+2e^+ +2\nu_e+$26.731 MeV). Hydrogen burning is the longest time period in the evolution of a star and releases the maximum energy per nucleon (see Figure 1.2), compared to the fusion of heavier nuclei in advanced burning sequence that will be described in the following. The released energy from nuclear reactions during the different burning stages provides the heat necessary to create enough pressure in the star's core to counter gravitational contraction.

The ash (^{4}He) accumulates at the core and the hydrogen burning stops, after the fuel (protons) is exhausted at radii in the star, where the temperature is sufficient. Since then no nuclear energy production counteracts the gravitational pressure anymore, the star contracts and the core temperature rises. If the initial mass of the star is $M \gtrsim 0.4 M_{\odot}$ the core temperature will be sufficient for the next burning stage, the

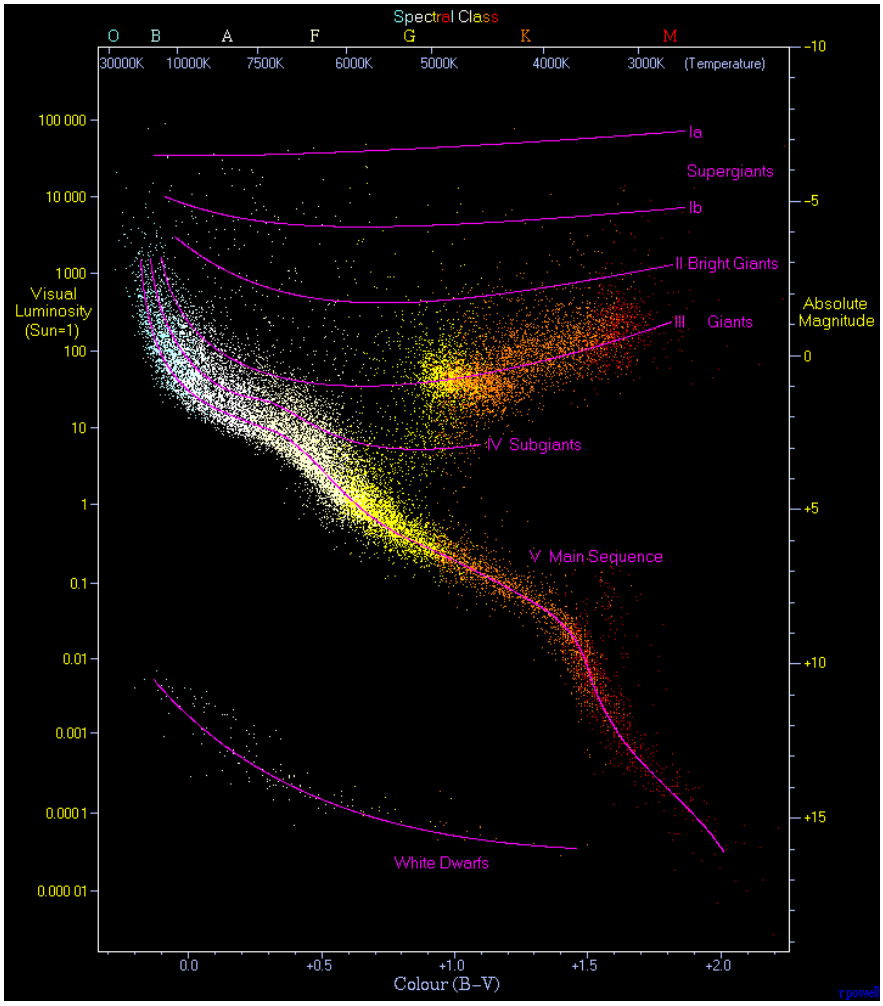

Figure 1.3: Observed luminosity and color (surface temperature) of stars in the Hertzsprung-Russel diagram (from [Pow06]).

helium burning of ^{4}He to ^{12}C.

Helium burning must pass through a bottle neck of stability in the chart of nuclei, because there is no stable nuclide with $A = 5$ and $A = 8$. Since the half-life of ^{8}Be is only $6.7 \cdot 10^{-17}$ s [Aud03a], the fusion $^4\text{He} + ^4\text{He} + 92$ keV $\leftrightarrow ^8$ Be can only be an intermediate step. With an efficient reaction rate, an equilibrium of fusion and disintegration will establish a sufficient amount of ^{8}Be to capture another ^{4}He and produce the stable ^{12}C. It turns out that this mechanism only can be efficient if the second reaction proceeds via a s-wave resonance in ^{12}C (met at $T_9 = 0.2$). This resonance has been predicted theoretically and could be verified experimentally [Dun53, Sal52].

Within the carbon burning stage, successive ^{4}He captures on the produced ^{12}C up to ^{24}Mg are possible at temperatures $T_9 = 0.1 - 0.4$. Nevertheless, the $^{12}\text{C}(^4\text{He}, \gamma)^{16}\text{O}$ reaction is slow compared to the $^4\text{He}(^4\text{He}\ ^4\text{He}, \gamma)^{12}\text{C}$ reaction and therefore many ^{12}C

remain after the ^{4}He is exhausted. The core then mainly consists of ^{12}C and ^{16}O and becomes a O/Ne white dwarf, it the next burning sequence is not triggered.

Again, the star contracts and suppose the star's mass is $M \gtrsim 9M_\odot$, the next burning sequence, carbon burning, starts via $^{12}\mathrm{C} + ^{12}\mathrm{C}$ and produces highly excited ^{24}Mg compound nuclei that emit protons, ^{4}He particles or neutrons, creating ^{23}Na, ^{20}Ne or ^{23}Mg, respectively [Hoy54], while the emitted particles are captured by other nuclei e.g. ^{12}C producing ^{16}O. At the end of this burning stage, the core mainly consists of ^{16}O, ^{20}Ne, ^{23}Na and ^{24}Mg and becomes a O/Ne (Mg) white dwarf, if the next burning sequence is not triggered.

If the star's mass is $M \gtrsim 11M_\odot$, the core temperature after contraction will be sufficient to produce energy in the Neon burning sequence, where the photodisintegration of ^{20}Ne becomes a major source of ^{4}He particles, which are captured in secondary reactions such as $^{20}\mathrm{Ne}(^4\mathrm{He},\gamma)^{24}\mathrm{Mg}(^4\mathrm{He},\gamma)^{28}\mathrm{Si}$ or $^{23}\mathrm{Na}(^4\mathrm{He},\mathrm{p})^{26}\mathrm{Mg}(^4\mathrm{He},\mathrm{n})^{29}\mathrm{Si}$. At the end of this burning stage, the core mainly consists of ^{16}O, ^{24}Mg and ^{28}Si.

The next burning stage is Oxygen burning and due to the increased temperature and the relatively low Coulomb barrier of ^{16}O, direct $^{16}\mathrm{O} + ^{16}\mathrm{O}$ fusion is possible. The excitation energy of the compound nucleus ^{32}S is high (16.5 MeV) and is far above the separation energy of light particles as n, p, d, ^{4}He, which are again captured in secondary reactions. The core accumulates mainly ^{28}Si and ^{32}S.

In the last burning sequence, the Silicon burning, direct fusion is not possible due to the high Coulomb barriers of ^{28}Si and ^{32}S. Instead, less stable (lighter) nuclei from previous burning stages are photodisintegrated, creating a source of light particles (such as ^{4}He particles) that can fuse with heavier nuclei successive up to nuclei in the iron region. This process is called photodisintegration rearrangement. Nuclei in the Fe region are very stable because of their maximum binding energies (see Figure 1.2). This explains the iron peak in solar atomic abundance shown in Figure 1.1 and is the end of exothermic fusion reactions.

The described burning sequences are explained in detail in [Ili06, Rol88, Cla83]. If a star's mass is not high enough to rise the temperature in its core during the contraction after a previous burning stage, the next burning sequence can not be triggered and the star's evolution ends, leaving a very dense core with the elemental composition that was built up in its last burning sequence, which is predetermined by the star's initial mass. The star finally cools via radiation and it is positioned in the HRD in the lower left. During the burning phases, huge amounts of mass is ejected and for initial star masses of $M < 11M_\odot$, the remnant mass is usually smaller than the so called Chandrasekhar limit $M \lesssim 1.44\ M_\odot$ and an equilibrium between the electron degeneracy pressure and the gravitational pressure is established, forming white dwarfs. If the remnant mass is larger, the core contracts even more and a supernova will succeed.

1.2 The Production of Heavy Chemical Elements

Starting with nuclei in the iron group, all fusion reactions producing heavier nuclei are endothermic, because the binding energy per nucleon decreases with the number of

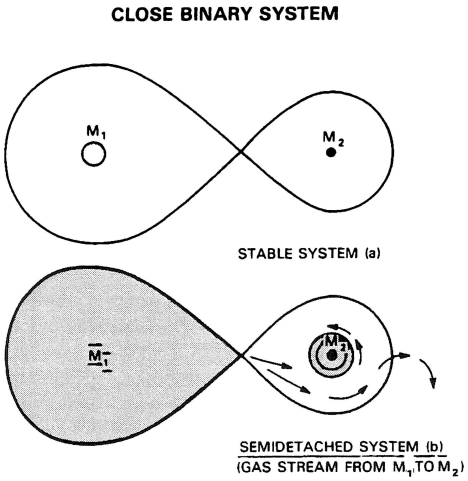

Figure 1.4: Roche lobe surface of a binary star system (from [Rol88]). The knot on the line between the stars is called inner Lagrangian point, where the centrifugal and the gravitational forces of both stars cancel.

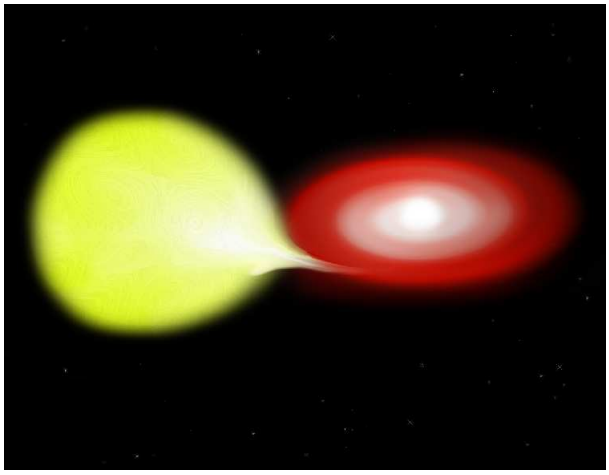

Figure 1.5: Artist illustration of a binary star system (from [MW01]). Hydrogen rich matter is transformed from the main sequence star or red giant on the left to the white dwarf on the right.

nucleons (see Figure 1.2). Therefore, these elements ($A \gtrsim 60$) can only be synthesized in environments of extreme temperatures and densities that provide the required energy. Due to the rising Coulomb barrier of heavy isotopes, fusion of charged particles becomes less efficient, but neutron capture processes creating very neutron rich nuclei with subsequent β^- decay can bypass this limitation [Bur57]. The theories of the rapid (r-) and the slow (s-) neutron capture processes describe mechanisms where the neutron capture rate is much higher than the β decay rate (r-process) and vice versa (s-process). This results in in the production of nuclei far away from the valley of stability on the neutron rich side (r-process) and relatively close to the stability (s-process) while the extreme conditions are present. Such environments are assumed to be found in supernovae [Sne03]. The produced n-rich nuclei decay back to the valley of stability, after the extreme conditions and neutron densities vanish. Detailed descriptions of possible environments where these mechanisms take place are complicated and are still subjects of active current research [H.-07, Ham10].

1.3 The Binary Star Systems

Estimations suggest that a notable fraction (this fraction is still discussed but could be $\sim 30\%$) of all stars in our galaxy are part of binary star systems [Lad06].

Both stars of such a system with the masses M_1 and M_2 have gravitational fields that overlap with each other as shown in Figure 1.4. The so called Lagrangian point is defined between the stars, where both gravitational and rotational forces cancel. Due

to the centrifugal acceleration, the two stars are enclosed by a barbell-like potential surface, called Roche lobe surface. If material passes through the inner Lagrangian point (e.g. due to evolutionary expansion of the star), the material's gravitational binding to its previous host star is lost and it can be transferred to the compound star [Rol88]. This is illustrated in Figure 1.5 [MW01]. This mechanism allows the transfer of hydrogen-rich material from the outer envelope of the companion star, which is the requirement for events such as classical novae that are described in the next section.

1.4 Classical Novae

The observation of a nova event in 1934 suggested an eclipsing binary star system [Wal54]. In the fifties, the idea became accepted that nova outbursts in general are caused by a hydrogen rich mass transfer in binary star systems [Sch96].

Classical nova events occur in binary star systems, composed of a white dwarf and a main sequence star or red giant. As previously described in section 1.1, a white dwarf is a star that has reached its evolutionary end and its mass is not sufficient to create core temperatures that allow fusion beyond C/O ("lighter white dwarfs" with $M \lesssim 1.1\ M_{\odot}$) or O/Ne ("massive white dwarfs" with $M \gtrsim 1.1\ M_{\odot}$) [Jos07]. Nevertheless, hydrogen rich material can be transformed from the main sequence compound star (or red giant) to the white dwarf by the mechanism described in the previous section and eventually settles on the surface with high velocities; mixing with helium and dredged up C/O or O/Ne from the white dwarf's core. Due to the white dwarf's gravitational potential, the density and the pressure on its surface are high ($\rho = 600 - 900$ g/cm^3 [Ili06]) and therefore the electrons behave like a degenerate gas. As soon as the density (and the temperature) of the accumulated hydrogen is sufficient, hydrogen burning via pp chain will take place resulting in an energy release and hence a rise in temperature. Due to the degeneracy, no expansion and therefore no cooling is possible.

The energy production rate of non resonant reactions is proportional to $\mathrm{T}^{n(T)}$ with $n = 1.26$ and $n = 67.91$ (for $T = 200$ MK [Ili06]) for the pp chain and the CNO cycle, respectively. When the temperature rises enough to initiate the CNO cycle, the temperature will rise even faster and finally, the released energy will overcome the degeneracy, because the electrons are lifted to higher states by Compton scattering with γ-rays. An abrupt explosion of the surface layers then causes the ejection of the envelope of the white dwarf. The rates of resonant (p, γ) rates on dredged up nuclei from the core rates are driven up by orders of magnitudes at this point and therefore contribute considerable to the energy production. The binary star system is not disrupted and the process actually can reoccur (with time periods in the order $10^4 - 10^5$ years) when the hydrogen accretion rate is small. Typical accretion rates are $10^{-9} - 10^{-10}\mathrm{M}_{\odot}$/year [Jos07].

Roughly 35 ± 11 nova events per year are predicted in our galaxy, but only about 5 novae per year are being discovered [Sha97] because of the extinction of the emitted light, along the line of sight, caused by the dust within the arms of our galaxy. Figure 1.6 shows a photo of the nova Cygni as observed in 1992 with the Hubble Space telescope

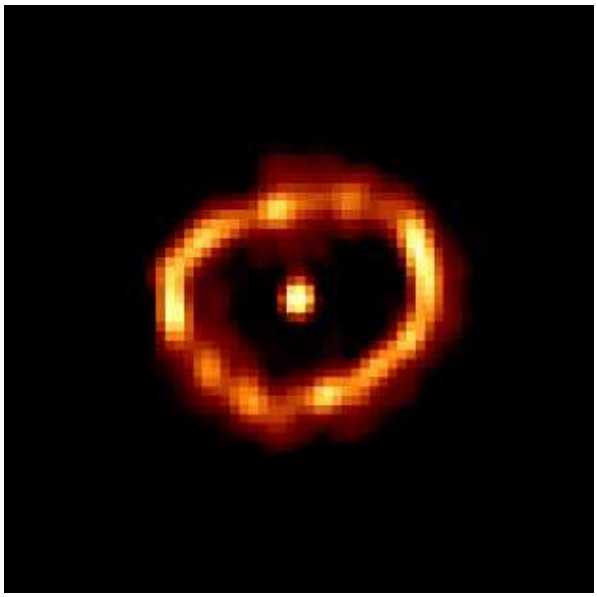

Figure 1.6: Nova Cygni 1992, as observed with Hubble Space telescope two years after the explosion [Cyg92]. The center dot is the remaining binary star system and the ring is the ejected surface.

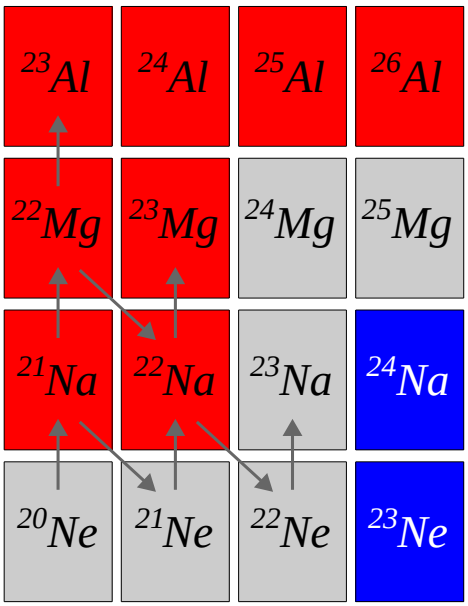

Figure 1.7: Partial reaction network from ^{20}Ne to ^{26}Al. Color code: red β^+ decay, blue β^- decay, grey stable nuclei. The arrows $\uparrow$ stand for the (p,γ) reaction rate, $\searrow$ stand for the β^+ decay rate.

[Cyg92]. In general, the characteristic light curves (the star's luminosity as a function of the time) show a rapid luminosity increase by 9 or 10 orders of magnitude. Within 10-250 days, the luminosity is back to a level comparable to the status before the nova event [Jos07].

Due to the high temperatures ($T_6 \lesssim 300$ for O/Ne novae) when the degeneracy is overcome and the new hydrogen fuel on the surface of the C/O or O/Ne core resonant (p,γ) proton capture reactions on dredged up seed nuclei such as ^{20}Ne occur. Sequences of proton captures and/or β decays allow nucleosynthesis up to $A \approx 40$. Classical novae are not the dominant sites of nucleosynthesis in our Galaxy, however they can contribute to the abundance of particular isotopes [Her05], whose abundances can not be explained from burning sequences (see section 1.1). The mean ejected mass into the inter stellar medium "probably exceeds $2 \cdot 10^{-4} M_\odot$" per event [Sta01].

γ-ray signatures from short lived nuclei, which are produced by (p,γ) reactions, such as ^{13}N and ^{18}F can be observed in principle, for all classical novae. Several long-lived isotopes are produced whose β-decay gives rise to characteristic γ-ray lines such as ^{22}Na and ^{26}Al. These can only be produced in O/Ne novae, while e.g. ^{7}Be is only produced in C/O novae. The characteristic γ-rays allow a distinction of both types and their observed intensities can be used to gather information about the environment such as the temperature. This is possible, if their production reaction rates are known, which

in turn depend on the temperature.

Reaction rate network calculations have been developed to estimate the isotopic abundances in the ejected matter. Many physical properties of the environment (temperature, pressure, density) and the pre-existing seed nuclei (density distribution, reaction rates at different temperatures) are needed for these calculations.

The question for the net production of e.g. ^{22}Na whose (γ-ray intensity could be observed with telescopes) can only be answered, if one looks to all processes that affect the abundance of this nucleus. For demonstration, only the physical processes (p, γ) and β decay are allowed in the following.

As shown in Figure 1.7, ^{22}Na is produced by proton capture (p, γ) of ^{21}Ne or by β decay of ^{22}Mg. The destruction occurs by proton capture of ^{22}Na to ^{23}Mg or its β decay to ^{22}Ne. If all rates of productive and destructive reactions are known, the net production of ^{22}Na can be estimated, if the amount of ^{22}Mg and ^{21}Ne is known, whose abundances in turn are determined by their production and destruction reaction rates. A reaction rate network therefore will assume an initial seed composition of nuclei and apply reaction rates that are determined from theory and experimental measurements.

With a large reaction network and the consideration of dynamic pressures and temperatures, a diverse seed composition and densities as well as more physical interactions, these network calculations become very complex. Typical reaction networks for classical nova studies use $\sim$ 150 stable and proton rich isotopes with A $\leqslant$ 40 which are linked with few thousand nuclear processes such as (p, γ), (p, α), (α, γ) and their reverse reactions [Ili02]. The reaction rates can be taken from published compilations (such as [Ang99] or [Ili10]).

Sensitivity studies of the abundances of nuclei in the ejecta by variations of reaction rates [Ili02] show which reaction rates have a crucial effect on the final isotopic abundance in the simulated network. The crucial reaction rates can then be subject of experimental measurements.

Classical novae are relatively simple objects compared to other events such as super novae (see section 1.2), which allows to challenge and to improve theoretical models.

1.5 Thermonuclear Reaction Rates

The following section describes the mathematical background of thermonuclear reaction rates. Non-resonant and resonant thermonuclear reaction rates are discussed in sub chapter 1.5.1 and 1.5.2, respectively. The detailed derivations can be found in [Ili06, Sar82, Cla83].

The total cross section σ of a nuclear reaction is given by:

$$\sigma = \frac{\mathrm{Y}_{\mathrm{reactions}}}{\rho_{\mathrm{target}} \Delta x \ \mathrm{N}_{\mathrm{beam}}} \tag{1.1}$$

with the number of occurring reactions per time $\mathrm{Y}_{\mathrm{reactions}}$, the particle density of the target ρ_{target}, its thickness Δx and the number of beam particles per time hitting the target $\mathrm{N}_{\mathrm{beam}}$. This equation is the foundation of all direct cross section measurements.

The dependence of $\sigma(E,\theta)$ on the energy E and the polar scattering angle θ can be observed and this gives insight to the nuclear structures of the involved particles. The total cross section is given by the integral:

$$\sigma = \int \left(\frac{d^2\sigma(\theta, E)}{d\Omega dE} \right) d\Omega dE \tag{1.2}$$

where $d\Omega$ is the covered solid angle.

Assuming a known cross section σ, the reaction rate volume density r_{01} in units of $\left[(\text{volume} \times \text{time})^{-1}\right]$ can be calculated:

$$r_{01} = \frac{\mathrm{N}_0\mathrm{N}_1}{\delta_{01}+1} v\sigma(v) \tag{1.3}$$

N_i is the number density of the interacting particle species $i = 0, 1$ in units of $\left[(\text{volume})^{-1}\right]$, v is the relative velocity of the two reacting particles to each other.

The velocity distribution of particles in a volume with the temperature T follows the Maxwell-Boltzmann distribution $P(v)$:

$$P(v)dv = \left(\frac{m_{01}}{2\pi kT}\right)^{3/2} e^{-m_{01}v^2/(2kT)} 4\pi v^2 dv \tag{1.4}$$

with the reduced mass $m_{01} = (M_0 M_1)/(M_0 + M_1)$ of the reacting particle species $i = 0, 1$ with the masses M_i, the Boltzmann constant k and the temperature T.

Introducing the non relativistic velocity-energy relation: $E = m_{01}v^2/2$ and therefore $dE/dv = m_{01}v$, it can be deduced:

$$\begin{aligned} P(v)dv &= P(E)dE \\ &= \left(\frac{m_{01}}{2\pi kT}\right)^{3/2} e^{-E/(kT)} 4\pi \frac{2E}{m_{01}} \frac{dE}{m_{01}} \sqrt{\frac{m_{01}}{2E}} \\ &= \frac{2}{\sqrt{\pi}} \frac{1}{(kT)^{3/2}} \sqrt{E} e^{-E/kT} dE \end{aligned} \tag{1.5}$$

Equation 1.5 can be combined with Eq. 1.3, resulting in the thermonuclear normalized reaction rate for the particle species 0 and 1:

$$\begin{aligned} \langle \sigma v \rangle_{01} &= \int_0^\infty v P(v) \sigma(v) dv \\ &= \int_0^\infty v P(E) \sigma(E) dE \\ &= \left(\frac{8}{\pi m_{01}}\right)^{1/2} \frac{1}{(kT)^{3/2}} \int_0^\infty E\sigma(E) e^{-E/kT} dE \end{aligned} \tag{1.6}$$

with $v = \sqrt{\frac{2E}{m_{01}}}$

1.5.1 The Non-Resonant Thermonuclear Reaction Rates

In the following, the so called S-factor is introduced that is motivated by the energy dependence in the derivation of the cross section from quantum mechanics [Ili06], given by:

$$\sigma \propto G(E) \cdot M(E) \cdot T_l(E) \tag{1.7}$$

with the geometric factor $G(E)$, the matrix element $M(E)$ that describes nuclear structure effects and the transmission probability $T_l(E)$ of the particle to penetrate the Coulomb barrier with the anglular momentum l, given by (assuming $l = 0$):

$$\begin{aligned} G(E) &\propto \lambda^2 & T(E) &= \exp\left(-2\pi\ Z_0 Z_1 \frac{e^2}{\hbar}\sqrt{\frac{m_{01}}{E}}\right) \\ &\propto \frac{h^2}{p^2} & &\equiv e^{-2\pi\eta} \\ &= \left(\frac{h}{\sqrt{2m_{01}E}}\right)^2 & \text{with}\quad \eta &= Z_0 Z_1 \frac{e^2}{\hbar}\sqrt{\frac{m_{01}}{E}} \end{aligned} \tag{1.8}$$

with the de Broglie wave length λ, where h is the Planck constant, p is the momentum and m_{01} the reduced mass of the particle species 0 and 1 as previously defined. $T(E)$ is the s-wave transmission probability for a Coulomb barrier [Mus88, Ili06], with the new introduced factor $e^{-2\pi\eta}$, which is called Gamow factor. These two functions ($G(E)$ and $T(E)$) introduce a general, strong energy dependence that is not caused by nuclear structure effects. All higher order effects (angular momentum, resonances) are described by the matrix element $M(E)$. In principle the astrophysical S-factor now includes all higher order effects on the cross section σ that are not described by $G(E)$ and $T(E)$. It is defined by

$$S(E) = \frac{E\sigma(E)}{e^{-2\pi\eta}} \tag{1.9}$$

and removes the first order energy dependence described previously [Cla83].

The reaction rate in Eq. 1.6 then can be written as:

$$\begin{aligned} \langle\sigma v\rangle_{01} &= \left(\frac{8}{\pi m_{01}}\right)^{1/2} \frac{1}{(kT)^{3/2}} \int_0^\infty e^{-2\pi\eta} S(E) e^{-E/kT} dE \\ &= \left(\frac{8}{\pi m_{01}}\right)^{1/2} \frac{1}{(kT)^{3/2}} \int_0^\infty S(E) e^{-2\pi\eta - E/kT} \end{aligned} \tag{1.10}$$

The S-factor in Eq. 1.10 contributes mostly to the energy integral in the energy range where $e^{-2\pi\eta - E/kT}$ becomes large. This product of the Gamow factor and the Maxwell-Boltzmann function is called Gamow peak and the components and the product is plotted in Figure 1.8(a) for the reaction $^{30}\mathrm{P}(\mathrm{p},\gamma)^{31}\mathrm{S}$ at a temperature $\mathrm{T}_9 = 0.2$. The linear plot of the Gamow peak is shown in Figure 1.8(b). Because this Gamow peak is convolved with the $S(E)$ function in Equation 1.10, contributions within this peak will dominate the energy integral.

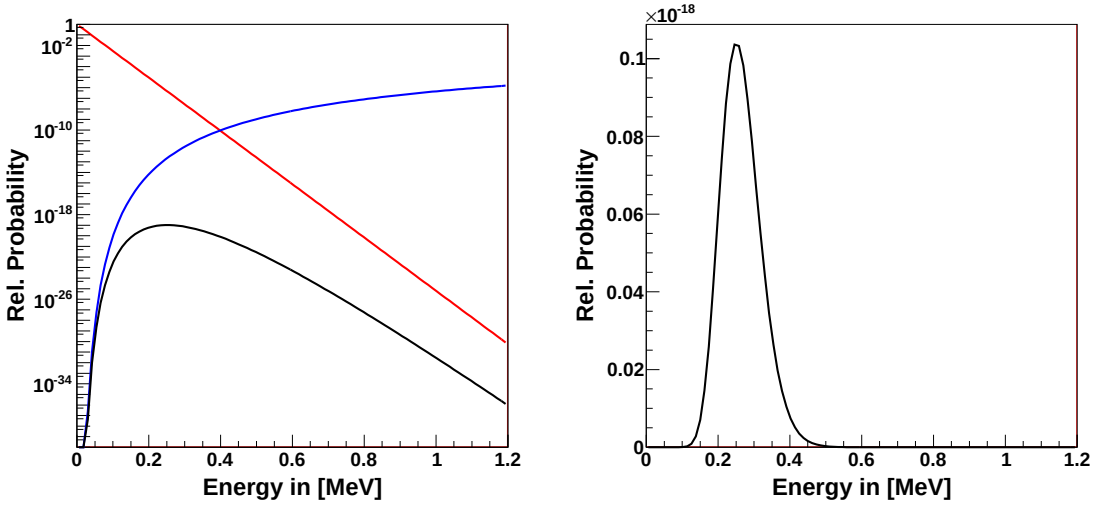

(a) (b)

Figure 1.8: The Gamow factor $e^{-2\pi\eta}$ (blue line) and the Maxwell-Boltzmann factor $e^{-E/kT}$ (red line) are plotted in (a) separately in a logarithmic scale. The functions show the factors for the reaction $^{30}\mathrm{P}(\mathrm{p},\gamma)^{31}\mathrm{S}$ at $\mathrm{T}_9 = 0.2$. Their product (black) is called Gamow peak and is plotted in a linear scale in (b).

The derivative of the Gamow peak, when set equal to zero, allows one to determine the energy with the maximum probability E_{eff} [Cla83]

$$E_{\mathrm{eff}} = \left(\left(\frac{\pi}{\hbar} \right)^2 (Z_0 Z_1 e^2)^2 \frac{m_{01}}{2} (kT)^2 \right)^{1/3} \tag{1.11}$$

The Gamow peak can be approximated with a Gaussian with its maximum at the same energy E_{eff} and the same first and second derivatives. The solution of the integral from $-\infty$ to ∞ of the Gaussian is $\sqrt{\pi}\Delta/2$. The Gamow peak therefore can be written:

$$\begin{aligned} e^{-2\pi\eta} e^{-E/kT} &= e^{-2\pi\eta - E/kT} \\ &= e^{-\frac{2E_{\mathrm{eff}}^{3/2}}{\sqrt{E}kT} - \frac{E}{kT}} \\ &\approx e^{-\frac{3E_{\mathrm{eff}}}{kT}} \; e^{-(\frac{E-E_{\mathrm{eff}}}{\Delta/2})^2} \\ \text{with its width:} \Delta &= \frac{4}{\sqrt{3}} \sqrt{E_{\mathrm{eff}} kT} \end{aligned} \tag{1.12}$$

Using the Gaussian approximation from Equation 1.12, expand the integral range to $[-\infty, \infty]$ and assuming a constant S-factor $S(E) = S_0$ one can derive the non-resonant

reaction rate to be [Ili06]:

$$\begin{aligned}\langle\sigma v\rangle_{01} &= \left(\frac{8}{\pi m_{01}}\right)^{1/2}\frac{1}{(kT)^{3/2}}S_0\int_0^\infty e^{-2\pi\eta}e^{-E/kT}dE \\ &\approx \left(\frac{8}{\pi m_{01}}\right)^{1/2}\frac{1}{(kT)^{3/2}}S_0 e^{-3E_{\text{eff}}/kT}\int_{-\infty}^\infty e^{-(\frac{E-E_{\text{eff}}}{\Delta/2})^2}dE \\ &= \sqrt{\frac{2(M_0+M_1)}{M_0M_1}}\frac{\Delta}{(kT)^{3/2}}S_0 e^{-3E_{\text{eff}}/kT}\end{aligned} \tag{1.13}$$

The expansion of the integral range is reasonable, because the contribution from $[-\infty, 0]$ can be neglected, but allows to solve the integral. If the the S-factor can not be assumed to be a constant, the integral can be solved numerically.

1.5.2 The Resonant Thermonuclear Reaction Rates

The cross section of a single narrow (compared to the level density) resonance can be described using the Breit-Wigner formula [Ili06]. The assumption of two different reacting particles is made:

$$\sigma_{B.-W.}(E) = \frac{\pi\hbar^2}{2m_{01}E}\frac{(2J+1)}{(2j_0+1)(2j_1+1)}\frac{\Gamma_a\Gamma_b}{(E_{\text{res}}-E)^2+\Gamma^2/4} \tag{1.14}$$

with the reduced mass of the particles 0 and 1 $m_{01} = \frac{M_0M_1}{M_0+M_1}$, the collision energy E in the c.m.s., the energy E_{res} and the spin J of the resonance level in the product, the spins j_0 and j_1 of the incoming reacting particles, the partial widths of the entrance and the exit channel Γ_a Γ_b (chance of the reverse reaction, going back to incoming particles vs. staying with the produced nucleus) and the total resonance width $\Gamma = \Gamma_a + \Gamma_b$.

Introducing $\sigma_{B.-W.}(E)$ in Equation 1.6, the reaction rate contribution from this single, narrow resonance can be calculated:

$$\begin{aligned}\langle\sigma v\rangle_{single} &= \left(\frac{8}{\pi m_{01}}\right)^{1/2}\frac{1}{(kT)^{3/2}}\int_0^\infty E\sigma_{B.-W.}(E)e^{-E/kT}dE \\ &= \frac{\sqrt{2\pi}\hbar^2}{(m_{01}kT)^{3/2}}\omega\int_0^\infty\frac{\Gamma_a\Gamma_b}{(E_{\text{res}}-E)^2+\Gamma^2/4}e^{-E/kT}dE \\ \text{with: } \omega &= \frac{(2J+1)}{(2j_0+1)(2j_1+1)} \\ \text{assumption: } & e^{-E/kT} = e^{-E_{\text{res}}/kT} \text{ and: } \Gamma_i(E) = \Gamma_i \text{ within the narrow resonance} \\ \text{expand with: } & \Gamma/2 \\ &= \frac{\sqrt{2\pi}\hbar^2}{(m_{01}kT)^{3/2}}\omega\Gamma_a\Gamma_b e^{-E_{\text{res}}/kT}\frac{2}{\Gamma}\underbrace{\int_0^\infty\frac{\Gamma/2}{(E_{\text{res}}-E)^2+\Gamma^2/4}dE}_{=\pi(\text{Lorentz function integral})} \\ &= (\frac{2\pi}{m_{01}kT})^{3/2}\hbar\omega\frac{\Gamma_a\Gamma_b}{\Gamma}e^{-E_{\text{res}}/kT}\end{aligned} \tag{1.15}$$

with $\gamma \equiv \frac{\Gamma_a \Gamma_b}{\Gamma}$ we get:

$$\langle \sigma v \rangle_{single} = (\frac{2\pi}{m_{01}kT})^{3/2} \hbar \omega \gamma e^{-E_{\rm res}/kT} \tag{1.16}$$

If a reaction has several resonances within the energy range of interest (here: Gamow peak), one has to sum all single rates of the resonances to determine the total rate of the reaction. Therefore:

$$\langle \sigma v \rangle = (\frac{2\pi}{m_{01}kT})^{3/2} \hbar \sum_i \omega_i \gamma_i e^{-E_{{\rm res}i}/kT} \tag{1.17}$$

with the resonance strength $\omega_i \gamma_i$:

$$\omega_i \gamma_i = \frac{(2J_i + 1)}{(2j_0 + 1)(2j_1 + 1)} \frac{\Gamma_{a,i} \Gamma_{b,i}}{\Gamma_i} \tag{1.18}$$

For a resonant (p, γ) reaction rate, $a =$ proton and $b = \gamma$-ray.

While extrapolations of the S-factor for the non resonant components of thermonuclear reactions are necessary for energy ranges below experimental access, reaction rates for the resonant components of thermonuclear reactions can be determined indirectly by measuring properties of the incident particles and the produced nucleus.

This can be done for example for (p, γ) reactions that are important in astrophysical scenarios such as classical nova events at low temperatures ($T_6 = 20 - 350$) where no direct measurements of reaction rates are feasible so far. The indirect method is using Equation 1.17 and 1.18 to determine the reaction rate by maesuring the quantities in those equations individually. Since ground state spins of nuclei are widely known, only the properties of the compound nucleus need to be measured; namely the spins J_i, $\mathrm{E}_i^{\rm ex} = \mathrm{Q}_{\rm value} + \mathrm{E}_i^{\rm res}$ (with the Q-value $\mathrm{Q}_{\rm value}$ of the reaction) and the partial widths $\Gamma_{\gamma,i}$ of each resonant state i. Since only resonances within the energy range of the Gamow peak dominate the reaction rate, only these states of interest need to be measured in order to determine the effective reaction rate. The total width $\Gamma_i = \frac{\hbar}{\tau_i}$ can be determined by the lifetime τ measurement of the excited state with experimental methods that will be described in the next sections.

1.6 The Experimental Techniques for Lifetime Measurements of Excited States

Since the lifetimes of excited nuclear states can vary by orders of magnitudes, adapted experimental techniques are necessary to determine lifetimes of different time ranges. Figure 1.9 shows the lifetime ranges that can be determined with the techniques "Fast electronic timing", "Recoil Distance Doppler Shift" Method (RSSD) and the "Doppler Shift Attenuation Method" (DSAM). The methods are explained in the following sections.

The lifetime of a state with $\tau \gtrsim 100$ ps can be determined with fast electronic timing experiments that measure the time difference between the population of the

Figure 1.9: The different time ranges of methods for lifetime measurements of excited states in nuclei. The arrow indicates the time bar that is started with the population of the state of interest. RSSD stands for "Recoil Distance Doppler Shift" Method and DSAM stands for "Doppler Shift Attenuation Method".

state of interest and the moment of its de-excitation via γ-ray emission. Therefore, such experiments need a start and a stop signal. For example, if the production of the excited nucleus can be detected, this signal can be used as a start for a timing measurement. The detection of the delayed emitted γ-ray can be used as the stop signal. Many of these timing measurements can be histogrammed and will result in a distribution, following the exponential decay law. The lifetime τ can then be extracted by fitting the formula

$$\mathrm{A(t)} = \mathrm{A_0} \exp(-t/\tau) \tag{1.19}$$

with the time after the population of the state of interest t, the number of observed γ-ray de-excitations after a given time $\mathrm{A}(t)$ and the total number of measurements $\mathrm{A_0}$.

The Recoil Distance Doppler Shift Method (RSSD) allows the measurement of the lifetime of excited states in nuclei in the range between $\sim$ 1 ps and $\sim$ 100 ps. In experiments applying this technique, an ion beam is focused on a thin target where the excitation of the nucleus of interest takes place. Due to conservation of momentum, the excited nucleus penetrates the thin target and moves a distance d through vacuum with a constant velocity $\vec{\beta}$, before it is stopped in a second, thick stopper target. The γ-ray de-excitation can be observed with a high purity germanium (HPGe) detector positioned in the forward direction of the trajectory of the excited nucleus. If the γ-ray emission occurs in flight, the observed γ-ray energy will show a positive shift due to the Doppler effect. If the γ-ray emission occurs after the excited nucleus is stopped in the stopper target, no Doppler shift will be observed. The time of flight between the thin target and the stopper target is given by $t_{\mathrm{flight}} = d \cos\delta \cdot |\vec{\beta}|^{-1}$ with δ the angle between $\vec{\beta}$ and the normal of the target surfaces. The observed $\mathrm{E}_\gamma^{\mathrm{obs}}$ spectrum will

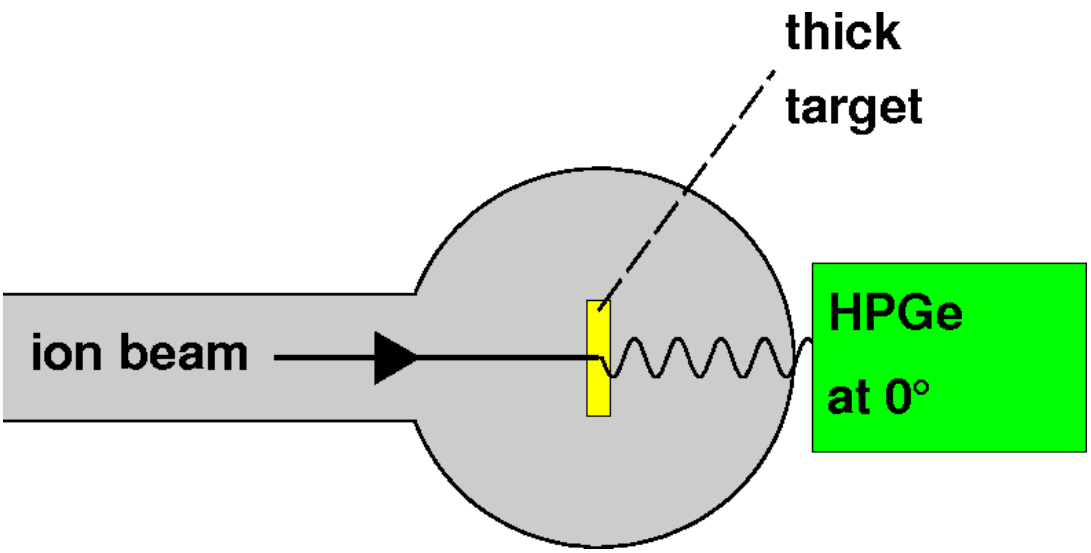

Figure 1.10: The schematic setup of a DSAM experiment. The evacuated beam line and target chamber are indicated in grey. The beam comes from the left and is stopped in a thick target (yellow). A HPGe detector (green) at 0° with respect to the beam axis is used to observe γ-rays (wave line) that are emitted in forward direction and to determine their energies.

show a peak with N_0 γ-ray events with the transition energy E_γ^0 as observed in the rest frame and a second energy peak with N_{shifted} γ-ray events with the Doppler shifted energy $E_\gamma^{\text{obs}} = E_\gamma^0(1 + |\vec{\beta}| \cos\alpha)$ with α the angle between the velocity vector $\vec{\beta}$ of the de-exciting nucleus and the direction of the γ-ray emission. Because the de-excitation probability distribution follows a time dependence given by Equation 1.19, the lifetime can be extracted from the ratios of the integrals of both peaks:

$$\frac{N_{\text{shifted}}}{N_{\text{shifted}} + N_0} = \int_{t=0}^{t_{\text{flight}}} \exp(-t/\tau) \tag{1.20}$$

And now coming to the Doppler shift attenuation Method (DSAM), it allows the measurement of excited state lifetimes in the range between ~ 10 fs and ~ 1 ps. This method is subject of this thesis and is described in detail in the next sub chapter 1.7.

1.7 The Doppler Shift Attenuation Method (DSAM)

First experiments exploiting the Doppler shift in an observed γ-ray transition to extract information about the lifetime of the de-exciting state were performed in the 1950's [Dev55, Ras49]. In the following decades the analysis technique and the γ-ray detectors have been significantly improved, however the basic idea has not changed. Typically, lifetimes between a few fs and a few ps can be determined with this method. The following section describes the basic physical principles and shows how the lifetime of the excited state affects the observed γ-ray energy spectrum.

Figure 1.10 shows a simplified schematic setup of a DSAM experiment. An ion beam is focused on a target (yellow) that is sufficiently thick to stop the beam and all beam like reaction products. A nuclear reaction directly below the surface of the target produces the excited nucleus of interest. Because momentum is conserved and due to inverse kinematics, the excited nucleus has a motion in forward direction and is eventually stopped in the thick target. If the lifetime of the populated state is of the same order as the time scale of the stopping process, the de-excitation via γ-ray emission may occur in-motion and while undergoing deceleration. Due to the velocity of the de-exciting nucleus relative to the γ-ray detector in the lab frame, the observed energy $\mathrm{E}_\gamma^{\mathrm{obs}}$ will then be Doppler shifted according to the formula [Kri85]:

$$\mathrm{E}_\gamma^{\mathrm{obs}} = \mathrm{E}_\gamma^0 \frac{\sqrt{1-\beta(\mathrm{t})^2}}{1-\beta(\mathrm{t})\cos\alpha} \overset{v\ll \mathrm{c}}{\approx} \mathrm{E}_\gamma^0 \left(1+\beta(\mathrm{t})\cos\alpha\right) \tag{1.21}$$

with the rest-frame transition energy E_γ^0, $\beta(\mathrm{t}) = |v(\vec{\mathrm{t}})|/\mathrm{c}$ the speed of the nucleus at the moment of its de-excitation in units of the speed of light c, and α the angle between the velocity vector $\vec{\beta}(\mathrm{t})$ and the direction of the γ-ray emission. For non-relativistic velocities ($v \ll \mathrm{c}$), the first order Taylor series has been applied. This energy shift can be measured in the lab frame with a HPGe γ-ray detector, which is indicated in green in Figure 1.10 at an angle of 0° with respect to the beam axis.

The observed Doppler shift in the γ-ray energy is positive for observation angles $0° < \alpha < 90°$ and negative for observation angles $90° < \alpha < 180°$ (see $\cos(\alpha)$ term in Eq. 1.21). Additionally, the observed energy shift is determined by the velocity of the de-exciting nucleus relative to the detector.

A measured $\mathrm{E}_\gamma^{\mathrm{obs}}$ spectrum will show γ-ray events from nuclei that were already stopped at the transition energy E_γ^0. If the de-excitation takes place while the nucleus is still in motion with the velocity $\vec{\beta}$, a Doppler shifted energy will be measured following Eq. 1.21.

The velocity $\vec{\beta}(t)$ of the excited nucleus in the target can be defined as a function of the time after the population. It can be simulated as it will be shown in section 4.3.1.

The probability, in time, of an excited state undergoing decay follows an exponential decay law, analogous to that of radioactive decay. The activity $\mathrm{A}(t)$ of a total number of A_0 excited nuclei as a function of the time t after the population of the state is therefore given by Eq. 1.19. If a total number of A_0 events are observed in an experiment, the activity function $\mathrm{A}(t)$ will be convolved with the velocity function $\vec{\beta}(t)$, resulting in the activity as a function of the velocity $A(\vec{\beta})$. An acquired $\mathrm{E}_\gamma^{\mathrm{obs}}$ spectrum of observed γ-rays will therefore show a distinct line shape that is characterized by the lifetime of the observed state and the deceleration of the excited nucleus in the target.

For demonstration, Figure 1.11 shows the simulated $\mathrm{E}_\gamma^{\mathrm{obs}}$ spectra of the HPGe detector at 0° with respect to the beam axis. A transition energy of $\mathrm{E}_\gamma^0 = 1$ MeV was arbitrarily chosen, but two different lifetimes of $\tau = 1.0$ ps and $\tau = 0.1$ ps were assumed in (a) and (b), respectively. The stopping process in the target has been simulated (see chapter 4 for details) and has been convolved with the activity function defined by the lifetime τ (see Equation 1.19).

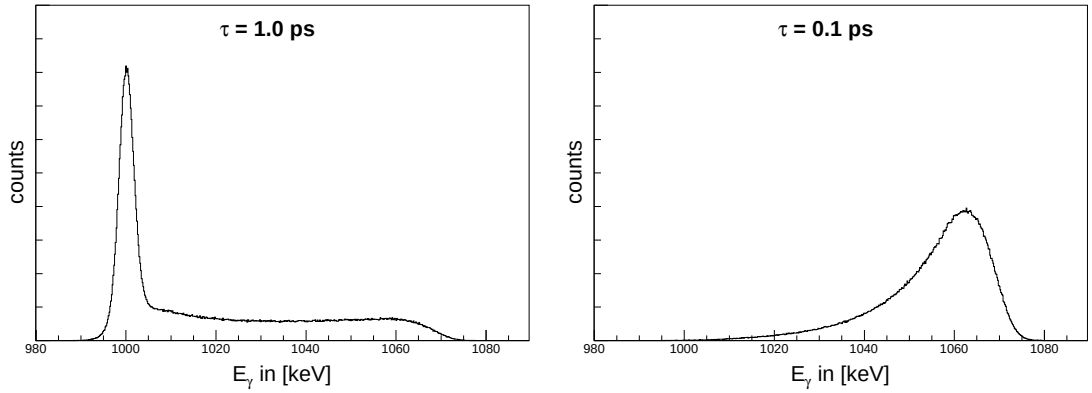

(a) (b)

Figure 1.11: The simulated E_γ^{obs} spectra in a DSAM experiment with an assumed transition energy of $E_\gamma^0 = 1$ MeV and a lifetime of $\tau = 1.0$ ps in (a) and $\tau = 0.1$ ps in (b).

The simulated excited nuclei had a start velocity in the target of roughly $\beta_{t=0} = 0.07c$ and were stopped after 1.5 ps. Events in the peak at $E_\gamma^{obs} = 1$ MeV (Figure 1.11(a)) are caused by γ-ray emissions after the excited nucleus has been stopped. The γ-rays that are observed at higher energies have been emitted in-motion. The maximum energy shift ($E_\gamma^{obs} = E_\gamma^0(1+\beta_{t=0}) = 1.07$ MeV) is given by the maximum velocity of the excited nucleus.

Because the chosen lifetime of 1.0 ps in Figure 1.11(a), a considerable number of excited nuclei have been stopped in the target before the γ-ray emission, resulting in a peak at $E_\gamma^{obs} = E_\gamma^0 = 1$ MeV in the energy histogram. A much shorter lifetime of $\tau = 0.1$ ps was chosen in 1.11(b). Therefore, all γ-ray emissions occur in-motion and the E_γ spectrum shows a line shape that is highly affected by the Doppler shift to higher energies.

The line shape in the E_γ^{obs} spectrum can be measured experimentally. If the stopping power is known, the lifetime of the observed state can be extracted. The simulation and the analysis of such an experiment is shown in detail in chapter 4.

In principle any kind of nuclear reaction such as (p, γ) or Coulomb excitation can be used that directly populates the state of interest. If the observed state has been populated indirectly by feeding from higher states, the line shape will be characterized by the lifetimes and the branching ratios of all states that feed into the state of interest as well. The determined lifetime will then be longer than the actual lifetime of the state of interest. In principle a correction would be possible, but introduces additional errors due to the uncertainties in the lifetimes and branching ratios of the feeding states.

Hence transfer reactions where one or several nucleons are transferred between the projectile and the target nucleus are preferable, because the kinematics can be solved in a two body problem. The angle and the energy of the light ejectile then uniquely identify the directly populated state of the excited nucleus. Both observables of the light ejectile can be determined in an experiment which allows one to identify events of

interest by particle-γ coincidences. Events, where the state of interest was not directly populated can be rejected and therefore the determined lifetime is not corrupted.

Beam experiments can in principle be performed in inverse or in direct kinematics. In direct kinematics, the heavier nucleus is used as a target and is bombarded with a lighter projectile. In contrast, when a heavy projectile impinges on a light target, the system is called inverse kinematics. Applying the same center of mass energy, a higher velocity of the center of mass (c.m.) frame in the lab frame can be obtained in inverse kinematics and in case of a DSAM experiment, larger energy shifts of the γ-rays can be observed, thereby providing a higher sensitivity to measuring shorter lifetimes.

Capturing these advantages, the new DSAM setup at the Maier-Leibnitz Laboratory (MLL) has been designed for transfer reactions in inverse kinematics. This allows the measurement of all observables such as angle, energy and identity of the light ejectile of the transfer reaction and to measure the Doppler shifted energy of the coincident γ-ray from the de-excitation of the heavy nucleus.

The target in a Doppler shift experiment, using a transfer reaction in inverse kinematics requires two conditions. First, the light reaction partner must be supplied and second, a sufficient stopping power is necessary to stop the excited nucleus in the same time range as the lifetime of the populated state. Both requirements can be achieved using implanted targets. Metals with high atomic numbers can supply a sufficient stopping power, while the target nuclei can be implanted below the surface of the metal with a defined depth profile. However, one design requirement of such an approach is that the target must be cooled in order to avoid diffusion of the implanted target nuclei due to beam heating in the target [Myt08].

This document is structured as follows. Chapter 2 describes and motivates the commissioning reaction ^{32}S(^{3}He,^{4} He)^{31}S that was used to determine the lifetime of the first excited state in ^{31}S. It illustrates the requirements to the experimental setup, whose concept and design is then described in detail in chapter 3. The data analysis of the ^{31}S* experiment and the extraction of the lifetime of the first excited state from the line shapes in the E_γ spectra is shown in chapter 4. The result is presented and discussed in chapter 5 and a conclusion with an outlook is given in the last chapter 6.

Chapter 2

The Commissioning Experiment: ^{32}S(^{3}He,^{4} He)^{31}S

As a proof of principle of the new experimental setup and the data analysis methods, the lifetime of the first excited state in ^{31}S (E_{ex} = 1249 keV) has been determined, using the (^{3}He,^{4} He) transfer reaction in a DSAM measurement. While this state itself is of no astrophysical importance, it has a known lifetime, thereby providing an ideal means for commissioning the setup and the analysis methods. In addition, the reaction has been chosen for the following reasons:

- The lifetime of the 1249 keV state in ^{31}S has been measured by Engmann et al. to be (720 ± 180) fs [Eng71]. This information allows one to choose an adequate stopping material and to compare the result.
- The differential cross section of the transfer reaction, populating the first excited state has been measured by McQueen et al. [McQ70]. This allows the optimization of the detection yield of the ^{4}He ejectiles in the silicon detectors and to choose an adequate ion beam energy.
- Engmann et al. [Eng71] have shown that no population of the third or higher states can be observed with a c.m. energy of $E_{cm} = 6.4$ MeV and therefore those yields must be low, even though the commissioning experiment will use a slightly higher c.m. energy of $E_{cm} = 7.3$ MeV. In addition, McQueen [McQ70] does not report any population of higher states at the same c.m. energy as it was used in the commissioning experiment. This is important to assure a direct population of the first excited state. Populating the state indirectly, by way of feeding from higher lying states, would affect the determined lifetime of the state of interest.
- The feeding from the 2nd and the 3rd level into the first excited state are highly suppressed [nud11], thereby avoiding a corruption of the determined lifetime (see the level scheme and the transition probabilities in Figure 2.1).
- The two body kinematics of the transfer reaction allows one to determine the directly populated state in ^{31}S by the observation of the angle and the energy of the ^{4}He ejectile in a charged particle detector. In principle, a cut on the ^{4}He

energy in the experimental data allows one to choose the directly populated state of interest. The first (1249 keV) and the second (2236 keV) excited states in ^{31}S are separated by almost 1 MeV (see Figure 2.1). If the resulting difference in the kinetic energy of the ^{4}He ejectile can be resolved in the experimental setup, a discrimination is possible. Therefore, a large energy gap in the level scheme is preferable in a commissioning experiment.

- The identification of the ^{4}He ejectile allows the reduction of the background in the E_γ spectra from other reactions in the target (e.g. of the beam with impurities on the target).

- The detector response functions and the photo peak efficiencies of the HPGe detectors at the expected transition energy can be well studied, using γ-ray sources such as ^{152}Eu or ^{60}Co. This is mandatory for the lifetime analysis, since the detector response function is convolved with the line shape caused by the Doppler effect.

- The center of mass energy in the consulted former studies by Engmann et al. [Eng71] and McQueen et al. [McQ70] can easily be achieved in inverse kinematics ($E^{lab}_{beam}(^{32}S)$ = 85 MeV), using the tandem accelerator at the MLL. Inverse kinematics increases the observed Doppler shift in the E_γ spectra compared to direct kinematics with the same c.m. energy. Larger energy shifts improve the measurement range of the DSAM technique.

This chapter describes the experimental requirements of the transfer reaction ^{32}S(^{3}He,^{4} He)^{31}S in inverse kinematics and the successful conception of the experimental setup in the commissioning experiment.

2.1 The Requirements of the Experimental Setup

Diverse basic conditions that are coupled to each other, need to be considered for the design of the experimental setup. Especially the interplay of the target thickness and its stopping power, cross sections and competing reactions needed to be balanced to maximize the yield of the reaction of interest in the experiment.

The experimental requirements of the target:

- ^{3}He implanted metal targets are used, where the ^{3}He acts as the reactant in the transfer reaction and the metal is the stopper material, which is needed for the DSA method.

- Applying the same c.m. energy as McQueen et al. of E_{cm} = 7.3 MeV, a ^{32}S beam energy of 85 MeV is necessary in inverse kinematics. The Q-value of the transfer reaction depends on the populated state in ^{31}S by $Q = Q_0 - E_{ex}$ with Q_0 = 5.54 MeV corresponding to the ground state and E_{ex} the energy of the populated state in ^{31}S. Due to the kinematics, the maximum energy of the produced ^{31}S

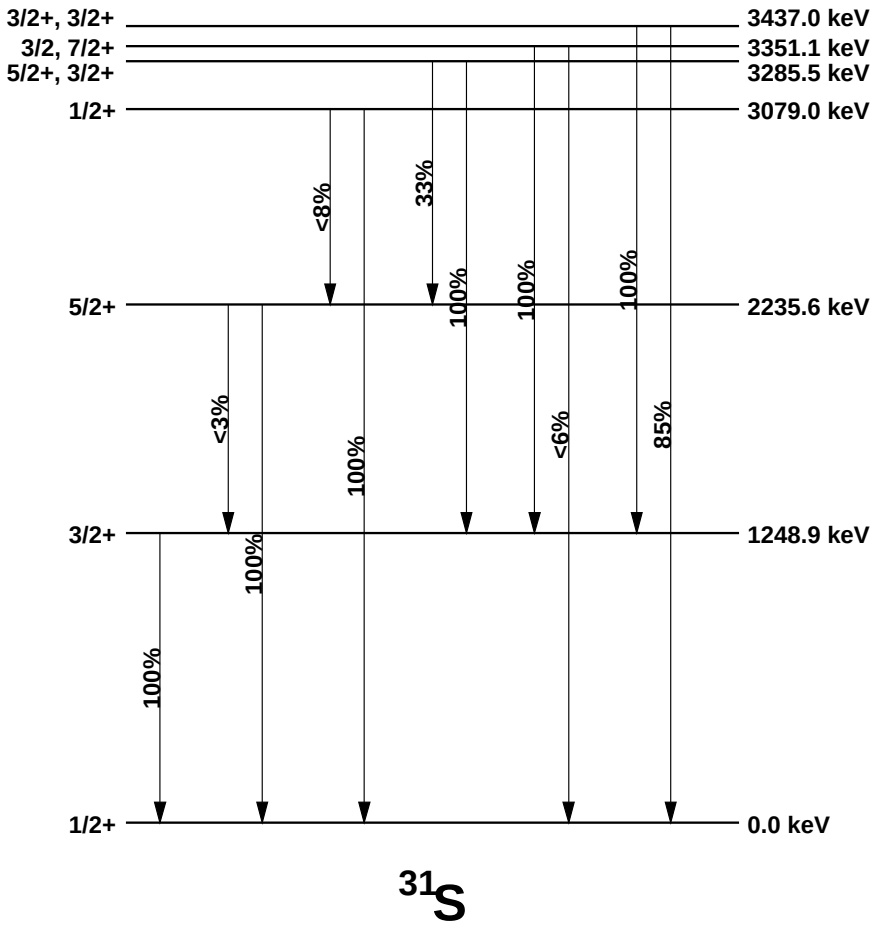

Figure 2.1: The level scheme of ^{31}S and transition probabilities: Feeding from the 2236 keV into the 1249 keV level is highly suppressed ($< 3\%$) and feeding from the 3079 keV into the 1249 keV level has not been observed. Higher states are unlikely to be populated with the used c.m. energy in the transfer reaction ^{32}S(^{3}He,^{4} He)^{31}S. The data is taken from the nudat website [nud11].

nucleus in the first excited state can be as high as 89.3 MeV. Because all excited ^{31}S nuclei must be stopped in a DSAM experiment, the stopping power of the target must be sufficient to decelerate and stop these nuclei within the lifetime of the first excited state.

- In order to observe the ^{4}He ejectiles from the transfer reaction in a particle detector, the target must be as thin as possible, so that the ^{4}He ejectiles can penetrate the target and still have sufficient energy to deposit in the detector. An optimum target thickness can be found, because the ^{4}He nucleus has a much lower atomic number than the ^{31}S nucleus and therefore ^{31}S, having a much higher stopping power, will be stopped while the ^{4}He ejectile can transmit through the target. The observation and identification of the ^{4}He ejectile is necessary to discriminate events of interest via ^{4}He - γ coincidences and thereby reduce the γ-ray background from other reactions.

The experimental requirements of the Si charged-particle detectors:

- An optimum solid angle coverage for a maximum detection yield of the ^{4}He ejectile detection from the transfer reaction is mandatory for the identification of events of interest. Only if a ^{4}He ejectile is detected, a γ-ray de-excitation might be observed in the HPGe detectors. This directly maximizes the particle-γ coincidences in the experiment.

- An optimum solid angle coverage for a minimized elastic ^{3}He event rate is necessary to reduce the dead time of the electronics and to preserve the Si detectors from irradiation damage.

- For the identification of the ^{4}He ejectile, a stack of a thin ΔE and a thick E_{rest} Si detector is used. A good ratio of the energy depositions in the ΔE and E_{rest} detectors is important and can be achieved by the thickness optimization of the ΔE detector.

The achievement of the described requirements will be discussed in the following sections, while the conclusion is given in sub chapter 2.5.

2.2 The Target

Several ^{3}He implanted gold targets with thicknesses between 6.2 μm and 6.3 μm were produced. The gold was chosen because of its high stopping power while the implanted ^{3}He nuclei serve as reactants in the transfer reaction. Simulations with SRIM [Zie08] and Geant4 [Ago03] were used to show that the time range of the stopping process of ^{31}S nuclei in gold and the lifetime of the first excited state in ^{31}S are in the same range.

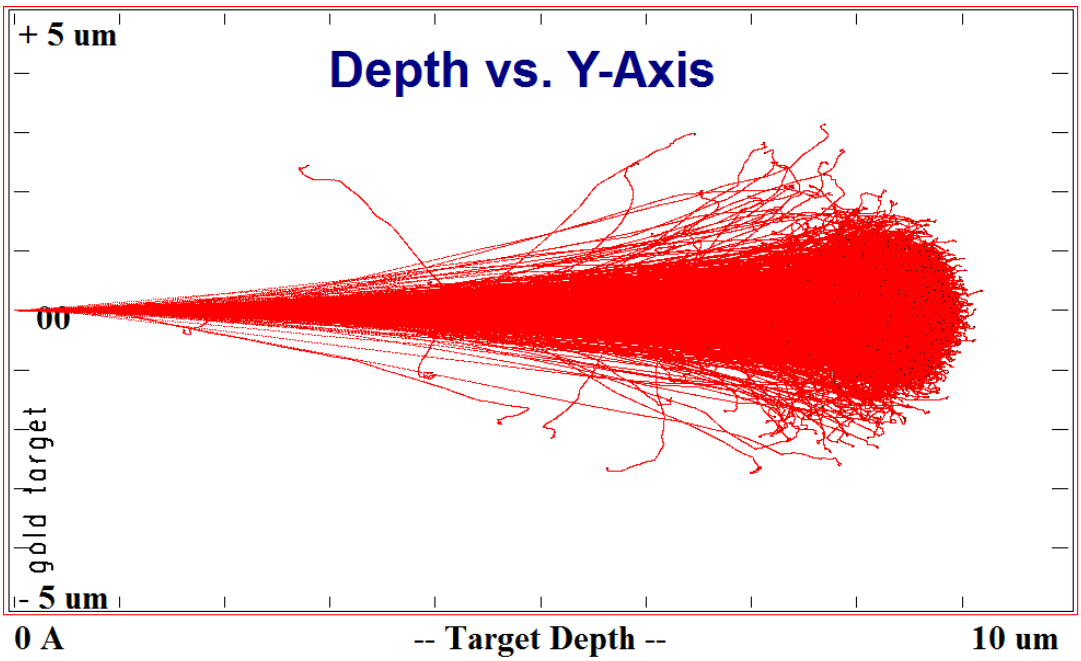

Figure 2.2: SRIM simulation [Zie08] of the trajectories of ^{31}S nuclei in gold with an energy of E = 89.3 MeV from the transfer reaction, populated in the first excited state. The angular straggling is $\sigma = 3.4°$.

2.2.1 The ^{31}S Stopping Power in Gold

For the detection of the ^{4}He ejectiles, the thickness of the target needs to be minimized to maximize their remaining energy after they have exited the target. On the other hand, the corresponding ^{31}S nuclei that are populated in the first excited state must be stopped in a DSAM experiment. Therefore their stopping in gold at their maximum possible energy of $\sim$ 89.3 MeV were simulated with SRIM [Zie08]. The energy for ^{31}S nuclei at polar scattering angles $\theta > 0°$ will decrease as it will be shown in section 2.4. The simulated trajectories in a plane are plotted in Figure 2.2. All ^{31}S nuclei that are excited in the first excited state are stopped within 9.5 μm thickness of the gold target. The angular spread caused by straggling is $\sigma = 3.4°$. This is important, because it affects the direction of the de-exciting nucleus.

The target thickness can be chosen to be even smaller than 9.5 μm, if the target is rotated with respect to the beam axis. The rotation angle can be chosen in a way that the effective thickness in the direction of the ^{31}S nuclei is sufficient to stop them, while the ^{4}He ejectiles in the direction of the particle detectors penetrate a reduced target thickness.

2.2.2 The ^{3}He Implantation into Gold

A 0.15 μm thin layer of implanted ^{3}He nuclei below the surface of the gold foil allows one to define the region where the transfer reaction takes place. The thinness of this implantation layer limits the energy loss of the ^{32}S beam; this, therefore, ensures that the spread in initial velocities of the produced ^{31}S is small, and the uncertainties in the modelling are minimized.

The implantation was done at the Helmholtz Zentrum Dresden Rossendorf (HZDR) [Akh10]. Six gold foils were implanted with a total dose of $6 \cdot 10^{17}$ cm^{-2} each at different energies to create a box like density profile as shown in Figure 2.3. The implantation energies and doses are listed in Table 2.1 and were estimated with SRIM simulations. The density of the implanted ^{3}He particles is limited by the mechanism of blister formation that destroys the surface of the target if the threshold density of $6 \cdot 10^{17}$ cm^{-2} is exceeded [Pás81, Gei84, Ale81].

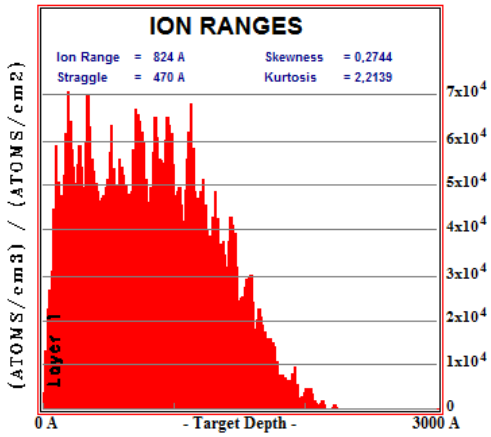

Figure 2.3: The SRIM simulated depth profile of the ^{3}He particles after their implantation in gold with various energies as listed in Table 2.1.

implantation energy	partial dose
5.0 keV	7.58 %
10.0 keV	1.52 %
35.0 keV	90.90 %

Table 2.1: The ^{3}He implantation energies and the partial doses. The total implantation dose was $6 \cdot 10^{17}$ cm^{-2}.

2.3 The Differential Cross Sections

For the optimization of the Si detector positions to detect the ^{4}He ejectiles, theoretical and experimental differential cross sections of the reaction have been considered. The optimum position of the Si detectors is discussed in the following sections.

Experimental cross section measurements of ^{32}S(^{3}He,^{4} He)^{31}S in direct kinematics at a c.m. energy of E_{cm} = 7.3 MeV are available from McQueen et al. [McQ70]. Figure 2.4(a) shows their experimental data and their theoretical predictions for the population of the ground, the first and the second excited state in c.m. coordinates. The data of the state of interest (1.22 MeV) for the commissioning experiment is marked in green. As the authors claim, "the experimental data and the theoretical predictions do not

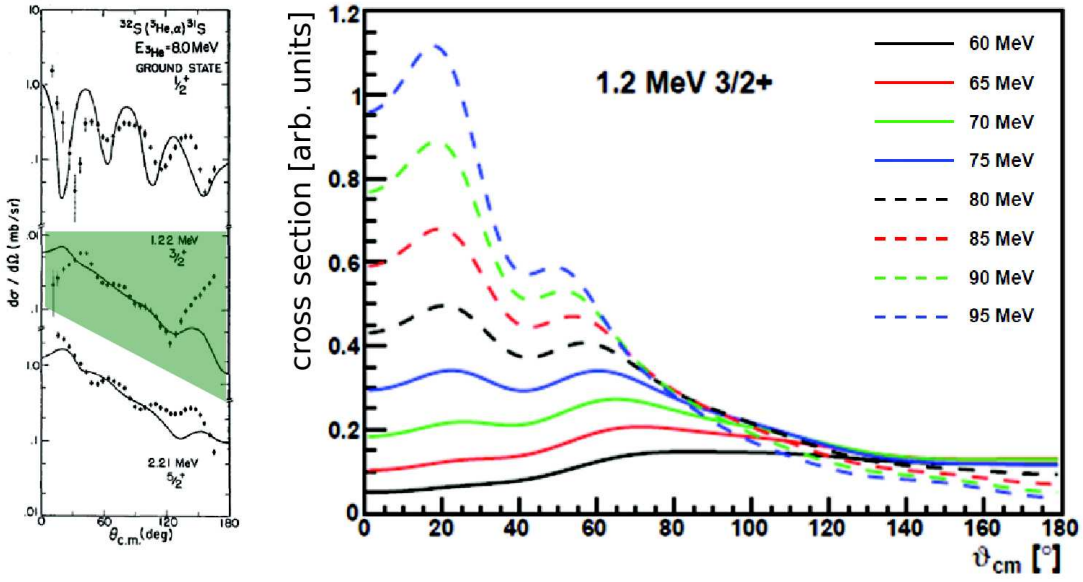

(a) (b)

Figure 2.4: Experimental and theoretical differential cross sections for the ^{4}He ejectile from the reaction ^{32}S(^{3}He,^{4} He)^{31}S* as a function of the polar angle in the c.m. frame. (a) shows experimental data and theoretical predictions for the 1st, 2nd and ground state from McQueen et al. [McQ70] at a c.m. energy of $E_{cm} = 7.3$ MeV. The state of interest is marked in green. (b) shows a qualitative, theoretical prediction for the 1st excited state in ^{31}S from Fresco [Tho88] at different beam energies in inverse kinematics. A 85 MeV ^{32}S beam corresponds to a c.m. energy of $E_{cm} = 7.3$ MeV.

agree very well". Their data shows that the differential cross sections for the c.m. polar angles above 120° rise, which is not predicted by their theoretical calculations. For comparison, the relative differential cross section has been calculated theoretically with the Fresco code [Tho88] and its angular dependence is shown in Figure 2.4(b) for different ^{32}S beam energies [Wim11]. The theoretical predictions from the Fresco code and McQueen qualitatively agree, but do not reproduce the experimental data from McQueen for angles close to 180°. In inverse kinematics, these c.m. angles transform to small polar angles in the lab frame close to 0°. Previous experiments at the DSAM setup have shown that no sufficient yield can be observed if the Si detectors cover these angles in the lab frame. This confirms the theoretical predictions and rejects the experimental data from McQueen et al. for these angles ($\theta_{cm} > 120°$).

The differential cross sections in the c.m.s. need to be transformed to the lab frame to find the best position for the charged particle detectors. While the experimental data from McQueen et al. were used for c.m.s. angles below $\theta_{c.m.} = 120°$, their theoretical prediction was used for angles above 120° for the previously discussed reasons. The result of the transformation to the lab frame is shown in Figure 2.5(a). Considering this

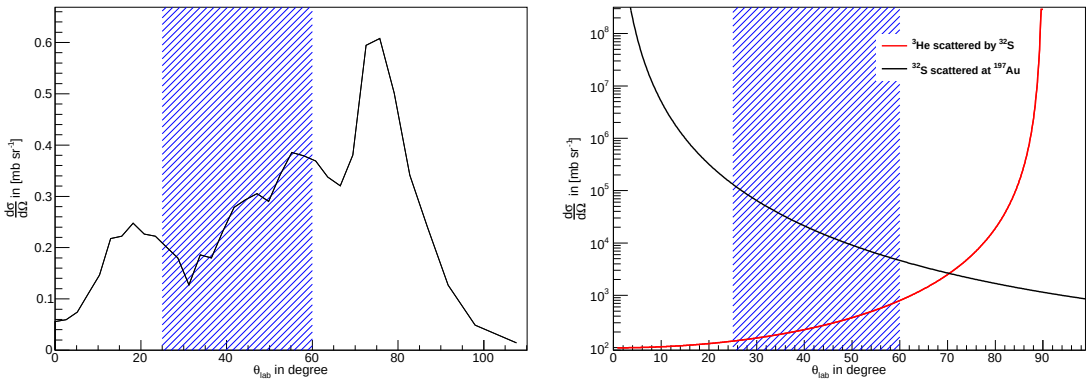

(a) ^{4}He ejectiles from the transfer reaction ^{32}S(^{3}He,^{4} He)^{31}S in a linear scale as a function of the polar angle θ_{lab}.

(b) Elastically scattered ^{3}He and ^{32}S beam particles that are elastically scattered at ^{197}Au in a logarithmic scale as a function of the polar angle θ_{lab}.

Figure 2.5: The laboratory frame differential cross sections of the transfer reaction (a) and Rutherford scattering (b). The blue band in (a) and (b) shows the final covered polar angle range of the Si telescopes as it will be discussed in section 2.5.

plot, the Si detectors would be preferably positioned at angles around 75°, resulting in a maximum yield for the detection of the ^{4}He ejectiles from the transfer reaction.

Figure 2.5(b) shows the laboratory frame differential cross section of elastic Rutherford scattering of ^{32}S with ^{3}He and ^{197}Au. For Rutherford ^{3}He scattering the cross section is maximum at 90°. The detection of the elastically scattered ^{3}He particles allows one to monitor the product of the beam intensity and the amount of ^{3}He particles in the target. Since the beam current can be read from other devices such as Faraday cups, the ^{3}He depletion of the bombarded target can be judged. The target can then be replaced, if the ^{3}He content in the target is exhausted. Nevertheless, the rate of the elastically scattered ^{3}He particles in the Si detectors should be moderate, to avoid radiation damages in the silicon and to reduce the dead time of the electronics. Therefore, the detector position should not be close to 90°. The Rutherford cross section of elastically scattered ^{32}S becomes maximum in the beam direction, where it is stopped in the target. Nevertheless, it must be considered that elastically scattered ^{32}S beam nuclei can penetrate the target at larger polar angles due to the target rotation.

2.4 The Kinematics

The two body kinematics of the transfer reaction determines the energy of the ^{31}S and the ^{4}He ejectile as a function of their polar angles. The kinematics can be derived from the conservation of the kinetic and mass energy and the linear momentum [Kra87]:

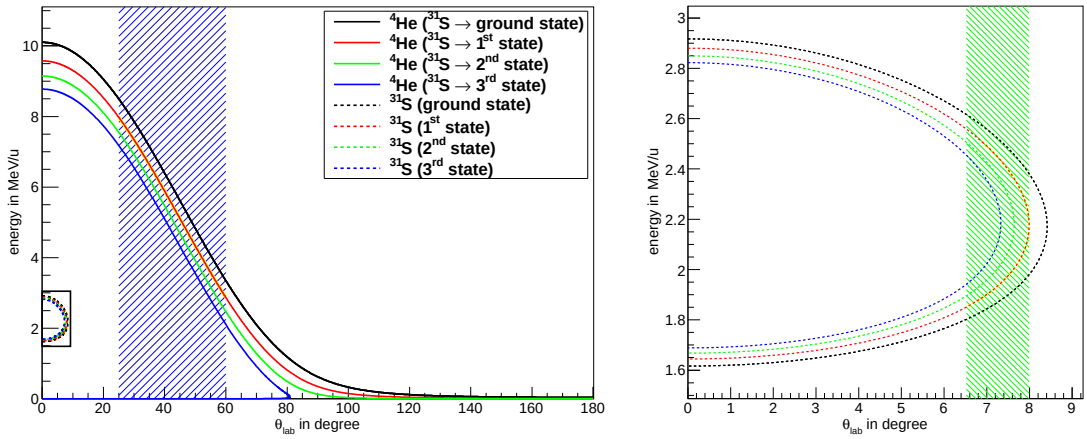

(a) (b)

Figure 2.6: The energy as a function of the polar angle for the outgoing particles of the transfer reaction ^{32}S(^{3}He,^{4} He)^{31}S in inverse kinematics at $E_{beam} = 85$ MeV. The polar angle θ_{lab} spans between the beam axis and the trajectory of the particle. (b) shows a zoomed range in (a). The blue band in (a) indicates the final covered polar angle range of the Si telescopes for the ^{4}He detection as discussed in section 2.5. The corresponding ^{31}S nuclei are indicated in (b) with a green band, where the first excited state in ^{31}S has been considered.

$$E_b^{1/2} = \frac{(m_a m_b E_a)^{1/2} \cos\theta_{lab} \pm \{m_a m_b E_a \cos^2\theta + (m_Y + m_b)[m_Y Q + (m_Y - m_a)E_a]\}^{1/2}}{m_Y + m_b} \tag{2.1}$$

with the energy E_i and masses m_i of the particle species $i\epsilon[a, X, b, Y]$, where a corresponds to the beam particle ^{32}S, X to the target nucleus ^{3}He and b and Y correspond to the outgoing particles ^{4}He and ^{31}S of the reaction. θ stands for the polar angle between the beam axis and the trajectory of the ^{4}He ejectile. Because the Q-value Q in the equation depends on the directly populated state in ^{31}S ($Q = Q_0 - E_{ex}$), the populated state can be determined by observing the polar angle and the energy of the ^{4}He ejectile. This in principle can be used in the DSAM experiment to assure that the excited state of interest in ^{31}S is directly populated and therefore the measured lifetime is not corrupted by feeding effects.

The kinematics of the transfer reaction in the lab frame have been calculated individually for the population of the ground state and the first three excited states in ^{31}S. Figure 2.6(a) shows four energy lines each for ^{4}He and ^{31}S nuclei, corresponding to the ground state (black) and the first three excited states in ^{31}S. The energies at a given polar angle θ_{lab} of the ^{4}He ejectiles corresponding to two neighbouring excited states are separated by more than 1 MeV, which in principle can be resolved in the Si detectors. If the angular resolution in the experimental setup is sufficient, the detected energy and polar angle θ_{lab} of the ^{4}He ejectile could be used to determine the directly populated state of the corresponding ^{31}S nucleus. Figure 2.6(b) shows a zoom on the

energy and angle range of the ^{31}S nuclei. Due to the inverse kinematics, only polar angles between 0° and 8° are possible, if the first excited state has been populated. This is important, because it limits the moving direction of the de-exciting ^{31}S nuclei in the DSAM experiment.

The relation between the polar angles in the lab frame of the trajectory of the ^{4}He ejectile that is detected and the trajectory of the corresponding excited ^{31}S nucleus that is stopped in the target, is shown in Figure 2.7(a). This relation is important to understand the observed Doppler shifts in a DSAM experiment, where a HPGe detector is positioned at 90° with respect to the beam axis as indicated in Figure 2.7(b). The covered solid angle of the ^{4}He particle detectors constrains the direction of excited ^{31}S nuclei whose γ-ray emission can be observed in coincidence. Figure 2.7(b) shows this situation in the horizontal plane in the lab frame. Here, the Si detectors cover polar angles between 25.0° and 60.0° (indicated in blue). The polar angular range of the corresponding excited ^{31}S nuclei is very narrow and covers angles between 6.5° and 8.0° (indicated in green). If a γ-ray emission is observed at 90° with respect to the beam axis, the observation angle with respect to the ^{31}S trajectory is actually between $(90.0 + 6.5)°$ and $(90.0 + 8.0)°$. Therefore the γ-ray is observed from backward angles and a Doppler shift to lower energies will be observed. If the opening angle of the HPGe detector is larger than 13°, some fraction of the detected γ-rays will be observed at forward angles ($< 90°$) as well, but the larger fraction will be observed in backward angles, causing a tail to lower energies in the E_γ spectrum.

2.5 The Yield Optimization of the Experiment

The yield of the experiment is determined by coincidences of detected ^{4}He ejectiles in the Si detectors and the observed γ-rays in the HPGe detectors outside the target chamber. The efficiency of the HPGe detectors will be discussed in chapter 3, but in general their efficiencies can be maximized by minimizing their distance to the target. The optimization of the position of the Si detectors for a maximum yield is more complicated, because it is affected by several constrains, which were discussed in the previous sections.

The differential cross section of the reaction ^{32}S(^{3}He,^{4} He)^{32}S was discussed in section 2.3 and a polar angle of 75° was considered for the position of the Si detectors. For the particle identification, the ^{4}He ejectile must have, after exiting the target, sufficient energy to deposit in the Si detectors to allow its identification and to trigger both the ΔE and E_{rest} detector. Unfortunately, the kinetic energy of the ^{4}He ejectiles in the range of polar angles close to 75° is relatively small ($\sim$ 4.75 MeV) as shown in Figure 2.6(a). Therefore, they can not penetrate the target and the ΔE detector, even if the target would be rotated to minimize the effective target thickness for the ^{4}He ejectiles.

The effective path lengths of the ^{4}He ejectiles in the target and the ΔE detector is determined by the polar angle θ and the azimuth angle ϕ of their trajectories (see Figure 3.2 for the definition of the coordinate system). Additionally, engineering issues that will be discussed in chapter 3 constrain the ϕ component in the detector position.

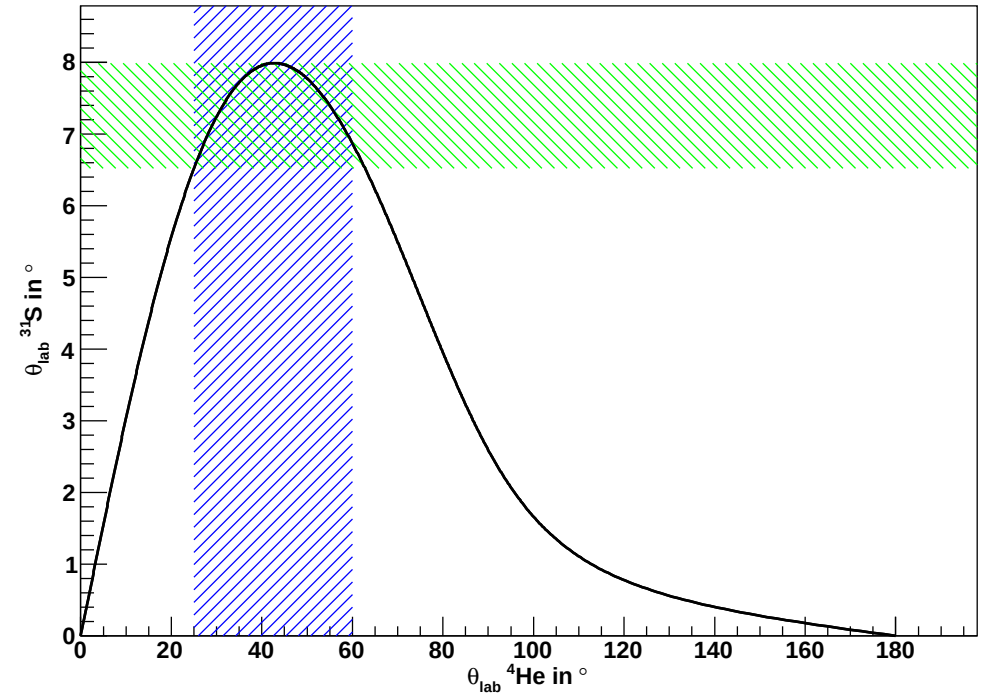

(a) The polar angle θ_{lab} of the direction vector of the excited ^{31}S nucleus as a function of the polar angle of the direction vector of the corresponding ^{4}He ejectile in the lab frame.

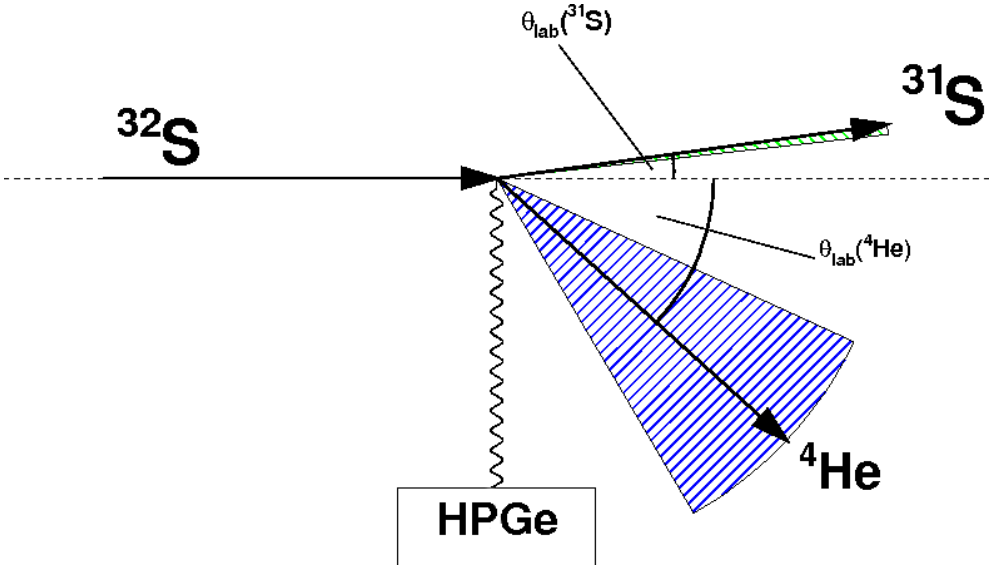

(b) Schematic diagram in lab coordinates of the scattering process of the transfer reaction in the horizontal reaction plane.

Figure 2.7: The angular correlation of the ^{4}He ejectiles and the corresponding ^{31}S* nuclei with an excitation energy of 1249 keV from the transfer reaction in inverse kinematics and at a beam energy of 85 MeV. The striped blue areas indicate the covered polar angles of the Si detectors in the commissioning experiment. The green striped areas indicate the range of the corresponding, excited ^{31}S nuclei. The polar angular range of the direction vectors of the ^{31}S nucleus is very narrow and is almost buried by the width of the drawn ^{31}S vector in (b).

The position where ^{4}He ejectiles have sufficient energy to penetrate the target and the ΔE detector and are stopped in the E_{rest} detector has been found at an angle of $(\theta, \phi) = (60°, 40°)$, when the 6.2 μm target is rotated by 54° with respect to the beam axis and a 50 μm thick ΔE detector is used. Due to the target rotation the effective thickness in beam direction is 10.5 μm which is sufficient to stop the ^{31}S nuclei as shown in sub section 2.2.1.

Taking into account the differential cross section to optimize the yield in the experiment, the upper edge of the detectors coverage in the polar angles is $\theta = 60°$. The lower edge in θ is then given by the geometry of the detector that will be discussed in sub chapter 3.3.2.

The proposed covered polar angular range ($\theta < 60°$) of the Si detectors, need to be evaluated by the cross sections of elastic scattering reactions of the beam with the target material (^{32}S +^{197} Au and ^{32}S +^{3} He, see Figure 2.5(b)). Due to the rotated target, elastically scattered ^{32}S nuclei are not stopped for all (θ, ϕ) angles that will be covered by the detectors, but are left with minor energies (few MeV). Therefore, a 6 μm Mylar foil is used to cover the ΔE detectors and stop those heavy nuclei. The energy loss of the ^{4}He ejectiles in the Mylar foil is small, but the detectors are not damaged by the high rate of low energetic ^{32}S particles. The rate of elastically scattered ^{3}He particles in the Si detectors is moderate and their detection can actually be used to monitor the ^{3}He content in the target as previously discussed in sub chapter 2.3.

Chapter 3

Experimental Design

One substantial work package of this thesis was the design and construction of a completely new experimental setup for lifetime measurements of excited states in nuclei, applying the Doppler shift attenuation method (DSAM, see section 1.7). The method uses a heavy ion beam and therefore, the setup has been installed at the tandem accelerator of the Maier-Leibnitz Laboratory.

This chapter describes the new experimental setup in detail. The setup is highly adaptable to experimental requirements, which is shown in the commissioning experiment where the lifetime of the first excited state in ^{31}S has been determined through the ^{32}S(^{3}He,^{4} He)^{32}S* reaction (see chapter 2).

3.1 The Maier-Leibnitz Laboratory

A nominal 14 MV tandem accelerator is used to provide ion beams at 13 experimental sites. The actual maximum voltage in 2011 was 13 MV. Many complex experiments and infrastructure for a large variety of applications in nuclear physics, nuclear astrophysics, biology and material science research are available, but no setup has previously existed to allow measurements of lifetimes of excited states in nuclei. A detailed overview of the scientific activities at the laboratory is given in the annual reports [MLL08].

A ground map of the laboratory is shown in Figure 3.1 [Har12]. The new DSAM setup is located in hall II at the beam line +10° (the site is marked in green).

The laboratory is operated by both Munich universities, the Technische Universität München (TUM) and the Ludwig-Maximilians-Universität (LMU). It is located on the campus of the Forschungszentrum Garching, Germany. Besides research groups of these two universities, many external scientists use the infrastructure and the tandem accelerator of the laboratory. The accelerator laboratory is an essential part of both clusters of excellence "Origin and Structure of the Universe" and "Munich-Centre of Advanced Photonics" (MAP) by the Deutsche Forschungsgesellschaft (DFG).

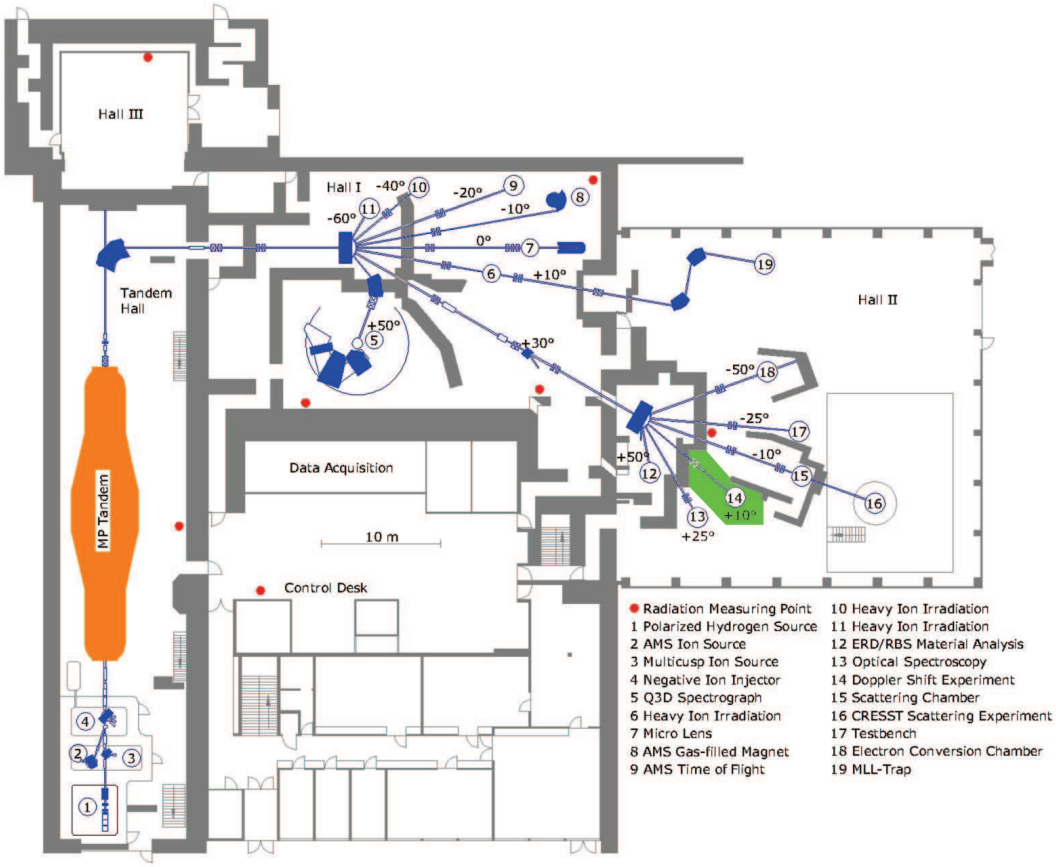

Figure 3.1: Ground plan of the Maier-Leibnitz laboratory [Har12] with the tandem accelerator (orange) and two switch magnets serving the beam lines. Dipole magnets are indicated in blue. The DSAM experiment is located at (14) in hall II, indicated in green.

3.2 The DSAM Setup at the MLL

The following sections describe the experimental setup in detail and show the adaptability of the setup according to the experimental requirements.

The design of the new DSAM setup has been developed, achieving several important criteria:

- **beam diagnostics**

  The DSAM uses an ion beam that needs to be focused on the target. A beam spot of minimum dimensions is required, to achieve a sufficient angular resolution in the detection of the light transfer ejectiles. Therefore, beam diagnostic components are necessary in the setup. Collimators that are mounted upstream of the target, cut away the halo of the ion beam (not used in the commissioning experiment because of a reduced transmission). A Faraday cup at the target position is used to focus the ion beam and measure its electrical current. For visual

diagnostic, a scintillator is used to visualize and therefore optimize the shape of the ion beam on the target.

- **vacuum**

  Due to the energy loss of charged particles in matter, a vacuum inside the target chamber and the beam line with $p < 10^{-6}$ mbar was provided. If the targets are cooled, such a vacuum is required to avoid contamination of the target surface due to the condensation of residual gas.

- **modular design for different reactions**

  Depending on the chosen reaction in future experiments, the configuration of the components in the setup varies. Therefore, a modular design is important that allows the use of additional particle detectors at variable positions as well as freedom in the target rotation that allows the optimization of the target thickness. As previously discussed, it must be sufficiently thick in the direction of the the excited nuclei, but as thin as possible in the direction of the emitted, light charged ejectiles.

- **maximum solid angle coverage of the HPGe γ-ray detectors**

  The HPGe detectors are positioned outside the vacuum chamber. In order to allow a maximum solid angle coverage and therefore maximize the yield of the experiment, the distance between the target and HPGe detectors must be minimized, which in turn limits the diameter of the target chamber and the inner space for the components such as the target ladder or the particle detectors.

- **particle detectors for the detection of light transfer ejectiles**

  A stack of a thin ΔE and a thick E_{rest} Si detector is used to form a detector telescope with which the identification of ejectiles is performed, along with measurements of their energy and their hit position on the detector telescope. The hit position on the detector and the beam spot center on the target determine the trajectory of the ejectile. Due to the two body kinematics of the transfer reaction, the energy and the polar scattering angle θ determine the directly populated state in ^{31}S. This in principle could be used to identify events of interest.

  The covered solid angle of the Si telescopes is adjustable to the experimental requirements such as cross sections and kinematics of the applied reaction.

- **multiple target positions**

  Multiple target positions are necessary to exchange targets that have been depleted of their implanted ^{3}He without venting the target chamber and loose valuable beam time. Also a blank target needs to be measured for background studies. Therefore, a so called target ladder is used that aligns several targets side by side. By moving the ladder up or down, different targets can be aligned to the beam axis.

- **target cooling for implanted targets**

  Because the DSA method requires stopping the excited nucleus (and beam) within the target, beam heating of the target occurs. Diffusion of the implanted ^{3}He nuclei becomes a problem with an increasing temperature. Therefore, cooling of the targets is necessary to eliminate diffusion otherwise caused by beam heating.

In the following chapters, a right handed coordinate system is used, defined as follows and shown in Figure 3.2. Its origin lies in the center of the target, with $\hat{z}$ defined anti-parallel to the direction of the beam. The direction of $\hat{y}$ is skyward. The polar angle θ_{lab} is defined as that angle between a direction vector $\vec{d}$ and the beam direction $-\hat{z}$. The azimuth angle ϕ_{lab} is defined between the projection of $\vec{d}$ into the x/y plane $\vec{d}_{\text{xy}}$ and the $\hat{x}-$ axis.

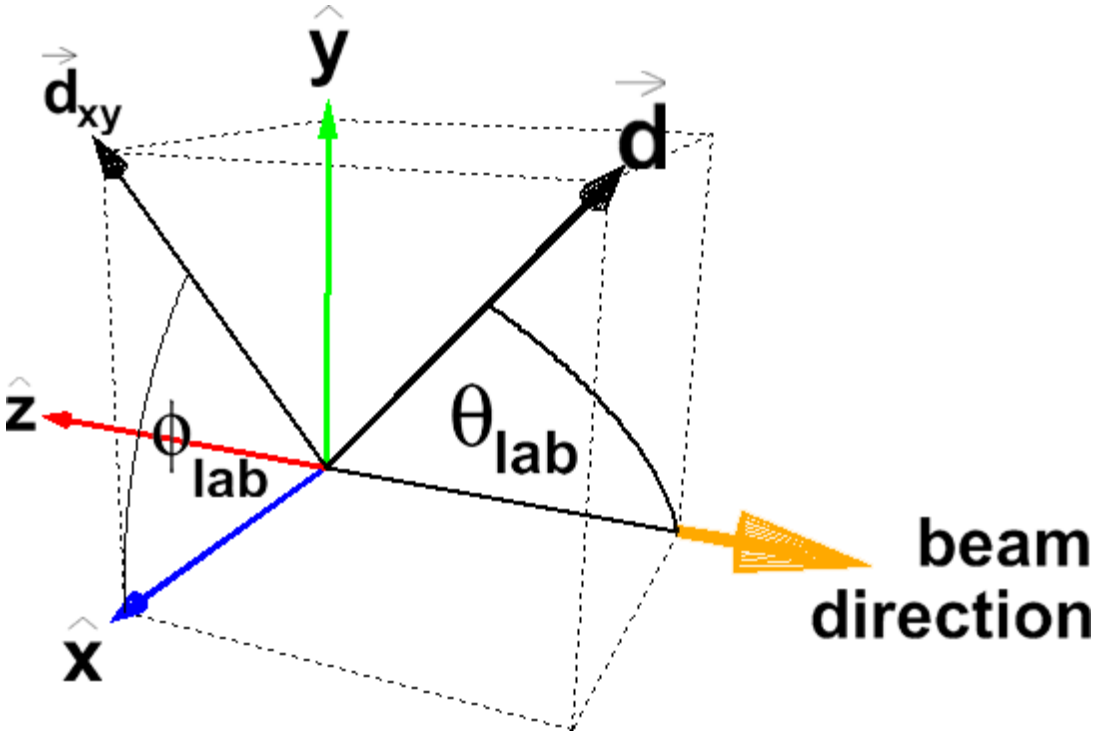

Figure 3.2: The definition of the applied, right handed coordinate system is shown. The origin is defined by the target center, the beam direction (orange) is anti-parallel to the $\hat{z}-$ axis (red) and the direction of the $\hat{y}$ axis (green) is skyward. The polar angle θ_{lab} is between a direction vector $\vec{d}$ and the beam direction $-\hat{z}$. The azimuth angle ϕ_{lab} is between the projection of $\vec{d}$ into the xy plane $\vec{d}_{\text{xy}}$ and the $\hat{x}$-axis (blue).

3.2.1 The Target Chamber Design

The DSAM facility at the MLL was designed in 2009 and 2010 using the computer-aided design (CAD) program SolidWorks [Das11]. Figure 3.3 shows a schematic overview of

the final design from the outside. It will now be described.

The upright cylindrical target chamber has a height of 200 mm and an outer radius of 77 mm. The walls were made of stainless steel (EN standard DIN 1.4541, X6CrNiTi18-10) with a thickness of 2 mm. The height of the chamber provides enough space to move a target ladder with multiple targets vertically and align different target positions to the beam axis. The radius provides enough space to position detector telescopes at various positions/distances from the target.

The bottom of the target chamber was closed with a base flange (CF DN-150) onto which all inner components such as the Si detectors and the target ladder are mounted (see Figure 3.4). The top of the target chamber was closed with a reduction flange (CF DN-150 - DN-100) and a glass window (CF DN-100) that allows viewing into the chamber and to look on the scintillation of the beam in a CsI crystal that is used for beam diagnostic.

The target chamber is connected to the beam line through a support chamber with CF DN-100 flanges (see Figure 3.3). The support chamber has four additional CF DN-100 flanges, where two of them are closed with blind flanges. The underside flange hosts a turbo vacuum pump (oerlikon MAG W 300); the upper-side flange hosts a LN_2 reservoir for the target cooling. A second turbo vacuum pump (Pfeiffer HiPace400) is attached to the beam line (95 cm upstream from the target, but not shown in Figure 3.3). A photo with an overview of the experimental site with three HPGe detectors aligned to the target chamber is shown in Figure 3.5.

The inner parts of the target chamber and the base flange are shown in Figure 3.4, where the ion beam enters from the right through the copper tube. The cooled target ladder can be slid up and down and is guided thermally isolated in two PEEK (polyether ether ketone) rails that are attached to the base flange with two aluminum U-profiles. The rotation of the target ladder with respect to the beam axis can be adjusted by concentrically rotating the base flange with respect to the target chamber and aligning the base flange bolt holes (see Figure 3.4) to the corresponding bolt holes in the chamber flange (see Figure 3.3). Due to the 20 bolt holes in the full circle, rotation angles of multiples of 18° are possible. A linear translator (huntvac, L-2111-4-SF) is used to vertically shift the target ladder in its rails without breaking the vacuum (see Figure 3.3). Therefore, a centered, 41 mm diameter hole was milled through the base flange, where a KF DN-40 - DN-16 reduction flange is mounted which holds the linear translator, whose shaft moves the target ladder. Due to the reduction flanges on the top of the target chamber and the reduction piece that holds the linear translator, the effective height of the target chamber that can be used for the target ladder is increased, allowing the use of the full lift of 100 mm of the linear translator. For thermal isolation, the interface between the target ladder and the metal shaft of the linear translator is made out of PEEK as well.

Two Si telescopes with a common mount were mounted on the base flange (see Figure 3.4), where 17 mounting positions are radially arranged with a polar angular separation of 5° between ±45° with respect to the normal vector of the target surface. The radial distance separating the plane of the Si telescopes and the target can be set between 30 mm and 70 mm (see also Figure 3.6(a)).

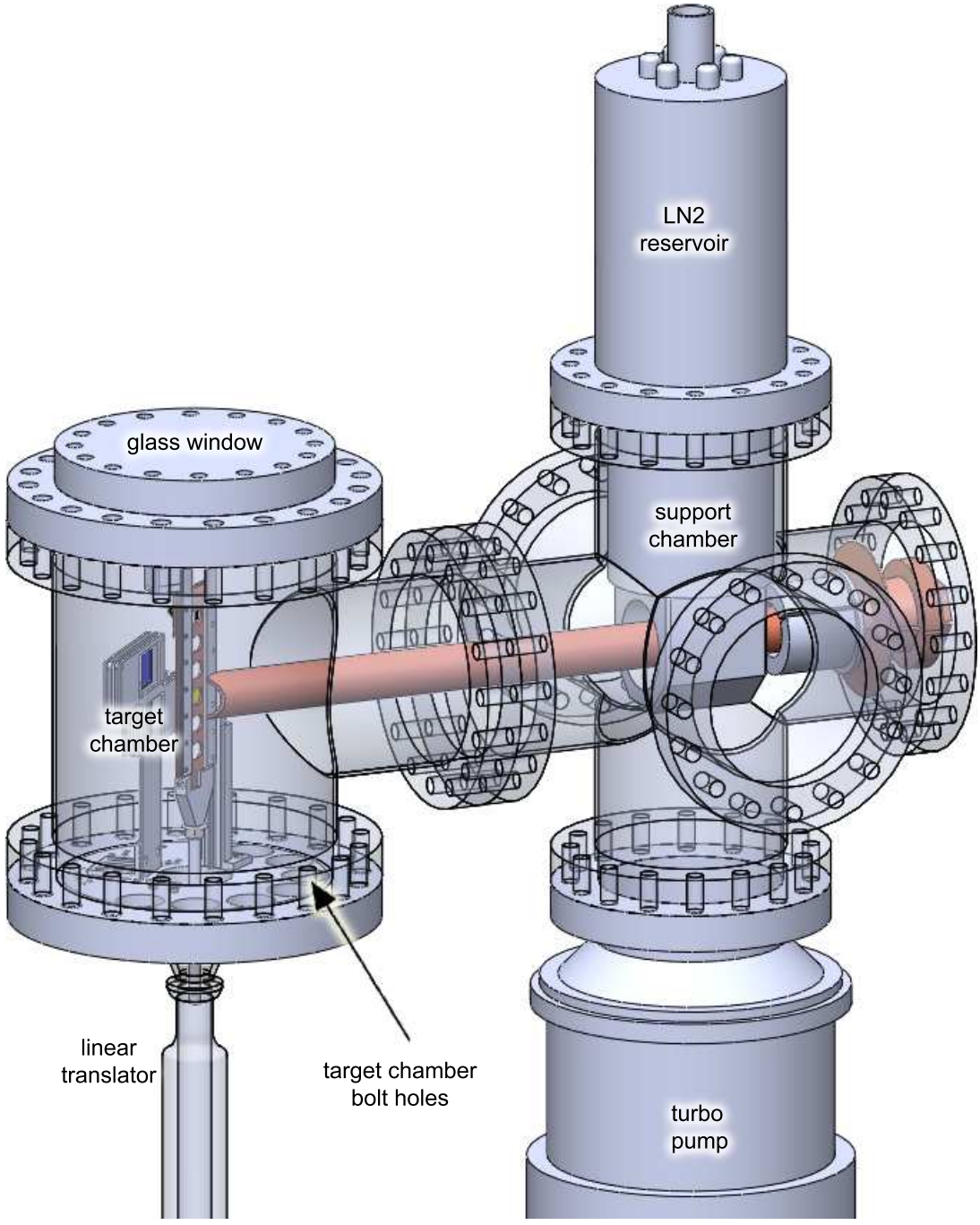

Figure 3.3: CAD drawing, showing a perspective side view on the outside of the target chamber and the support chamber. The linear translator allows to align different target positions of the target ladder to the beam axis. The LN_2 reservoir is in thermal contact with the copper tube that cools the target ladder. A turbo pump is mounted to the support chamber. For beam diagnostic, the glass window in the top flange of the target chamber allows to visually look into the target chamber.

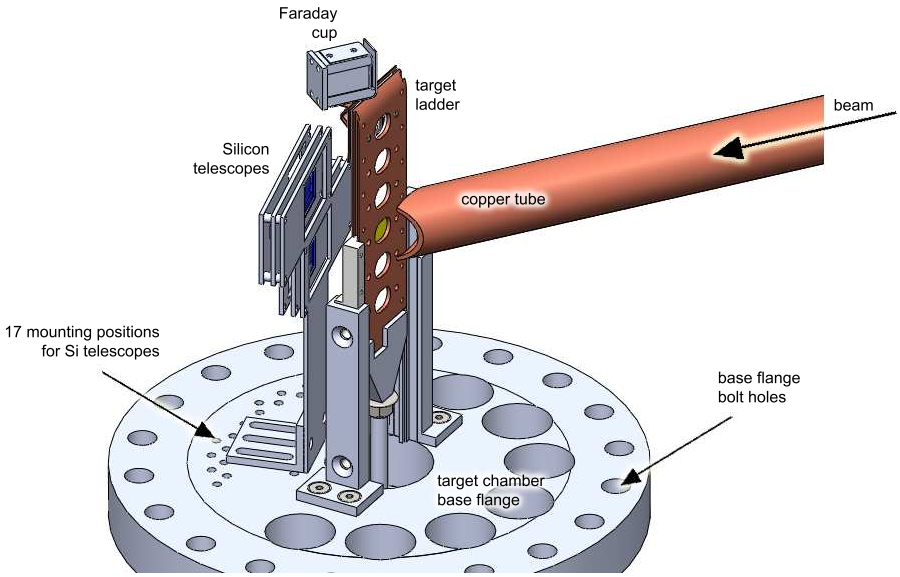

Figure 3.4: CAD drawing, showing a perspective side view on the base flange and the components inside the chamber.

Figure 3.6 shows the top view on the inside of the target chamber as a schematic diagram (a) and an actual photo (b). The beam comes from the right through the copper tube that is part of the target ladder cooling system which will be discussed in the next sub section. The base flange is rotated clockwise by 54° concentric to the target chamber and the Si telescopes are mounted at an angle of 15° (counter clockwise) with respect to the normal of the target surface. This results in a target rotation of 54° and an angle of the Si telescopes of $54° - 15° = 39°$ relative to the beam axis in a horizontal plane. Seven electrical LEMO feedthroughs in the base flange provide the necessary means by which to provide bias and signal cables to the Si detector telescopes and the components for beam diagnostic and temperature monitoring inside the chamber.

3.2.2 The Target Ladder and its Cooling System

As shown in Figure 3.4, the target ladder provides six target positions for standardized so called "Munich target frames" ($25.0 \cdot 12.5$ mm^2, made of aluminum or stainless steel). The ladder is made of copper which was chosen for high thermal conductivity. At each target position, the target ladder has a hole to permit transmission of reaction products, and a milled recess in the shape of the Munich target frame. This design then allows secure attachment with two screws of the target frame to the ladder in such a way to maximize surface area contact and, thereby, optimize thermal conductivity between the frame and the target ladder.

In order to cool the target ladder, two flexible copper braid cables are used to ther-

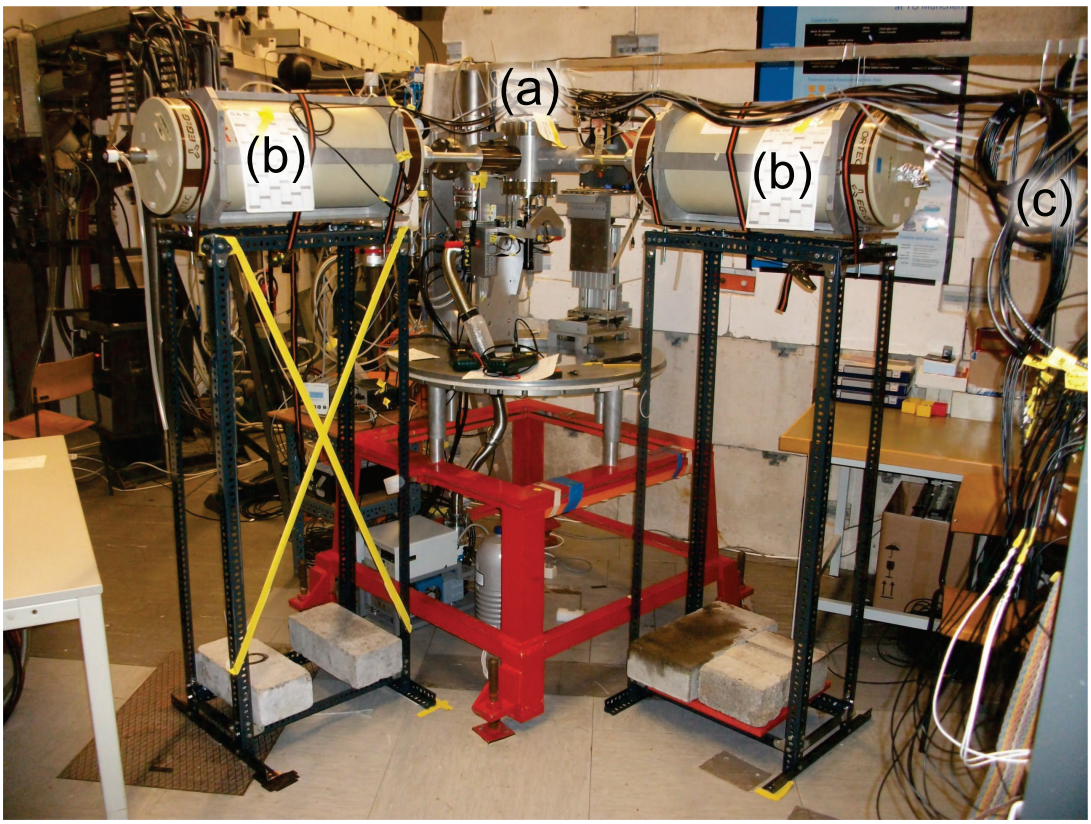

Figure 3.5: Photo of the experimental DSAM area. The stainless steal target chamber marks the end of the beam line (a). Three HPGe detectors (b) were aligned to the target at 0°, 90° and 110° with respect to the beam axis (only two detectors are visible in the photo). The cable bridge brings the preamplified signals to the data acquisition system (DAQ) in the rack on the right side of the picture (c).

mally connect the target ladder with the cooled copper tube (see photo in Figure 3.6(b)), which in turn is in thermal contact with the LN_2 reservoir shown in Figure 3.3 (see also Figure 3.7). The flexibility of the copper braids allows the target ladder the full vertical range of movement. Because a sufficient cooling of the target ladder is essential, those engineering challenging connections are now described in detail.

In general, an optimum thermal contact between two objects can be reached by maximizing their contact surfaces. Therefore, the copper braid cables were sandwiched between thin copper blades and the target ladder over the whole height of the ladder. The upper part of this connection is shown in Figure 3.7(a). The other ends of the copper braids are clamped to the copper tube with a pipe clamp as shown in Figure 3.6(b). The copper tube is centered in the beam line and is attached to a copper made cooling finger in the support chamber that is thermally coupled to the LN_2 reservoir. The connection between the copper tube and the cooling finger is shown in Figure 3.7(b). The cooling finger has a hole milled through it with a diameter of 49.6 mm and

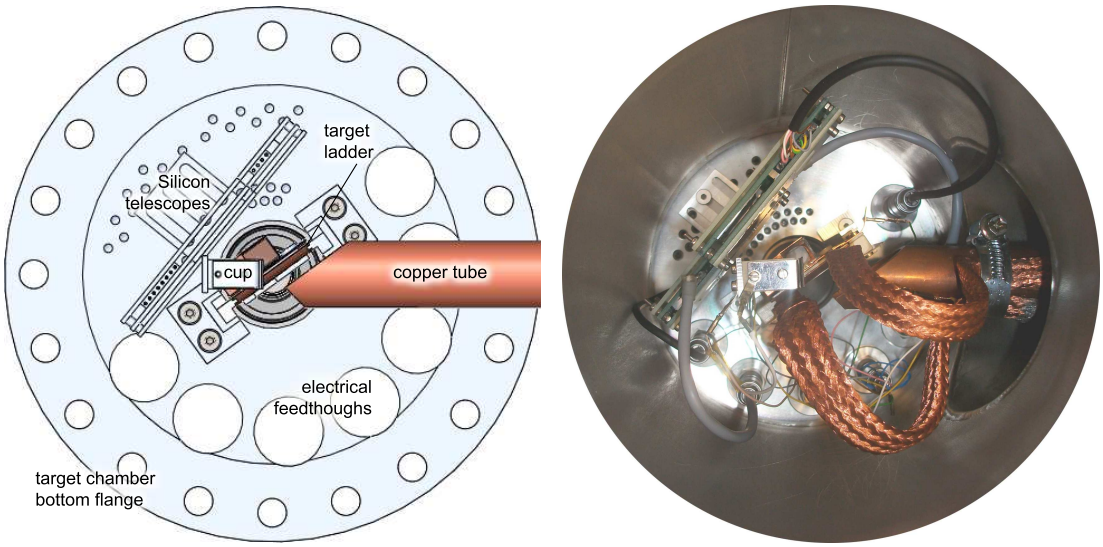

(a) Technical drawing (b) Photo

Figure 3.6: Top view on the inside of the chamber. The base flange is rotated by $\theta = 54°$ and the Si telescopes are mounted at an polar angle of $\theta = 39°$ in the horizontal plane. The beam comes through the cooled copper tube from the right. For the cooling of the target ladder, the thermal contact to the copper tube was achieved using flexible copper braid cables as shown in (b).

a female thread on the beam facing side. The copper tube with a diameter of 25 mm is thermally coupled to the cooling finger by means of an adapter comprised of two cones that fit into each other. A cylinder with an inner cone and a cone with an inner freed cylinder, housing the copper tube, were used (see Figure 3.7). The inner cone has been screwed into the cooling finger and therefore pressed the outer cone to the cooling finger. Since both components have been slotted lengthwise, a radial pressure was created that tightened the tube to the block.

The temperatures of the copper tube and the target ladder were monitored with PT100 resistors that were glued by "UHU - plus sofort fest" on the respective surfaces. The thermal coupling of the glue has not been studied, therefore the temperatures given in this thesis are upper limits. The filling level in the LN_2 reservoir was monitored with two additional PT100 resistors, sitting ~ 5 mm and ~ 150 mm above the bottom of the reservoir, respectively. If the lower resistor was measured to be above the resistance threshold for the corresponding temperature of LN_2, the reservoir needed to be refilled.

The chosen design has two advantages:

1. A thermal gradient causes the temperature of the target always to be higher than the temperature of the copper tube. Therefore the tube is more attractive for the condensation of residual gases, which alleviates the contamination of the target surface.

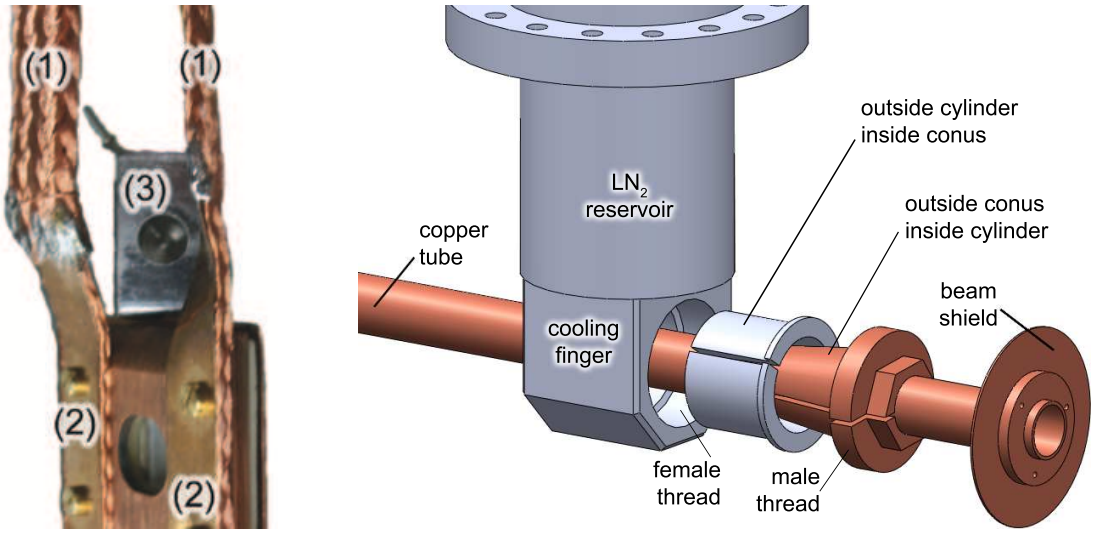

(a) Photo, showing the upper part of the target ladder from beam direction.

(b) The thermal coupling of the copper tube with the cooling finger. Additionally, a beam shield is mounted upstream on the copper tube.

Figure 3.7: The target cooling system: The LN_2 reservoir is thermally coupled to the cooling finger and the copper tube (b). Flexible copper braid bunds (1) were clamped to the copper tube on one side, and sandwiched between copper blades (2) and the target ladder on the other side (a). The Faraday cup (3) is mounted on top of the target ladder and aligned to the beam axis.

2. The surfaces of the cooling finger of the LN_2 reservoir and the copper tube act as cryo pumps. The effect could be observed in the chamber's pressure during the cool down cycle. Typically, the vacuum improved from $\sim 1 \cdot 10^{-6}$ mbar to $\sim 5 \cdot 10^{-7}$ mbar.

Condensation shrouds of similar design have been used in DSAM experiments by Alexander et al. [Ale81], Mythili et al. [Sch08] or Kanungo et al. [Kan06].

Starting the cool down cycle of the system at room temperature, the target ladder reached a temperature of $-115°$ C, typically within two hours. The lowest temperature of $-127°$ C without beam was observed after 3:40h of cooling. A typical cooling curve of the temperature as a function of time T(t) is shown in the appendix A.1.

With a deposited heat power of the ion beam $P_{heat} = 0.4$ W in the target, a LN_2 refill of the reservoir was necessary every ~ 8 hours. With this heat power, the target ladder temperature never rose above $-115°$ C. The temperature in the beam spot with a power of $P_{heat} = 0.5$ W was calculated with SolidWorks [Das11] and is found to be below room temperature, which is sufficient to prevent ^{3}He diffusion. For details, see Appendix A.2.

3.2.3 Beam Diagnostics

For beam diagnostics, a mini Faraday cup was mounted on top of the target ladder (see Figure 3.4 and 3.7 (a)). It can be aligned to the beam axis, moving the target ladder vertically. This design has the advantage that the Faraday cup is moved out of the way, if a target is bombarded and therefore has no effect on any γ-ray efficiency of the HPGe detectors, which are themselves situated in a horizontal plane centered on the target foil position. The Faraday cup is attached to the target ladder in such a way so that its entrance aperture is aligned with the incident beam, thereby ensuring correct measurements of the beam current at the target position.

When the ion beam enters the Faraday cup, it is stopped in a stainless steel stopper. During that process, secondary electrons are ejected. In order to reliably read the beam current, an electron suppression voltage has been applied to reduce that effect. Beside the Faraday cup current, the current from a shield in front of the Faraday cup were read and optimized during the beam tuning.

Optionally, two collimators made out of tantalum can be mounted electrically isolated in the copper tube and their currents from the beam halo can be read. This can be used to minimize the width of the ion beam during the beam tuning. A narrow beam width is preferable to reach a better angular resolution in the Si telescopes. A beam shield shown in Figure 3.7(b) assures that the beam can not bypass the copper tube to enter the target chamber.

An additional Faraday cup is mounted in the beam line $\sim$ 70 cm upstream of the target which is used in between the experimental runs to monitor the beam current.

For a visual diagnostic of the beam shape at the target position, the topmost target position of the target ladder holds a CsI crystal. The glass window in the upper flange of the target chamber allows one to observe the scintillation light of the crystal via a small mirror when the beam ions impinge on it. Since the position of the crystal does not differ from any of the other target positions, it is assured that the experimental targets will be exposed exactly to the same beam spot as observed in the crystal.

3.3 Detectors and Preamplifiers

An adequate choice of detectors is mandatory to measure the observables (see section 1.7) in a DSAM experiment. The following section justifies the choice of detectors for the γ-ray detectors and the charged particle detectors that have been used for the trigger generation for the data acquisition (DAQ). The characteristics of the detectors and their electronics are described in detail.

3.3.1 The High Purity Germanium Detectors (HPGe)

Three high purity germanium (HPGe) detectors with high efficiencies and good energy resolutions have been used for the detection of the emitted γ-rays under 0°, 90° and 110° with respect to the beam axis in a horizontal plane. These different observation angles will result in different line shapes in the E_γ spectra as described in section 1.7.

manufacture	Canberra	Ortec	Ortec
serial #	b 10540	37-N31120A	33-N40483A
bias voltage	-5000 V	-5000 V	-4500 V
crystal volume	~ 375 cm^2	~ 405 cm^2	~ 406 cm^2
crystal radius	79 mm	75.6 mm	75.6 mm
$(\theta, \phi)_{\mathbf{pos}}$	$(110°, 180°)$	$(90°, 0°)$	$(0°, 0°)$
distance	84.0 mm	83.5 mm	83.5 mm
efficiency @ 1332 keV	6.0×10^{-3}	5.7×10^{-3}	3.6×10^{-3}
$\epsilon(\mathbf{E}_\gamma)$ **parameter** a	0.30 ± 0.13	0.24 ± 0.11	0.13 ± 0.06
$\epsilon(\mathbf{E}_\gamma)$ **parameter** b	-0.541 ± 0.068	-0.522 ± 0.069	-0.497 ± 0.068

Table 3.1: The specifications and properties of the HPGe detectors are listed. The efficiencies are normalized to a distance of 84 mm between the detector surfaces and the γ-ray source at the target position inside the target chamber. The efficiency function ϵ(E) and its parameters are discussed in section 3.3.1.

All detectors are n-type and have a coaxial, cylindrical geometry. The fundamental properties of the detectors are listed in Table 3.1.

The distances between the surfaces of the HPGe detectors and the target chamber wall were minimized as quoted in Table 3.1 in order to maximize the detectors solid angle coverage and therefore optimize the γ-ray detection efficiency. Due to the chosen target rotation, the emitted γ-rays do not have to penetrate heavy material other than the target chamber wall and thus the detection efficiency is not greatly influenced.

The volumes and the radii of the crystals in the HPGe detectors differ, and individual characterizations have been accomplished concerning the energy calibrations, the photopeak efficiencies and the detector response functions. The studies were conducted with the configuration (distance to target / position) of the ^{31}S* experiment as quoted in Table 3.1, because the characteristics could be affected by the setup. The characterizations are described in the following subsections.

The preamplifiers of the HPGe detectors are attached to the detector housing and are partially cooled to minimize electronic noise induced by heat. Two output signals provide the energy signal and the timing signal with 93 Ω and 50 Ω termination, respectively. The processing of the analog signals and the data acquisition will be described in section 3.4.

The Energy Calibration of the HPGe Detectors

After the ^{31}S* experiment, energy spectra from three γ-ray sources (^{22}Na, ^{60}Co, ^{152}Eu) were acquired. The sources were sequentially mounted at the target position inside the target chamber. The distances between the HPGe detectors and the source were the same as during the experiment and are quoted in Table 3.1. The photo peaks in the acquired raw E_γ spectra were assigned to the known transition energies, resulting in

an energy calibration function for each detector. However, it was found in the analysis of the experiment that there was a small time variability of the energy scale (up to 2 keV over one week). This could be due to a thermal dependence of the detectors or the electronics. Therefore, individual calibration functions were necessary for each run of the beam time (a single run typically took one hour).

The energy calibration functions for each individual run have been determined using beam induced reactions and their γ-ray lines. These background reactions are mainly caused by fusion evaporation or coulomb excitation of the beam with the target material. Five γ-ray lines emitted from ^{39}K (346.69 keV, 783.36 keV, 1129.96 keV, 1773.98 keV, 2814.24 keV) and one γ-ray line from ^{197}Au (547.5 keV) have been used. Their known transition energies were plotted versus the centroids of the six photo peaks that were determined by fitting them with Gaussian line shapes.

The energy calibration plots (E_γ vs. ADC bin number) showed minor non-linear effects in the source data as well as in the beam time data, and therefore 2nd order polynomial calibration functions were necessary to align the energy scales of all three detectors in the full energy range.

The Response Functions of the HPGe Detectors

A sufficient characterization of the HPGe detector response functions is mandatory for the analysis of a DSAM experiment and the modeling of the Doppler effected line shapes in the E_γ spectra (see subsection 4.3.3).

The response function of a HPGe detector and its signal processing electronics is defined by the peak shape in the E_γ spectrum of an observed quasi mono energetic γ-ray source. Due to the statistical processes in the γ-ray detection in the HPGe crystal, the detector response function of an ideal detector can be usually characterized with a Gaussian.

Additional effects such as crystal defects, thermal processes or electron/hole recombination cause discrepancies to the Gaussian function of an ideal HPGe detector. The electronic signal processing creates an additional energy spread due to electronic noise in capacities and resistors. All these mechanisms create small statistical fluctuations in the measured signal amplitude that can result in tails or asymmetries of the peak shape in the acquired E_γ spectrum. Determining the response function of a detector setup means finding an empirical function that fits the line shape of the E_γ spectrum while attempting to model these effects.

The E_γ spectra of a ^{152}Eu γ-ray source that, was positioned at the target position of the setup, were acquired in the configuration of the ^{31}S experiment (see Table 3.1). The HYPERMET function [Phi76] was used to characterize the detector response functions of the three used HPGe detectors in the experimental setup. It is a sum of a symmetric peak function, a tail function and a linear background function:

$$\mathrm{HYPERMET(E)} = f_{\mathrm{sym.}}(\mathrm{E}) + f_{\mathrm{tail}}(\mathrm{E}) + f_{\mathrm{background}}(\mathrm{E}) \tag{3.1}$$

The detailed mathematical function is given and the fitted data for the three detectors is shown in appendix A.3. Besides a linear background and the centroid for the peak

shape $E_{peakpos}$, four additional parameters describe the peak shape.

Because the detector response function can be energy dependent, the 1112 keV line in ^{152}Eu has been chosen to characterize the peak shape, since its energy is very close to that of the 1249 keV line from the first excited state in ^{31}S. The number of rejected events due to the dead time of the data acquisition system (DAQ) was smaller than 4.3%. The fitted functions are plotted in the appendix A.3 and the characteristic parameters are quoted. The obtained response functions are used in the analysis to model the Doppler affected line shapes in the E_γ spectra.

Detailed studies of the characteristics of the used HPGe detectors can be found in [Fie10] and [Hei11].

HPGe Detector Photopeak Efficiencies

Nine γ-ray lines from ^{152}Eu (MLL pool - source ID: 507-86, 976 Bq, 4. August 2011) were used to determine the γ-ray photo peak efficiency of the detectors in the setup configuration of the ^{31}S* experiment. The source was mounted at the target position inside the chamber and the distances between the HPGe detectors and the source were the same as during the experiment and are quoted in Table 3.1. The photopeaks were fitted with the HYPERMET function and the area under the function, after background subtraction, was determined and normalized to the run time. The emission probabilities per decay were taken from [Deb79]. Figure 3.8 shows the photopeak efficiencies of the three detectors as a function of the γ-ray energy. The data has been fitted with the function $\epsilon(E_\gamma) = a \cdot E_\gamma^b$ with the free parameters a and b that are quoted in Table 3.1.

Even though the volumes of the germanium crystals of the three detectors were comparable (see Table 3.1), the efficiency of the Ortec detector at 0° (# 33-N40483A) is reduced by a factor of $\sim$ 0.7 compared to the Canberra detector at 110°. The ^{152}Eu measurement is consistent with observations of the natural background radiation (609.3 keV, 1120.3 keV, 1764.4 keV from ^{214}Bi and 1460.8 keV from ^{40}K). The lack of efficiency in this detector is not understood. Nevertheless, no distracting effects have been observed in the energy resolution or the detector response function. The yield of the ^{31}S* commissioning experiment was high enough to compensate this effect.

3.3.2 The Charged Particle Detectors

The charged particle detection in the Si telescopes was used to generate the trigger for the data acquisition and find charged particle - γ coincidences. The use of $\Delta E/E_{rest}$ Si telescopes allows the particle identification and therefore the background reduction in the E_γ spectra. Due to the limited space (γ-ray efficiency) in the target chamber, a compact design is necessary. Low noise, and a good energy and position resolution of the detectors is important for the offline analysis of such an experiment. The detection position and the target determine the particle's trajectory. This allows the correction for the effective thickness of the ΔE detector, which is important for the particle identification. Also, if the angular resolution of the setup is sufficient, the kinematics of the transfer reaction can be used to determine the directly populated state of the excited

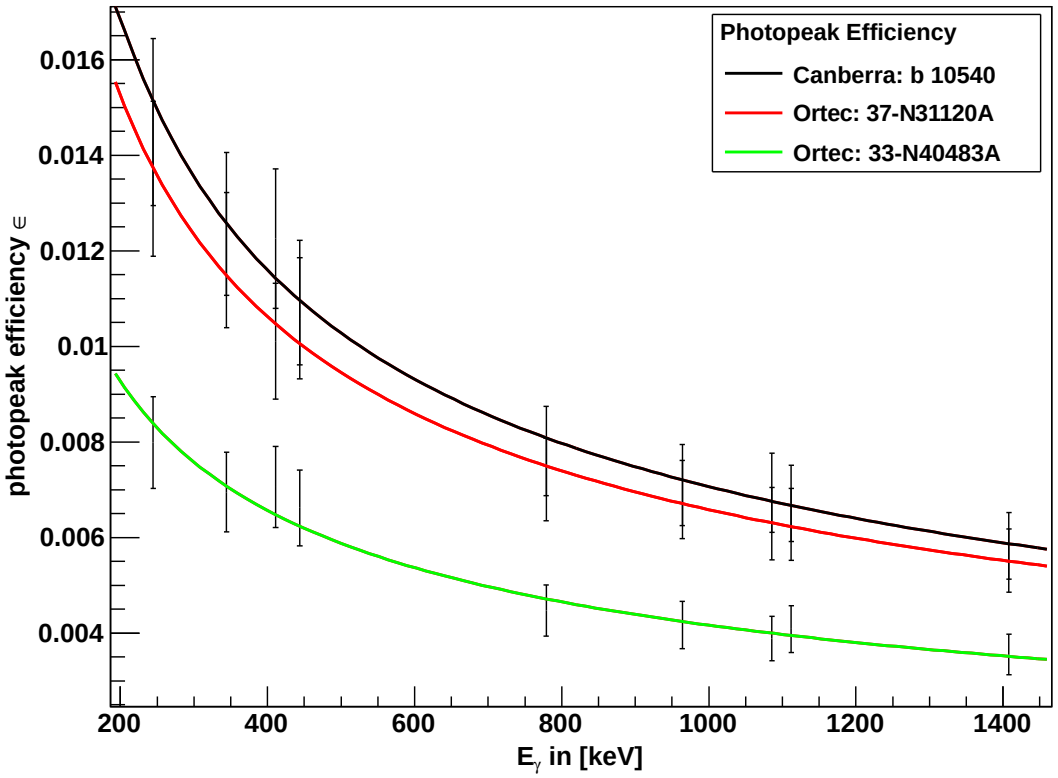

Figure 3.8: The photopeak efficiencies of the HPGe detectors as a function of the γ-ray energy. The data points were acquired with a ^{152}Eu source and are normalized to a distance between the source and the detectors surfaces of 84 mm. The data has been fitted with the function $\epsilon(\mathrm{E}_\gamma) = a \cdot \mathrm{E}_\gamma^b$ with the free parameters a and b. The errors are dominated by the uncertainty in the distance between the detectors and the source.

nucleus of interest as shown in section 2.4.

The following describes the design and the characteristics of the Si telescopes that have been used.

Two identical telescopes each with an active area of $20 \cdot 20$ mm^2 have been mounted symmetrically around the horizontal plane in the height of the beam axis. A minimum distance of 10 mm between the active areas of the telescopes is caused by the design of the custom made PCB boards that host the Si chips. The displacement and the normal vectors of the detectors surfaces, positioned at the geometric center of each detector are given by $\vec{n} = (0, \pm 15 \text{ mm}, 0) + (d \ \sin(\theta_{\mathrm{Si}}), 0, -d \ \cos(\theta_{\mathrm{Si}}))$, where $d = 34.6$ mm is the distance between the plane of the position sensitive $\mathrm{E}_{\mathrm{rest}}$ detectors and the target in the x/z plane (see Figure 3.2). θ_{Si} is the polar angle of the center of the detectors projected in the x/z plane.

For charged particle identification, each telescope is composed of a set of a thin ΔE and a thick, position sensitive $\mathrm{E}_{\mathrm{rest}}$ detector. A 6 μm Mylar foil was also mounted in front of the ΔE detector to protect the ΔE from low energetic beam particles that

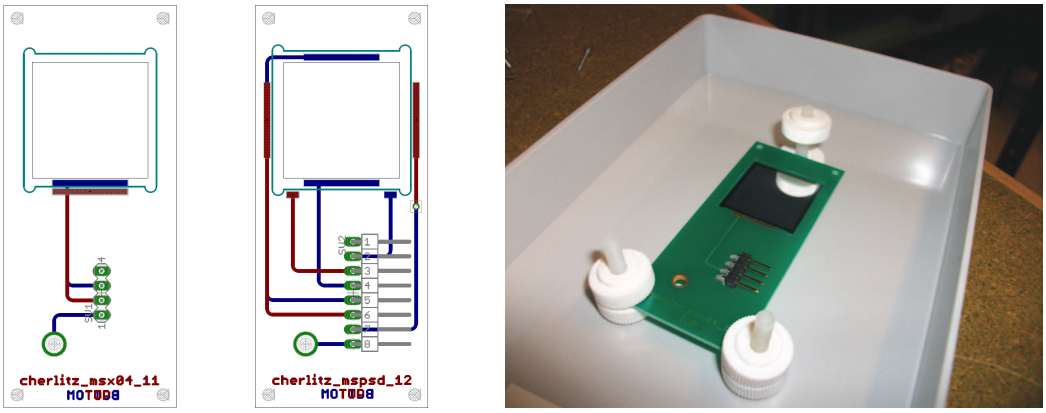

(a) (b)

Figure 3.9: The layout of the PCB boards that host the Si chips is shown in (a) for the MSX04 ΔE (left) and the MSPSD E_{rest} (right) detectors. Red and blue lines indicate circuit paths on the front and back side of the board, respectively. The chip is recessed in the board and was bonded to soft gold pads. (b) shows a photo of a mounted MSX04 chip on its custom made PCB board.

could be scattered out of the target.

Figure 3.9(a) shows the schematic design of the custom made PCB boards ($70 \cdot 30\text{mm}^2$) that host the ΔE and E_{rest} Si chips. The boards were designed with EAGLE (Easily Applicable Graphical Layout Editor) [Cad10]. A complete Si telescope provides five signals with the energy information in the ΔE and E_{rest} detectors and the hit position of the E_{rest} detector (1 ch - MSX (ΔE), 4 ch - MSPSD (E_{rest})). Figure 3.9(b) shows a photo of a mounted ΔE Si chip in the according PCB board.

The silicon chips have been manufactured and mounted on the PCB boards by "Micron Semiconductor Limited" [Mic11]. The fundamental specifications of each detector are listed in Table 3.2. Depending on the experimental requirements (particle identity and kinetic energy), the thickness of the installed ΔE detector can be chosen to be 52 μm or 241 μm to achieve optimal particle identification. The thickness of the E_{rest} detectors is 997 μm.

Duo lateral (DL) position sensitive detectors (PSD) have been chosen for the E_{rest} detectors because of their low number of readout channels. The method of the position and the energy measurement is explained in the following for a one dimensional detector.

Figure 3.10 shows the simplified equivalent circuit of a one dimensional position sensitive detector (PSD). The upper surface has a resistive layer and contacts on the left and right side allow to measure the charge, flowing to the left Q_{left} and right Q_{right}, respectively. The resistors R_i substitute this continuous resistive layer on the surface and the capacities C_i substitute the p-/n depletion layer inside the Si chip. If a charged particle hits the detector, it deposits energy that creates electron/hole pairs in the depletion layer. Due to a reversed bias, the thickness of this layer is increased

model	serial #	thickness	purpose	nom. V_{depl}
MSPSD DL20-1000	2589-1-3	997 μm	$\mathrm{E_{rest}}$	105 V
MSPSD DL20-1000	2589-1-4	997 μm	$\mathrm{E_{rest}}$	105 V
MSX04-50	279-18A	52 μm	ΔE	5 V
MSX04-50	2794-18-2	52 μm	ΔE	5 V
MSX04-250	2447-15A	241 μm	ΔE	10 V
MSX04-250	2447-15-2	241 μm	ΔE	10 V

Table 3.2: Properties of the silicon detectors, manufactured by Micron Semiconductors ltd. All chips have an active area of 20×20 mm^2. The $\mathrm{E_{rest}}$ detectors are position sensitive.

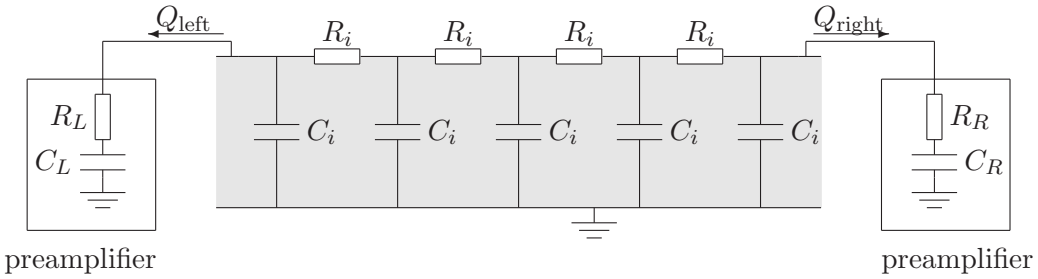

Figure 3.10: Principle of a 1-dimensional position sensitive detector (PSD) using the charge division in a resistive layer. See text for details.

and the created charge carriers (electrons and holes) are extracted to the surfaces of the detector. The resistance along the upper surface causes a charge division to the contacts on the left and right side of the detector. The total charge divides inverse proportionally to the integrated resistance on the left and on the right side of the hit position.

The total deposited energy is proportional to the total charge $\mathrm{Q_{total}}$. The total charge and the relative hit position can be determined applying the formula:

$$\mathrm{Q_{total}} = \mathrm{Q_{left}} + \mathrm{Q_{right}} \qquad \mathrm{pos} = \frac{\mathrm{Q_{right}} - \mathrm{Q_{left}}}{\mathrm{Q_{total}}} \tag{3.2}$$

The used $\mathrm{E_{rest}}$ detectors apply the described method in two dimensions, where the position in X is determined by charge division on the front surface and Y is determined by charge division on the back surface. The integrated resistances on the back and front side were $\mathrm{R_{back}} \approx 2.3$ kΩ and $\mathrm{R_{front}} \approx 1.15$ kΩ, respectively.

Higher order effects of the detector and the charge sensitive preamplifiers cause non linear effects on the determined hit position and a position dependence of the determined energy. The effects have been corrected, but are smaller than the resolution of the experimental setup (see A.5). The corrections are discussed in the appendix A.4.

Resolution studies of the same type of MSPSD detectors ($20 \cdot 20\mathrm{cm}^2$) show that a

position resolution of 200 μm can be achieved [Soi10]. This corresponds to an angular resolution in the polar angle θ of the detectors in our setup between 0.3° and 0.2°. Nevertheless, it will turn out that the angular resolution of the setup is limited by the beam spot width, as it is shown in appendix A.5.

3.3.3 The Charge Sensitive Preamplifiers

The two Si telescopes with seven channels each have been connected with custom made LEMO cables (length = 30 cm) and feedthroughs to individual preamplifier units outside the target chamber. Custom made circuit boards were designed to drive seven industrial preamplifier modules with low electrical noise properties. The units are based on standard "CREMAT Model 110" single channel hybrid modules [Cre11] in a well shielded massive aluminum housing. This concept was chosen to make use of the excellent noise qualities of the CREMAT and to provide a large flexibility in the choice of different amplification ranges, meeting experimental requirements.

An AC-coupled arrangement has been chosen for the custom made circuit boards that allows changing the load resistance without changing the preamplifier input (see [Kno99]).

Additional serial resistances (schematic R_L and R_R in Figure 3.10) for the individual channels of the MSPSD detectors have been installed between the detector and the input of the CREMAT modules (1.0 kΩ x-channels, 0.7 kΩ y-channels). This is mandatory to improve the position resolution of the detectors and to avoid oscillations of charges between the CREMAT modules.

A low voltage power supply has been provided to the units with a standard RS232 cable from a NIM module (Mesytec MNV-4 [Mes13]). In order to monitor the individual leakage currents of the Si detectors, the detector bias voltages have been provided by a NIM module (Mesytec MHV-4 [Mes13]) to each detector individually.

3.4 The Data Acquisition (DAQ) and the Electronics

The data at the DSAM facility is acquired with a "Versa Module Eurocard" (VME) bus system, using a 12 bit peak sensing analog-to-digital-converter (ADC, Caen 785), a 12 bit time-to-digital-converter (TDC, Caen 775) and a scaler (SIS 3820). A PowerPC (PPC) and a trigger module (GSI Triva) serve as the interface to the computers and the servers in the local area network (LAN). The readout software "Marabou" [Lut11] is used, which is maintained by the computer group at the MLL and employs the "Multi Branch System" (MBS) developed at the Helmholtzzentrum für Schwerionenforschung (GSI) in the backend to communicate with and read the VME modules. For the online analysis during the experiment, the visualization program "HistPresent" is used. It is based on ROOT [Bru97] and is maintained by the MLL computer group as well [Sch11].

The preamplified energy signals from the Si and the HPGe detectors are pre-processed by analog electronics, before the ADC can be employed to digitize the signal amplitudes. The following section describes the configuration during the $^{31}S^*$ experiment and shows how the analog signals have been processed and how the logical signals have been

produced to establish a trigger logic. A schematic diagram is presented in Figure 3.11. In addition to the ADC, the TDC has been employed to identify the trigger source in the HPGe detectors.

The silicon telescopes provide five signals each (1ch MSX04 ΔE, 4ch MSPSD E_{rest}), which were preamplified (see 3.3.3) and then fed into a 16-channel shaper NIM module (Mesytec MSCF-16 [Mes13]). Besides the analog signal shaping, the module discriminates the signals separately and provides the common Si trigger obeying multiplicity settings. A multiplicity of n is given, if n channels trigger in coincidence within a given time window. Using both telescopes, a multiplicity of $2 \leq n \leq 8$ (of 10 possible channels) has been required to discriminate events with sufficient information for a $\Delta E/E_{rest}$ particle identification. If the readout system is ready (no PPC veto), the common Si trigger is used to provide the global trigger for the DAQ. The schematic trigger logic is shown in Figure 3.11.

The global trigger is used to create the gate for the ADC of all energy channels of the Si detectors and the HPGe detectors, start the TDC measurement (common start, individual stops), load the next event in the scaler and trigger the readout of all VME modules via the PPC.

The HPGe detectors (see 3.3.1) have built-in preamplifiers, each providing a timing and an energy signal. The energy signals were shaped with spectroscopy amplifiers (Silena Milano, AMPLIFIER MOD 7614) before they were fed into the ADC. The timing signals were processed discretely in timing filters (ORTEC 474 / ORTEC 579) and discriminated (Phillips Scientific, 730 Tri-Mode Discriminator) to provide logic signals. These logic signals have been delayed and were used to stop the individual TDC time measurements that have been started by the global trigger. As a consistency check, one TDC channel has been stopped by the delayed TDC start signal. The TDC data will be used to identify which HPGe detector has detected a γ-ray in coincidence with a charged particle in the Si telescopes.

All logical signals (common Si, HPGe and logic conjunctions) were monitored with the scaler module (32 channels, SIS 3820) to monitor the dead time of the system or to identify unexpected noise in certain detector channels.

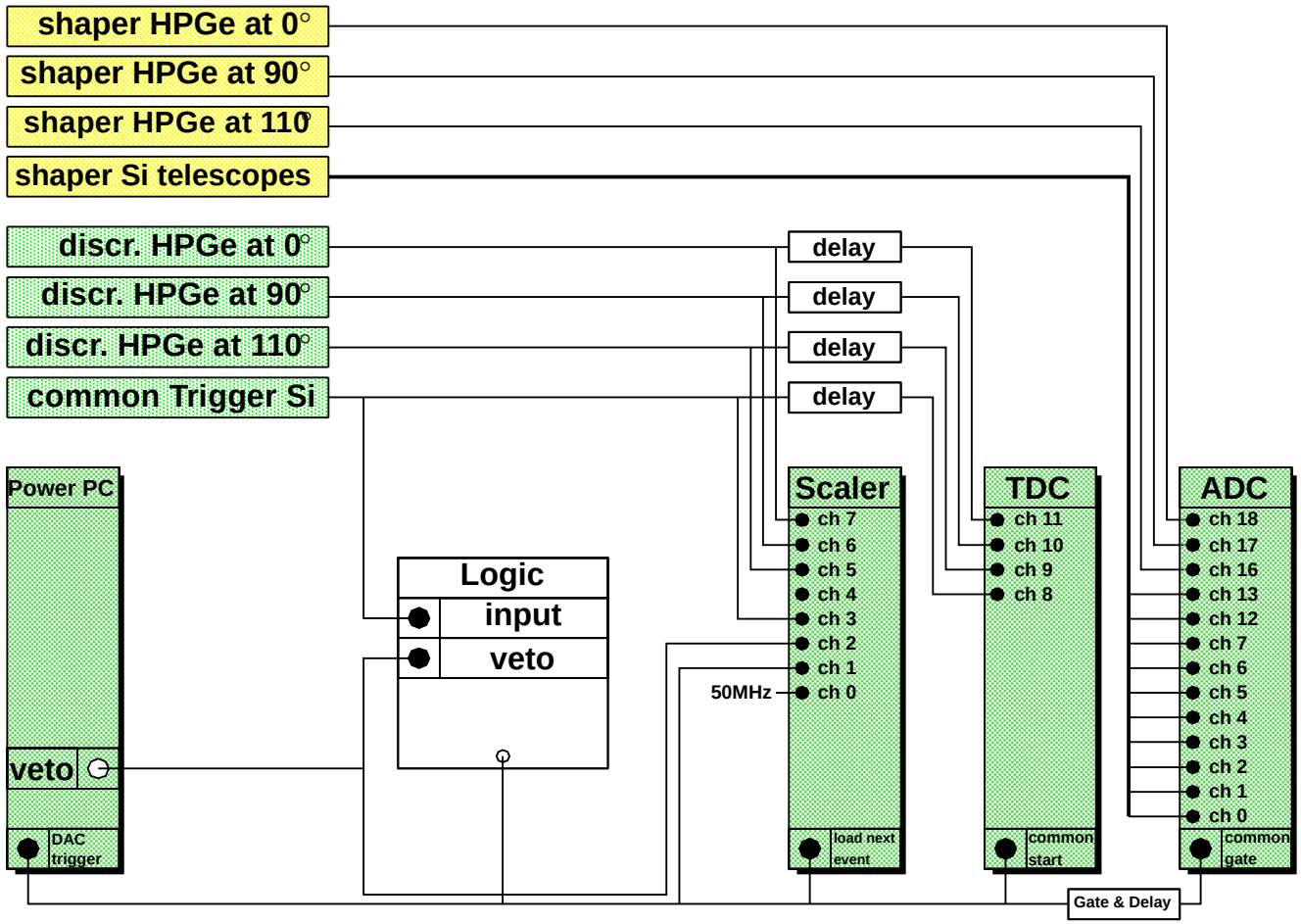

Figure 3.11: The schematic trigger logic. See section 3.4 for a detailed explanation.

Chapter 4

Analysis

This chapter describes the methods by which the Doppler shifted γ-ray spectra were extracted from the raw data, and the model by which these spectra were fitted to obtain the lifetime of the first excited state in ^{31}S.

4.1 The Data of the Beam Time: July / August 2011

The commissioning experiment was performed between the 28$^{\text{th}}$ of July and the 3$^{\text{rd}}$ of August, 2011. A ^{31}S beam (charge state 8^+) with 85 MeV was used to acquire more than 90 hours of data from the ^{32}S(^{3}He,^{4} He)^{31}S* reaction, using three ^{3}He implanted gold targets. More than 32 hours of beam data was acquired from gold targets with no implanted ^{3}He particles (which, for future reference, will be called "Au-only") for γ-ray background studies.

On average, the electrical beam currents were 18.3 enA and 50.0 enA for the ^{3}He and Au-only runs, respectively. The higher beam currents for the Au-only targets were reasonable, because no diffusion of the target material was possible. The time integrated beam current (beam current $\times$ time), between the two target types, is comparable and therefore statistics are comparable as well. This allows a background subtraction of the E_γ spectra in the offline analysis.

The beam spot at the target position was determined using a scintillating CsI crystal, and was found to have the shape of an ellipse with a vertical diameter of 4 mm and an horizontal diameter of 3 mm. The product of the beam current and the ^{3}He target area density (S ions s^{-1} $\times$ ^{3}He cm^{-2}) was monitored with the Si telescopes via elastic scattered ^{3}He particles. Figure 4.1 shows the online monitored rate of ^{3}He particles in the Si detectors. A small cut on a fraction of the ^{3}He particles in the particle identification plot has been set and the number of entries were integrated after each run and normalized to the beam current and the run time. Because ^{3}He and ^{4}He particles could not be discriminated from each other in the online analysis, some ^{4}He particles were taken into account. The data points in Figure 4.1 are connected with a line to guide the eye. If Au-only targets were used for background studies (red), rates below 10 (pnA s)$^{-1}$ were observed.

In order to maximize the used area of each target, the targets were used with the center of the beam initially focused on the center of the target followed by downward

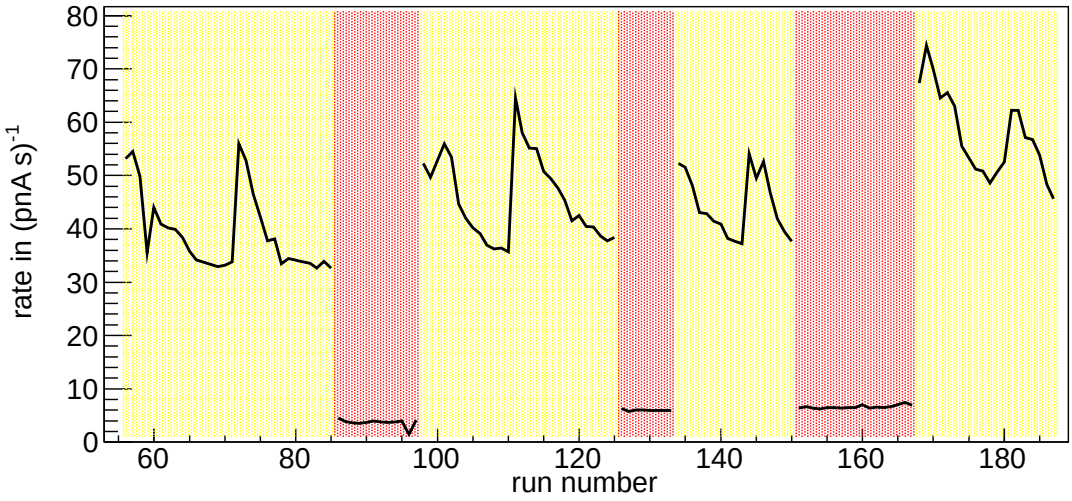

Figure 4.1: The normalized rate of elastically scattered ^{3}He particles as a function of the run number. The given rates need to be interpreted relatively. The yellow and red bands indicate the use of ^{3}He and Au-only targets, respectively.

and upward shifts in the target position by 2 mm, when it was determined that ^{3}He depletion justified the change in position. At 2.3 pnA of beam current, the target position was changed every $10 - 12$ hours.

The temperature measured by a PT100 resistor attached to the target ladder was never higher than 157 K $= -116°$ C for the ^{3}He runs and 166 K $= -107°$ C for the Au-only runs, respectively. The increased temperature for the Au-only runs was caused by the higher beam power for those runs.

The vacuum was monitored with a vacuum gauge, and the pressure was never higher than $1.2 \cdot 10^{-7}$ mbar.

The majority of data in this experiment has been acquired, triggering on charged particles. Half an hour of beam time has been used to trigger on γ-rays or charged particles.

4.2 The Processing of the Experimental Data

The E_γ spectra from the three HPGe detectors, positioned at different polar angles (see Table 3.1), provide the Doppler shifted line shapes, which are connected to the lifetime of the observed de-exciting state. The raw E_γ spectra were filled whenever a charged particle (p, d, t, ^{3}He, ^{4}He) hit one of the Si telescopes. Due to the chosen reaction channel ^{32}S(^{3}He,^{4} He)^{31}S, only events which were triggered by ^{4}He particles can be correlated to the reaction of interest.

All events that were triggered by other particles than ^{4}He can be rejected, thus enabling background reduction in the E_γ spectra. The following section describes how this background is subsequently reduced and subtracted by using all the available

	ADC	TDC	scaler
Si telescope1 Si telescope2	$\Delta E + E_{rest}$ + position $\Delta E + E_{rest}$ + position	delayed stop	# triggers
HPGe Canberra	E_γ	stop	# triggers
HPGe Ortec90	E_γ	stop	# triggers
HPGe Ortec00	E_γ	stop	# triggers

Table 4.1: Set of information in a single data event, triggered by one of the Si telescopes. The scaler has been used for the rate monitoring. See also section 3.4.

information stored in the event structure.

The data processing is done using the script language ROOT [Bru97], which allows handling of large amounts of experimental data. In total, 20 Gb of data was acquired from runs with ^{3}He implanted gold targets and the Au-only target. Each event in the data stream provides the set of information which is shown in Table 4.1. The detailed wiring of the ADC, the TDC and the scaler in the electronic setup is described in section 3.4. As described previously, the scaler data was acquired for rate monitoring of the detectors and consistency checks in the DAQ, but has not been used in the following lifetime analysis.

Using the combined information from the TDC and ADC modules, background events can be identified and therefore rejected, as will be shown next.

4.2.1 The TDC Data

Due to the global trigger in the electronic setup, the individual raw E_γ spectra have been filled in all cases, including those cases where no valid energy signal was pending. In this context, "not valid" means that the shaped energy signal did not achieve a maximum within the ADC gate. Such events have been identified by the TDC measurements and were rejected from the final analysis. An example TDC spectrum of the HPGe detector at 90° is shown in Figure 4.2(a).

The TDC measurements were started in common by the global trigger and the discriminated timing signal from each HPGe detector was used to stop an individual TDC measurement. If the timing filtered signal of an individual detector was below the hardware threshold of the discriminator, the TDC measurement was not stopped and no actual time period was acquired causing an invalid measurement for this channel in the data event. A TDC gate on the E_γ spectra was applied, including the full time range of the TDC module ($t > 0$ and $t <$ "maximum TDC range"). No cut with a range smaller than the full TDC range is possible, because the time distribution for identified ^{4}He particles and for identified ^{4}He in coincidence with a 1249 keV γ-ray do not differ significantly as shown in Figure 4.2 (b) and (c), respectively. Therefore, any shorter TDC cut would reject events of interest. The offline sorted E_γ spectra were filled only if a valid TDC time within the gate was found.

A calibrated E_γ spectrum from a single, $\sim$ 1 hour run using the above TDC gate criteria is shown in black in Figure 4.3, while the raw E_γ spectrum is shown in red. Use

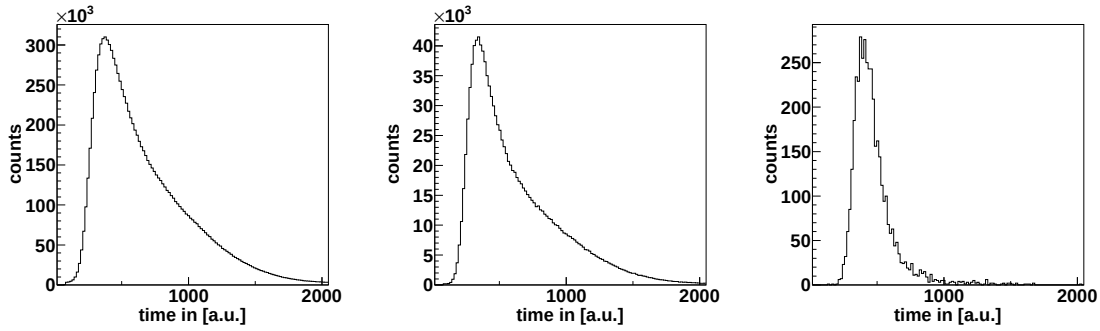

Figure 4.2: The TDC spectra of the HPGe detector at 90° with different applied gates. The histograms contain all data with ^{3}He implanted gold targets. Independent on the gate on identified α particles (b) or on α particles in coincidence with the detection of a γ-ray in the $E_\gamma = 1248.9$ keV peak (c), the distribution of TDC values is similar as for the non gated spectrum (a).

of the TDC gate reduces the background events by an order of magnitude integrated across the entire spectrum. In particular, events have been removed from the individual E_γ spectra, where the energy was below the hardware threshold ($E_\gamma \lessapprox 180$ keV) of the discriminator of the timing signals. Events with $E_\gamma = 0$ keV have been triggered by charged particles, but no γ-ray has been detected in coincidence in the selected HPGe detector (see Figure 4.3 first bin of the red histogram). These events have been rejected by applying the TDC gate as well.

Only events that obey the described TDC cuts are used for the further analysis.

4.2.2 Particle Identification Using the Silicon Telescopes

Charged particle identification (PID) utilizing the Si telescopes is a powerful procedure to identify events of interest and to reduce the background in the E_γ spectra significantly. The identification of ^{4}He particles in the Si-telescopes is used to extract events arising from ^{32}S(^{3}He,^{4} He)^{31}S*. Such transfer reaction events can, in principle, be selected based on the kinetic energy and polar angle of the ^{4}He as measured by the Si-telescope, and the fact that the transfer reaction is a two-body process. All events that have been triggered by charged particles other than ^{4}He must have been created by other reactions such as fusion evaporation or elastic scattering reactions; these must be rejected in the analysis. The following section describes the generation of the $E_{rest}/\Delta E$ histograms and the construction of the particle identification cuts, which have been used to gate the E_γ spectra.

Due to the different energy losses dE/dx of charged particles with different masses and atomic numbers in matter, the combination of a thin Si detector, penetrated by the light charged particle, and a second thick Si detector which stops the same particle allows the identification of the particle by the ratio of energy deposition $E_{rest}/\Delta E$

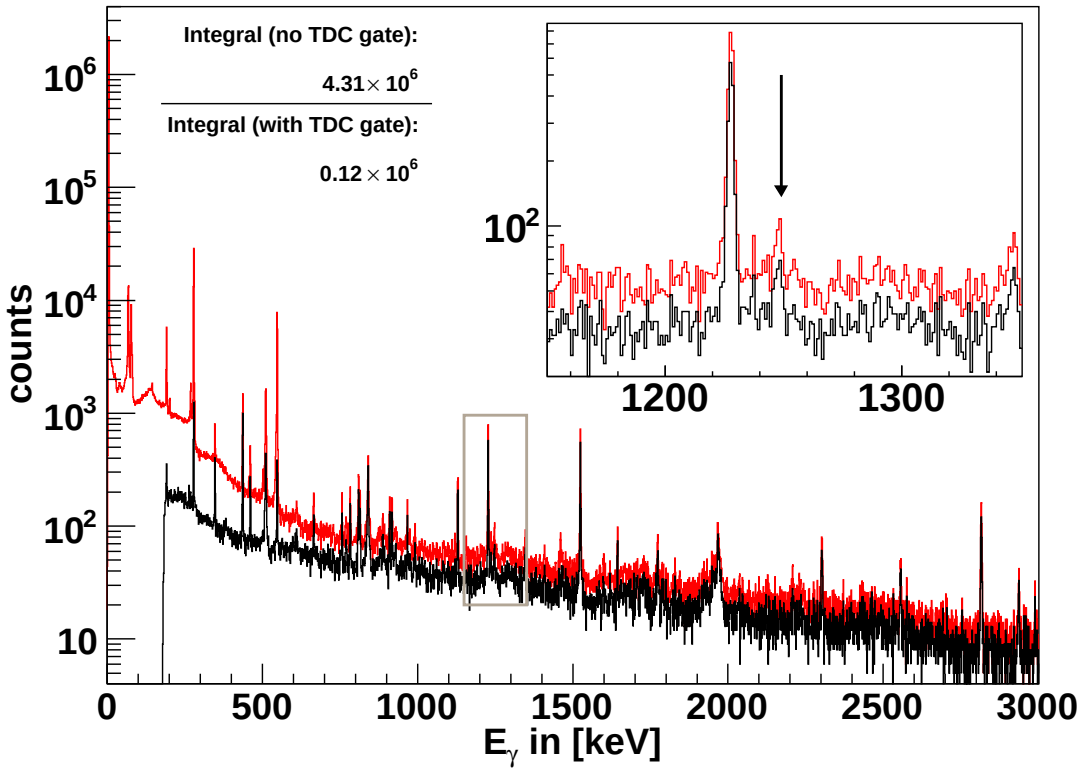

Figure 4.3: Calibrated E_γ spectra of the HPGe detector at 90° with (black) and without (red) the applied TDC gate. The histograms contain data of approximately one hour of beam time with a ^{3}He implanted gold target. The scaling in the y axis is adjusted to the number of counts in the $E_\gamma = 0$ keV peak. The energy cut in the gated spectrum (black) for $E_\gamma \lesssim 180$ keV is caused by the hardware threshold of the discriminator module. The range in the grey rectangle covers the energy range of interest and is zoomed in the upper right. The arrow indicates the energy of the ^{31}S γ-ray transition of interest.

[Kno99].

The raw $E_{rest}/\Delta E$ histogram of one of the Si telescopes in the experiment is shown in Figure 4.4. A clear distinction between the group of protons and helium particles is possible. In the helium group, ^{3}He and ^{4}He particles overlap and can not be initially separated. Nevertheless, their separation is crucial to reject events triggered by elastically scattered ^{3}He particles; such elastic events produce random coincidences that would contribute to the background in the final E_γ spectra.

Due to the global trigger, about half of the events have been triggered by the Si telescope 1 and telescope 2, respectively. This can be used to determine the offsets in the ΔE and E_{rest} axis. If the first Si telescope has triggered the global event, the second telescope will be read and, without a charged particle detection in it, its ADC offset value will be determined. The offsets have been corrected for further analysis and a cut that excludes the nicely separated group of protons and events with no

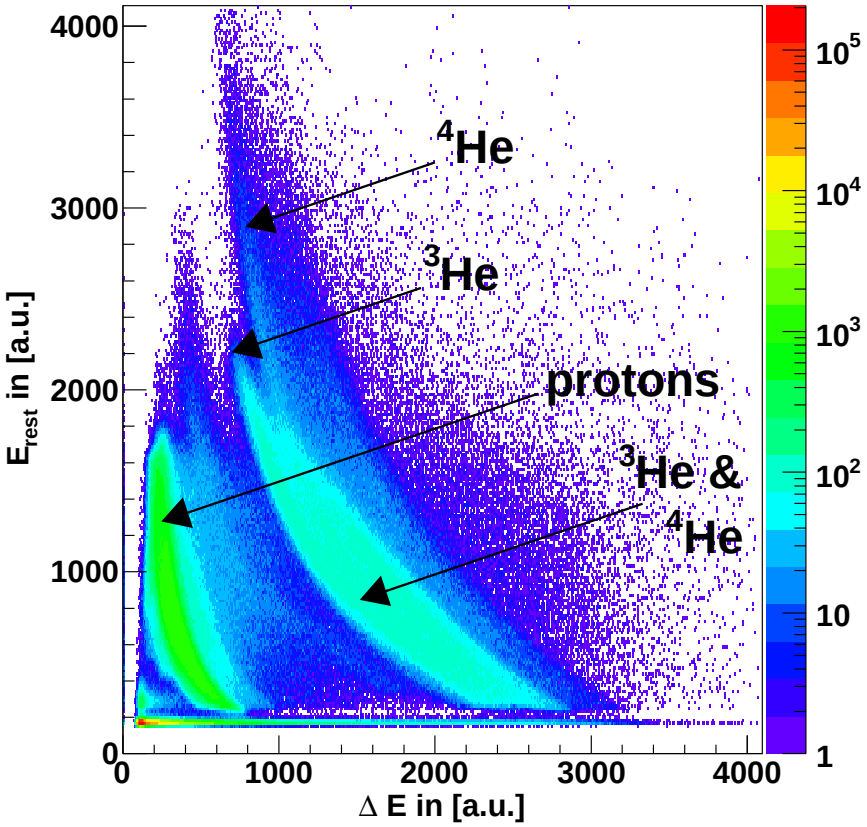

Figure 4.4: E_{rest} vs. ΔE PID plot of $\sim$ 1 hour of beam time of the whole active area of one of the Si telescopes. The arrows indicate different kind of particles.

energy deposition in the E_{rest} detector has been set, because particles, stopped in the ΔE detector can not be identified and their trajectories can not be determined. In the following it is demonstrated how the overlapping ^{3}He and ^{4}He groups have been separated successfully allowing us to generate cleaned E_γ spectra gated only on ^{4}He particles.

The main reason for the lack of separation in the $E_{rest}/\Delta E$ spectra is caused by the limited energy resolution due to the hit position dependent effective thickness of the ΔE detectors because of the geometry of the setup. Depending on the angle between the normalized velocity vector $\overrightarrow{v}$ of the charged particle and the normal vector $\overrightarrow{n}$ of the detector surface, the effective thickness changes as shown in Figure 4.5(a), where δ is the angle that spans between the vectors $\overrightarrow{v}$ and $\overrightarrow{n}$. The effective thickness traversed by the helium particle is given by the inverse scalar product of the two vectors and the normal thickness d_{norm} of the ΔE detector:

$$d_{eff} = \frac{1}{\overrightarrow{v} \cdot \overrightarrow{n}} \, d_{norm} = \frac{1}{\cos(\delta)} \, d_{norm} \tag{4.1}$$

Since the orientation of the ΔE detector did not change during the experiment, δ only depends on the normalized velocity vector $\overrightarrow{v}$ of the detected particle, which can be described by the polar scattering angle θ and the azimuth angle ϕ: $\overrightarrow{v}(\theta, \phi)$ and therefore $d_{eff}(\theta, \phi)$.

Referring back to Figure 3.2 for the definition of our coordinate system, the polar angle θ in the lab frame is defined between the vector of the beam direction $-\hat{z}$ and the velocity vector $\overrightarrow{v}$ of the scattered particle. The angle between the projection of $\overrightarrow{v}$ onto the x/y plane and the x-axis $\hat{x}$ defines the azimuth angle ϕ. The origin of this coordinate system is given by the center of the target.

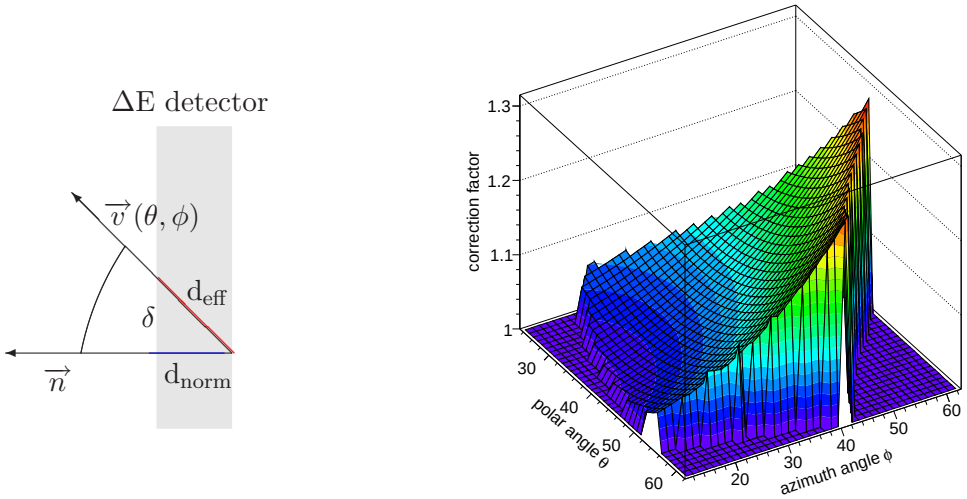

(a) (b)

Figure 4.5: The effective thickness of the ΔE detector. (a) shows the profile of the ΔE detector. A particle with the normalized velocity vector $\vec{v}(\theta,\phi)$ penetrates the detector under an angle of δ relative to the normal $\vec{n}$ vector of the detector's surface. The normal (d_{norm}) and the effective thicknesses (d_{eff}) are marked blue and red, respectively. (b) shows the correction factor for the effective thickness as a function of θ and ϕ. The detector position is at $\theta = 39°$ in the horizontal plane and therefore, the minimum effective thickness is found here. Because the position of the detector, the minimum angle between a particles trajectory and the normal vector of the detector surface δ is $\sim 15°$ and therefore the effective thickness is always larger than the physical thickness.

With the assumption of a pin point target, the velocity vector $\overrightarrow{v}$ is defined by the hit position in the MSPSD E_{rest} detector (see chapter 3.3.2). Taking into account the detector positions relative to the target (see chapter 3.2), the polar and azimuth angle of the trajectory $\overrightarrow{v}(\theta, \phi)$ can be determined. Figure 4.5(b) shows the dependence of the effective thickness d_{eff} on the polar and azimuth angles (θ, ϕ) of the particle direction vector.

The hit pattern of He-type particles in the (θ, ϕ) coordinate system of the MSPSD detectors is shown in Figure 4.6. The originally quadratic shape of the active area of

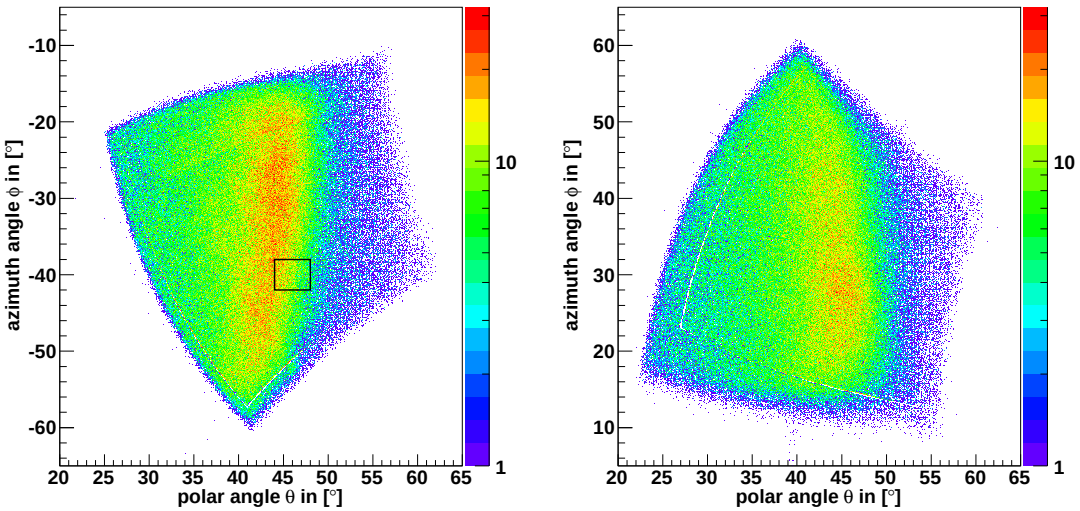

(a) Si telescope 1 (θ, ϕ)

(b) Si telescope 2 (θ, ϕ)

Figure 4.6: The hit pattern of the two Si telescopes in the (θ, ϕ) coordinate system. Due to the rotation of the Si telescopes in the horizontal plane of the HPGe detectors by 39 ° and the vertical offset of their centers by 15 mm with respect to the beam axis the covered azimuth angle ϕ is highly dependent on the polar angle θ.

the detectors transforms to an distorted quadrangle in (θ, ϕ) coordinates.

In order to separate ^{3}He and ^{4}He in the $E_{rest}/\Delta E$ histograms, the detectors have been virtually subdivided, in software, into small pixels ($\Delta\theta = 4.0°$ and $\Delta\phi = 4.0°$). Because of these small angular bins, the thickness variation of the ΔE detector within such a pixel is small. The $E_{rest}/\Delta E$ histogram of a single virtual pixel (indicated in Figure 4.6(a) by a rectangle) is shown in Figure 4.7(a), where it can be clearly seen that separation of ^{3}He and ^{4}He particles is possible.

An algorithm has been developed to find the $E_{rest}/\Delta E$ profile of the ^{4}He particles for each pixel and fit it with a parametrized exponential function indicated by the solid line in Figure 4.7(a). The mass projection of the data onto the fitted function in Figure 4.7(b) has been determined by calculating the shortest distance of an entry in Figure 4.7(a) to the fitted curve. The histogrammed mass projections separate the groups of ^{3}He and ^{4}He particles into two mass peaks in the 1-dim. spectrum of Figure 4.7(b). A one-dimensional cut in the 1-dim. mass spectrum, indicated with the red vertical lines in Fig. 4.7(b), allows for clean separation of ^{4}He from ^{3}He particles in each virtual pixel of the Si-telescope. The 1-dim. cut and the corresponding fit function parameters for each virtual pixel, identifying the ^{4}He particles have been saved to a parameter file, which was loaded by the analysis program.

The cut on identified ^{4}He particles reduces the background in the E_γ spectra significantly as shown in Figure 4.8 and compared to the spectrum in Figure 4.3. The remaining background is mainly caused by fusion evaporation of ^{4}He particles from the reaction $^{32}S + ^{12}C$, but also random coincidences as it will be discussed in section 4.2.4.

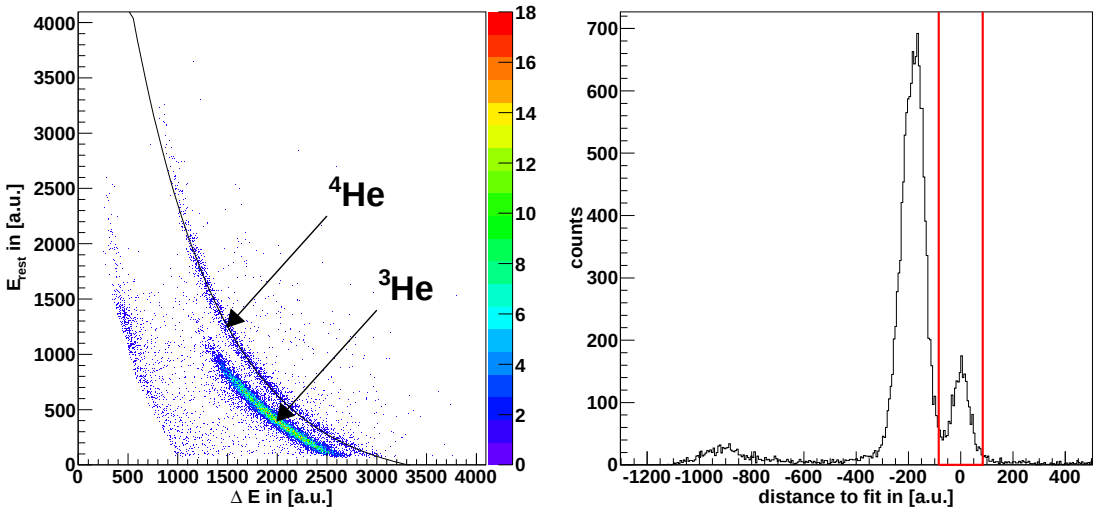

(a) $E_{rest}/\Delta E$ plot for events in the telescope1 obeying the position pixel cut. The ^{4}He profile has been fitted with an exponential function.

(b) Mass weight projection of the data in (a) with respect to the fit. Events included in the red box are identified ^{4}He particles.

Figure 4.7: $E_{rest}/\Delta E$ and mass weight projection of the data from the pixel with its center at $(\theta, \phi) = (46°, \phi = -40)$ with $\Delta\theta = 4°, \Delta\phi = 4°$ as indicated in Figure 4.6(a).

4.2.3 The Reconstruction of the Kinematics

As previously discussed in section 2.4, the energy and the angle of a detected ^{4}He ejectile from the transfer reaction determine the directly populated state in ^{31}S. Therefore, the ^{4}He energy must be reconstructed directly after the reaction in the ^{3}He layer below the surface of the Au gold target.

Due to the energy loss dependence on the effective thickness effect in the target foil, the Mylar foil, and the ΔE detector, the deposited energy in the Si telescope has a θ and ϕ dependence. For all particles entering the Si detector telescope, the energy, identity and hit position (θ, ϕ) are known, therby allowing calculation of energy losses in all previously penetrated layers. Therefore, the total energy E_{total} directly after the reaction can be determined. E_{total} then can be compared with the theoretical kinematics curve with the attempt to identify the populated states to which they would be associated.

The energy calibration of the MSPSD detectors in the experiment was done with a triple α source (^{239}Pu,^{241}Am,^{244}Cm) after the experiment, keeping the experimental conditions the same as during the experiment. The data for the position and energy correction was taken before the experiment (for details see chapter 3.3.2).

During the beam time, the ΔE detectors suffered radiation damage causing their performance to change with time. Their leakage currents were increasing and therefore the voltage drop over the depletion layer decreased, implying that more charge carriers recombined in the detector and could not contribute to the charge measurement. Since

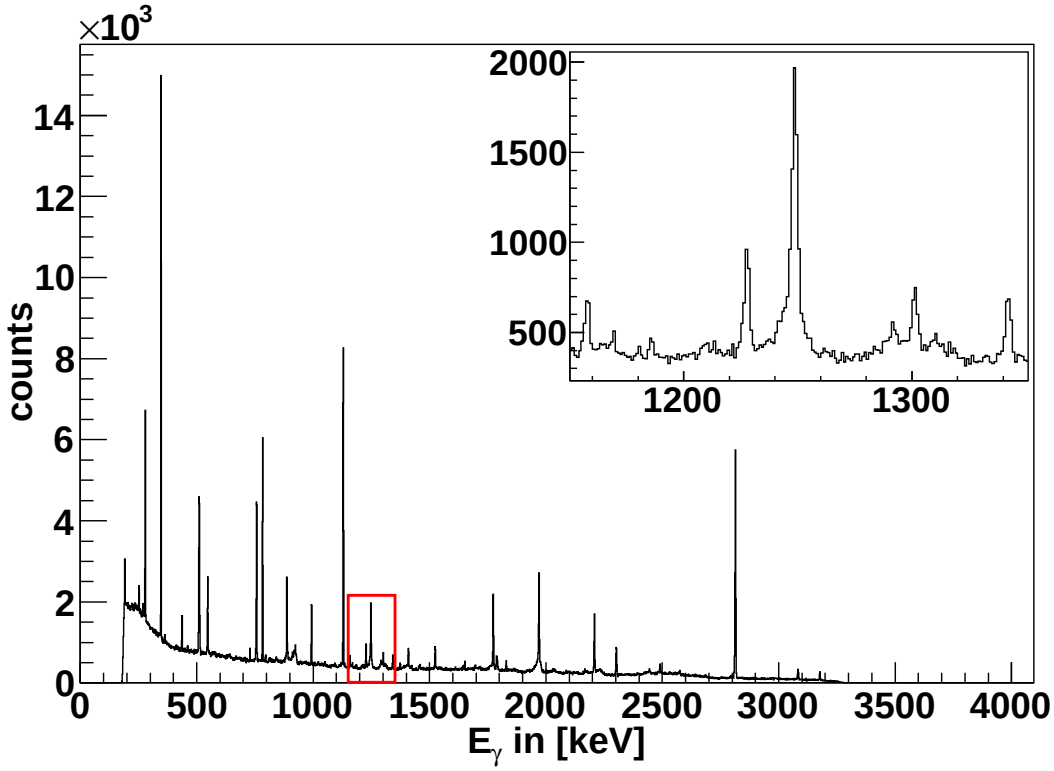

Figure 4.8: Background reduced, energy calibrated E_γ spectrum of the HPGe detector at 90° with a gate on identified ^{4}He particles from 90 hours of beam data. The $3/2+ \rightarrow 1/2+$ transition γ radiation in ^{31}S is observed at 1248.9 keV. The residual peaks besides the ^{31}S line are mostly beam induced and come from fusion evaporation of ^{32}S with ^{12}C or coulomb excitation of ^{197}Au.

the damage grew with time, a time dependent energy shift was observed in the data of the ΔE spectra. In order to compensate for this effect during the experiment, the applied bias voltage was increased and the resistances in the preamplifiers were decreased. Thus, it was necessary to separately determine a set of energy calibration parameters for each run (with a typical run time of one hour). The energy deposition in the ΔE detectors of identified ^{3}He particles can be calculated from the effective thickness of the detector and dE/dx tables, which have been compiled with SRIM [Zie08], and the measured E_{rest} energy. The calculated energy deposition ΔE_{SRIM} vs. the measured ADC value $\Delta E_{meas.}$ is plotted in Figure 4.9(a) for a run early and (b) in the middle of the experiment. Linearity is present in all runs, but the slope and the offset of the linear calibration function changes during the experiment. Events that lie off the line of the linear fits originate from protons or deuterons which have not been rejected by the initial cut on helium isotopes; these events are not considered in the fitting algorithm of the calibration function.

The resulting calibration parameters for the ΔE detector in telescope 1 are plotted

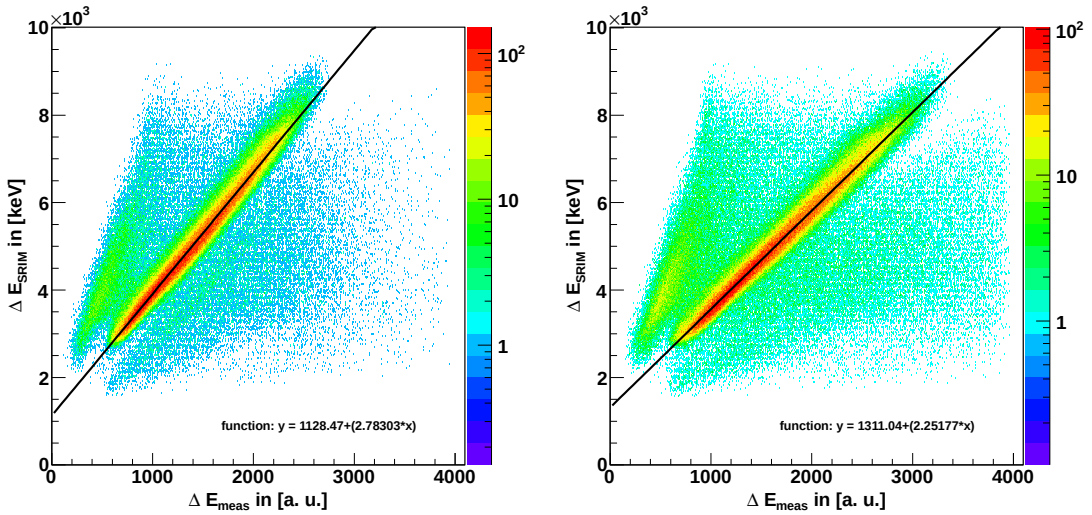

(a) ΔE detector1: data of run 74 (b) ΔE detector1: data of run 104

Figure 4.9: The deposited energies (calculated with SRIM) of identified ^{3}He particles in the ΔE detector versus the measured energy in arbitrary ADC units. The linear correlation is given in all runs. The calibration function parameters change with time due to irradiation damage. This can be observed in the different offsets and slopes in figure (a) and (b).

in Figure 4.10 and show their dependence on the time.

The energy losses in the 6 μm Mylar foil that covers the ΔE detectors and those in the target foil were calculated with SRIM as well. Again, the effective thicknesses of those layers, which depend on the direction vector of the particle, were considered for the calculated energy losses.

The total energy E_{total} of the ^{3}He or ^{4}He particles directly after the reaction is then given by the sum of the measured energy in the E_{rest} detector $E_{rest}^{measured}$ and the

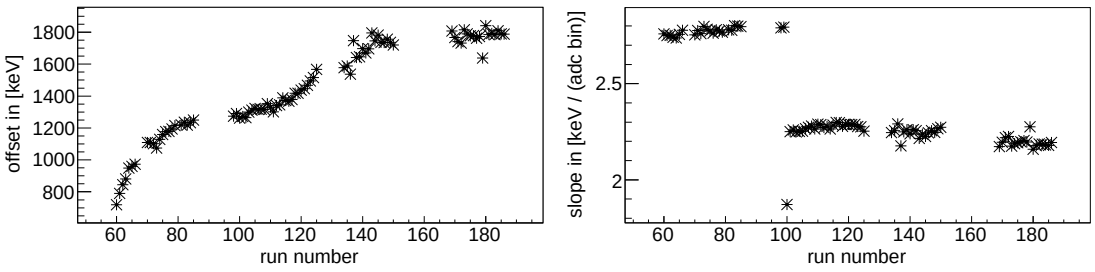

(a) (b)

Figure 4.10: Trend in the time dependence of the offset (a) and the slope (b) in the ΔE energy calibration function from telescope 1 determined from ^{3}He data. The errors are too small to be displayed. The amplifier's gain was adjusted after run 99 and 100.

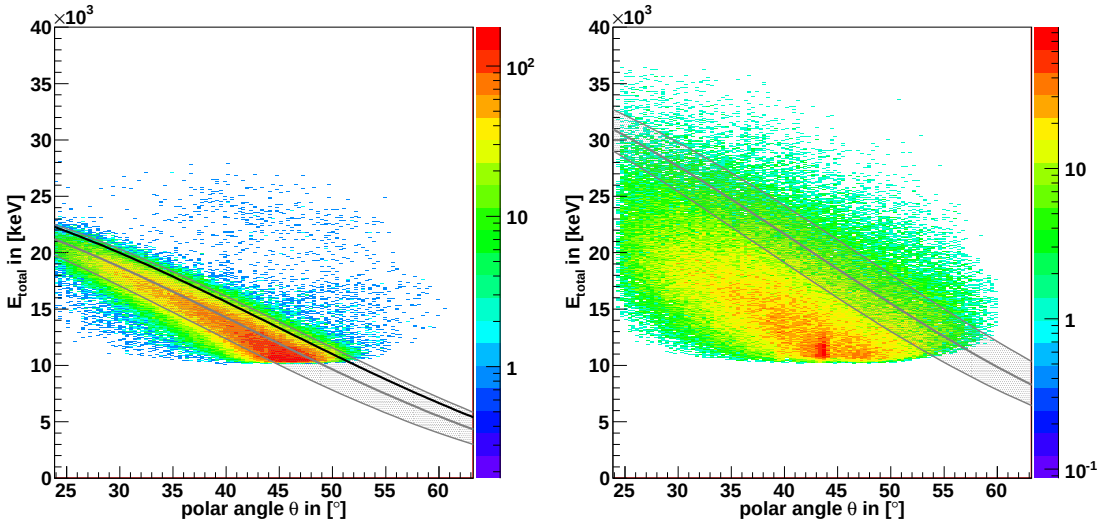

Figure 4.11: The total kinetic energy directly after the reaction of ^{3}He (a) and ^{4}He particles (b) versus their polar scattering angle is shown. Roughly one hour of beam time is shown. The black solid line in (a) indicates the expected energy of elastically scattered ^{3}He particles. The grey line is the black line shifted by $\theta = -3°$ and the grey hatched region indicates the angular uncertainty caused by the beam diameter. The line in (b) indicates the expected energy of the ^{4}He ejectiles from the transfer reaction ^{32}S(^{3}He,^{4} He)^{31}S* assuming the direct population of the first excited state. A shift in θ of $-3\circ$ is included. The grey hatched region indicates the angular uncertainty caused by the beam diameter. See text for details.

calculated energy depositions in the ΔE detector ΔE_{Si}^{SRIM}, the Mylar foil ΔE_{Mylar}^{SRIM} and the gold target ΔE_{target}^{SRIM}:

$$E_{total} = \Delta E_{target}^{SRIM} + \Delta E_{Mylar}^{SRIM} + \Delta E_{Si}^{SRIM} + E_{rest}^{measured} \tag{4.2}$$

The total energy E_{total} as defined in Eq. 4.2 of identified ^{3}He particles versus their polar scattering angle θ is shown in Figure 4.11(a). The thick black line indicates the theoretical angular dependence of their kinetic energy.

The systematic discrepancy between theory and experiment in Figure 4.11(a) can be explained by uncertainties in the position of the Si telescopes and the beam spot position on the target, which cause a systematic error in the determined polar angle θ. For example, a ± 1 mm offset in the horizontal position of the beam spot on the target causes a shift in the determined polar angle of $\pm 2.8°$. Uncertainties in the Si telescope positions and the distance to the target could cause an additional error in the determined polar angle of $\pm 1.6°$ and $\pm 0.6°$, respectively. All these effects cause the systematic shift in the polar angle θ of $\sim 3°$ between theory and experiment. In contrast, the error in the total energy E_{total} is rather small. Here, uncertainties are caused by the energy loss of the ^{32}S beam in the implantation layer of the target before the reaction (maximum 0.5 MeV in the observed energy of ^{3}He particles) and

in the determination of the total energy E_{total} (E_{rest} calibration, uncertainties in the thicknesses of the ΔE detector, the Mylar and the Au target, causing a systematic error in the order of hundreds of keV). Nevertheless, the trend of the angular dependence follows nicely the theoretical predictions.

For the ^{3}He elastic scattering data, the thick grey line in 4.11(a) is shifted by $\theta = -3°$ relative to the thick black line. In the following, all plotted grey lines include the $-3°$ shift in θ relative the theoretical prediction, while the black lines are not shifted. Including this shift, the majority of the experimental data is well described, even though the experimental data is broader than the grey band, which will be discussed in the following. The data of the elastically scattered ^{3}He particles in Figure 4.11(a) shows the angular and energy resolution of the setup. Ideally, one would observe a narrow energy and angular spread in the histogram. Due to the size of the beam spot during the experiment and the close distance of the Si telescopes, the angular uncertainty can be as large as 8.5° with its maximum at $\theta = 54°$ (see appendix A.5). The grey shade in Figure 4.11(a) indicate this angular spread in the determined polar angle. In addition, the angular straggling increases by a factor two from 1.2° (sigma) at 20 MeV to 2.7° (sigma) at 10 MeV (calculated with LISE++ [Tar08]). This explains why the angular spread for the ^{3}He particles is smaller for higher energies. The energy cut off for $E_{total} < 10$ MeV in Figure 4.11(a) is caused by the thicknesses of the ΔE detector, the Mylar foil and the gold target. ^{3}He particles with lower energies are stopped before the MSPSD detector and therefore can not be identified, nor can their hit position (θ, ϕ) be reconstructed. Finally, the density of counts is seen to increase with increasing scattering angle, which is consistent with Rutherford elastic scattering in inverse kinematics and the squarish geometry of the detectors. The detectors covered azimuth angle ϕ and therefore the covered solid angle is θ dependent, peaking at $\theta \approx 41°$ (see Figure 4.6).

The total energies of identified ^{4}He particles versus their polar scattering angle $E_{total}(\theta)$ are plotted in Figure 4.11(b). The theoretical prediction of the kinematics of the ^{4}He ejectiles from the transfer reaction where the first excited state was populated is plotted in grey. Because the described systematical effects for the ^{3}He particles are valid for the ^{4}He ejectiles as well, the $-3°$ shift in θ is already included in the grey line. The grey band indicates the angular uncertainty caused by the beam spread.

The data in Figure 4.11(b) does not show a structure within the grey band and, instead, the majority of the detected ^{4}He particles actually has a lower total energy. Applying a gate on the ^{4}He particles within the grey band does not improve the 1249 keV peak to background ratio in the E_γ spectra which is roughly 1:1. Figure 4.12 shows $E_{total}(\theta)$ of identified ^{4}He ejectiles in one telescope from the whole experiment in coincidence with a γ-ray with an energy of 1249 keV in one of the HPGe detectors. Again, the grey line indicates the expected dependence of ^{4}He ejectiles, coming from the transfer reaction, where the first excited state was populated. The $-3°$ shift in the polar angle θ is included and the uncertainty due to the beam spread is shaded in grey. In contrast to the expected 50% (deduced from the 1:1 peak to background ratio in the E_γ spectra), only 16% of the events in Figure 4.12 lie within the grey band. Several cuts following the shape of the kinematics, covering also lower energies were tried, but the peak to background ratio in the ^{4}He gated E_γ spectra did not change. This shows

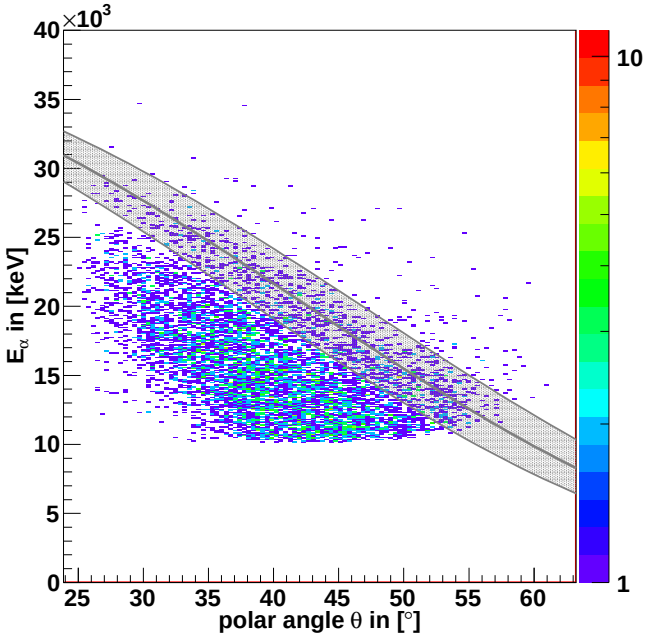

Figure 4.12: The kinetic energy of identified ^{4}He particles from the entire experiment that are in coincidence with a 1248.9 keV γ-ray. The grey band indicates the kinematics of ^{4}He ejectiles from the transfer reaction, populating the first excited state.

that ^{4}He events outside the grey band also contribute to the 1249 keV peak and feeding can not be excluded by the application of cuts in the $E_{total}(\theta)$ spectra. Nevertheless, feeding will be refuted by the observation of $\gamma\gamma$ coincidences as shown in section 4.2.5.

As it will be discussed in section 4.2.4, most of all identified ^{4}He particles in Figure 4.11(b) are caused by fusion evaporation and from physics not related to the transfer reaction. A conclusion concerning the reconstruction of the kinematics will be given in section 4.2.6 after the origin of the fusion evaporated ^{4}He particles is discussed in the next section and feeding will be excluded in section 4.2.5.

4.2.4 Background Events

All data events triggered by charged particles from other reactions than the transfer reaction have been considered as background events. These can originate from elastically scattered particles from the target (mainly ^{3}He), or evaporated products from fusion reactions (mainly protons and ^{4}He particles). The particle identification allows to reject events that were triggered by other particles than ^{4}He, excluding basically all elastically scattered particles.

Fusion evaporation reactions become possible if the beam energy is high enough to open fusion reaction channels with the target material. Then fusion evaporation can cause a significant ^{4}He and coincident γ-ray background. Due to their high atomic numbers, fusion of ^{32}S and the gold nuclei in the target is not possible, but fusion of

^{32}S with impurities such as carbon on the surface of the target is possible and was observed. The contamination of the target surface could occur during the production or the storage of the targets. The theoretical cross sections of fusion reactions of ^{32}S with ^{12}C was estimated with PACE4 [Tar03] to be as high as 761 mbarn at a beam energy of E_{beam} = 85 MeV. The cross sections of the transfer reaction of interest is three orders of magnitude lower.

Events in the experiment that were triggered by evaporated products such as protons or deuterons from fusion reactions can be rejected in the offline analysis with the particle identification, but if ^{4}He particles are evaporated this is not possible. The products of those fusion reactions were identified on the basis of γ-ray spectroscopy in the ^{4}He gated E_γ spectra, which is shown in Figure 4.13.

The largest cross sections have been calculated with PACE4 for the production of ^{39}K (444 mbarn), ^{42}Ca (126 mbarn), ^{42}Sc (87 mbarn), ^{40}Ca (54 mbarn) and ^{36}Ar (24 mbarn)[Tar03]. In case of ^{39}K and ^{36}Ar reaction channels, at least one ^{4}He particle is emitted, thus leading to the background γ-ray lines in the ^{4}He gated E_γ spectra as shown in Figure 4.13. The observed γ-ray transitions marked in red and green match the extracted level schemes of ^{39}K and ^{36}Ar in Figure 4.14. This demonstrates that fusion evaporation is the major background source for ^{4}He particles and coincident γ-rays.

The theoretically calculated energy spectra of the evaporated ^{4}He particles from fusion evaporation (^{32}S+^{12}C) as a function of the polar angle in the lab frame is shown in the Figure 4.15 (calculated with PACE4 [Tar03]). The thick black line indicates the energy of ^{4}He ejectiles from the transfer reaction of interest. The neighboring thin lines indicate its angular spread due to the beam spot size. The angular spread for the evaporated ^{4}He particles is in the same order, but is not included in the data of the histogram. The energies of ^{4}He particles from fusion evaporation and ejectiles from the transfer reaction overlap and therefore no discrimination is possible.

4.2.5 Feeding

DSAM lifetime measurements can be corrupted by feeding, which is the indirect population of the state of interest caused by γ-ray transitions into the state of interest from higher lying states. This would shift the result towards longer lifetimes, because the feeding to the state of interest can occur during the stopping process. Due to the two-body nature of the transfer reaction, elimination of feeding would be possible by analysis of the ^{4}He kinematics curve as described in chapter 2.4. However, as shown in section 4.2.3 this is not possible in the experimental data. Nevertheless, it can be shown that feeding has not been an issue in the commissioning experiment by looking for $\gamma\gamma$ coincidences. If feeding had been significant, γ-rays with the correct transition energies would have been observed in coincidence with a γ-ray in the 1249 keV peak (see ^{31}S level scheme in Figure 2.1). Figure 4.16 shows the accumulated E_γ spectrum of the entire experiment from all HPGe detectors gated on ^{4}He particles and in coincidence with a γ-ray in the 1249 keV peak from the ^{31}S de-excitation of interest.

Comparing the $\gamma\gamma$ coincidences in Figure 4.16 with the possible transitions in the

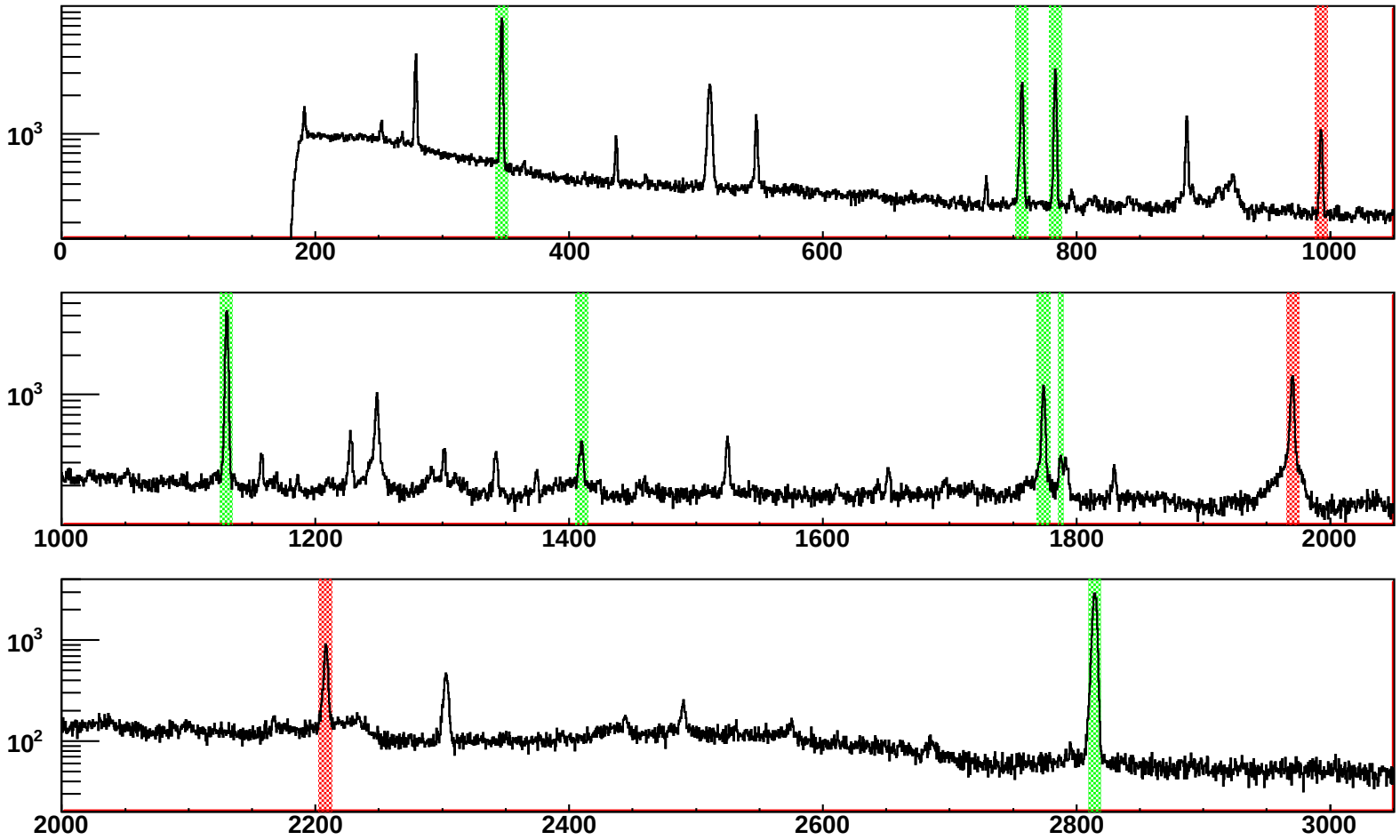

Figure 4.13: The E_γ spectrum in units of keV accumulated from the entire experiment of the detector at $\theta = 90°$ gated on ^{4}He particles shows evidence of fusion evaporation of ^{32}S with ^{12}C resulting in ^{39}K and ^{36}Ar. The energies from ^{39}K de-excitation are shaded in green: 346.7 keV, 756.9 keV, 783.4 keV, 1130.0 keV, 1409.8 keV, 1774.0 keV, 1787.7 keV, 2814.24 keV. The energies from ^{36}Ar de-excitation are shaded in red: 992.8 keV, 1970.4 keV, 2207.9 keV. Additional observed lines have been be assigned to transitions in ^{197}Au, ^{40}Ca, ^{42}Ca and ^{31}S.

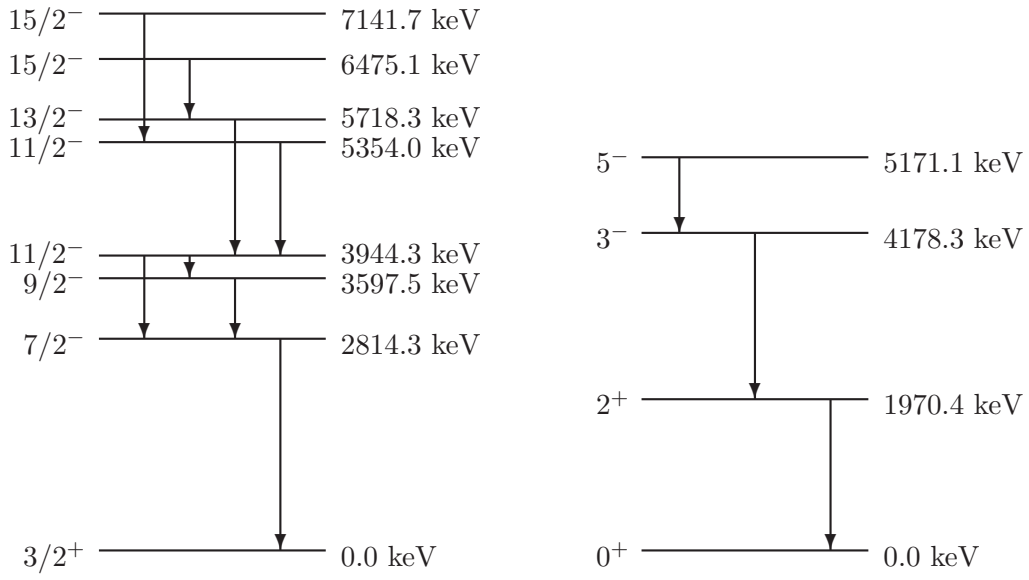

(a) Extracted level scheme ^{39}K (b) Extracted level scheme ^{36}Ar

Figure 4.14: Extracted level schemes: Only states resulting in observed transitions are included. The data is taken from the nudat website [nud11].

level scheme of ^{31}S in Figure 2.1 shows that no transition energies have been observed that hint on feeding. The possible transition energies are indicated with arrows; the widths of the attached horizontal lines indicate their possible Doppler shifts. Only few $\gamma\gamma$ coincidences are observed in the ranges of interest, but they are observed with the ^{3}He implanted targets (red) as well as with Au-only targets (black). Therefore, and because the ^{4}He gated E_γ spectra do not show lines at possible transition energies in ^{31}S as well, it can be concluded that no major feeding was observed that could effect the determined lifetime significantly.

4.2.6 Discussion of the Kinematics

The 1249 keV peak to background ratio in the E_γ spectra, gated on all identified ^{4}He particles is 1:1 as it can be seen in Figure 4.8.

The cross section for the fusion evaporation reactions of the ^{32}S beam with the ^{3}He target nuclei was calculated with PACE4 [Tar03] and shows that only ^{35}Ar could be produced by this reaction. Other fusion evaporation reactions of the beam nuclei with ^{12}C (whose reaction products were observed) or ^{14}N and ^{16}O (whose reaction products were not observed, but could be contaminations from the atmosphere on the target) do not produce ^{31}S as well [Tar03].

Because ^{31}S* can not be produced by fusion evaporation reactions with the proven target nuclei (including identified impurities), half of the ^{4}He particles in the $E_{\text{total}}(\theta)$ spectrum in Figure 4.12 must come from the transfer reaction of interest and the

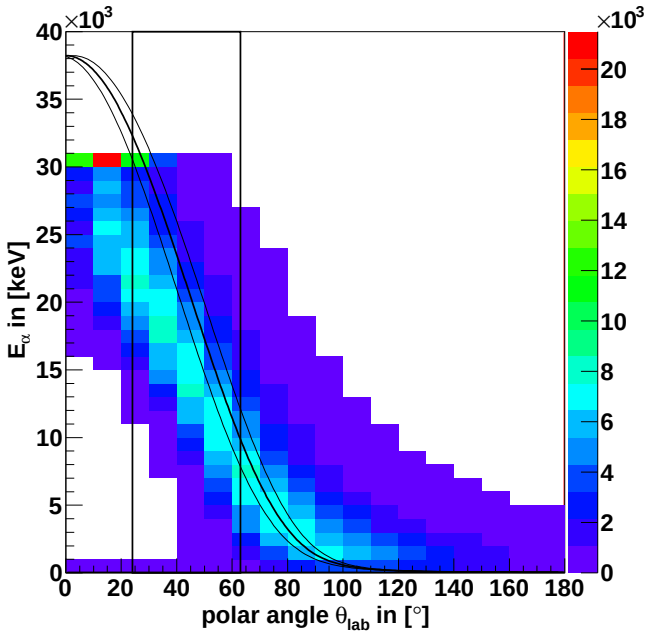

Figure 4.15: The total kinetic energy $E_\alpha(\theta_{\mathrm{lab}})$ of ^{4}He particles from fusion evaporation reactions of ^{32}S with ^{12}C, calculated with PACE4. The black frame indicates the angular coverage of the Si telescopes. The middle black curve indicates the kinematics of ^{4}He ejectiles from the transfer reaction, populating the first excited state. The two outward curves indicate the angular uncertainty caused by the beam diameter on the target.

other half from background reactions such as fusion evaporation reactions, that do not produce ^{31}S.

Only 16% of all events in the histogram in Figure 4.12 lie in the range of the grey shade, which does not match 50% from the 1249 keV peak to background ratio in the ^{4}He gated E_γ spectra. This could hint on feeding from higher states, that were populated by the transfer reaction, but this can be disproved by the observed $\gamma\gamma$ coincidences as shown in the previous section 4.2.5 and the population of higher states was also not observed by McQueen et al. [McQ70] and Engmann et al. [Eng71].

^{4}He particles from fusion evaporation, creating other nuclei such as ^{39}K or ^{36}Ar could by chance trigger the DAQ in coincidence with the 1249 keV γ-ray emission from a ^{31}S nucleus produced by the transfer reaction where its associated ^{4}He ejectile did not hit one of the Si telescopes. Nevertheless, those random coincidences are extremely rare and could only contribute about 1 ‰ to the observed ^{4}He-γ coincidences shown in Figure 4.12.

Taking into account the poor resolution and the wide spread in the energy and angle in the $E_{\mathrm{total}}(\theta)$ data of the elastically scattered ^{3}He particles in Figure 4.11(a), it is likely that 50% of the $^4\mathrm{He} - \gamma$ coincidences in Figure 4.12 actually come from the transfer reaction, but the low statistic combined with the same number of background events (see E_γ peak to background ratio) do not allow to reconstruct their kinematics

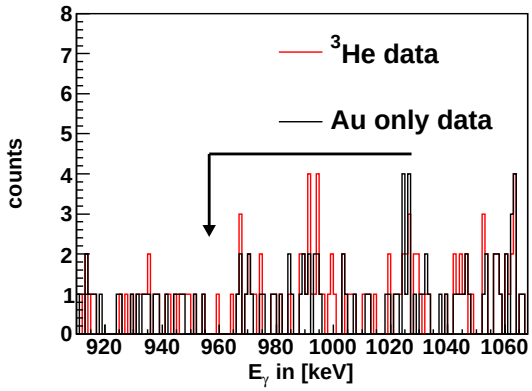

(a) Zoomed energy range for data from ^{3}He implanted targets (red) and gold only targets (black)

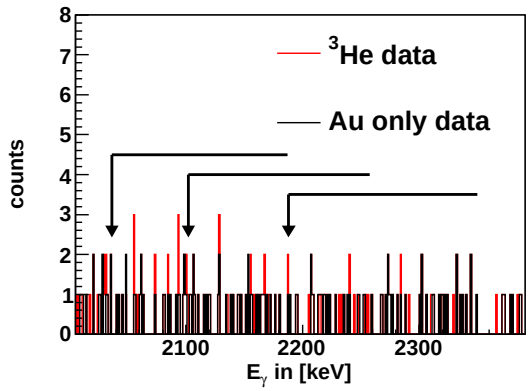

(b) Zoomed energy range for data from ^{3}He implanted targets (red) and gold only targets (black)

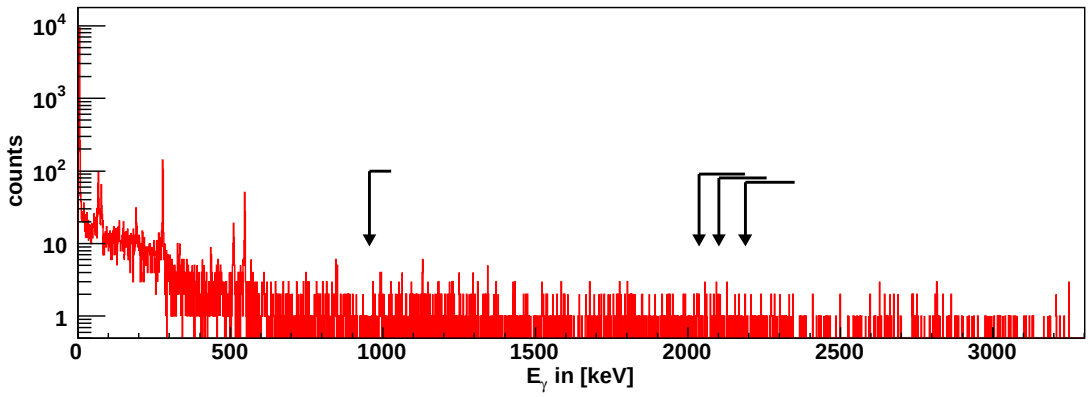

(c) Triggered by α particles and coincident with 1246 keV $< E_\gamma <$ 1251 keV

Figure 4.16: γ-ray coincidences with the detection of a γ-ray in the 1249 keV peak in one of the HPGe detectors. Data of the entire experiment is shown. The black arrows indicate energies, where coincidences can be expected, due to feeding: 986.6 keV, 2036.5 keV, 2102.1 keV and 2188.1 keV (see level scheme in Figure 2.1 for details of the possible transitions). The widths of the horizontal lines which are attached to the arrows indicate the range of the possible Doppler shifts.

or to separate them from underlying background events.

The absence of γ-ray lines that would be necessary to populate the first excited state in ^{31}S indirectly allows the conclusion that feeding can not be a major effect in this experiment and hence the lifetime which will be determined from from the line shapes in the E_γ spectra is not corrupted, even though the cut on the kinematics is not possible. Additionally, the population of states higher than the second state in ^{31}S was also not observed by McQueen et al. [McQ70] and Engmann et al. [Eng71], while the second state does not feed into the first excited state of interest (see the level scheme in Figure 2.1).

4.2.7 E_γ Spectra Background Subtraction

The background in the E_γ spectra has been highly reduced using the identification of ^{4}He particles. Nevertheless, some background peaks remained in the range of the 1249 keV peak and could not be reduced as shown in Figure 4.17, where the processed data of the entire experiment is accumulated from the ^{3}He implanted gold targets (black) and the Au-only targets (red). The Au-only E_γ spectrum nicely reproduces the background in the ^{3}He E_γ spectrum and therefore could be adopted for background subtraction. The following section describes the procedure in detail.

Because only a fraction of all identified ^{4}He particles were produced by the transfer reaction of interest, many of the ^{4}He particles were from fusion evaporation and created background events in the E_γ spectra. The data, which was acquired with Au-only targets, was processed in the same way as the data from ^{3}He implanted targets. Therefore, the Au-only E_γ spectra can be subtracted from the ^{3}He E_γ spectra after their normalization to each other. The statistics of the two data sets is comparable. Due to minor fluctuations, the binning in the spectra has been reduced by a factor of two resulting in a 2 keV binning, which is also in the order of the HPGe detectors energy resolutions.

The result of the γ-ray background subtraction of the E_γ spectra of all three HPGe detectors is shown in Figure 4.18. The line shape of the 1248.9 keV peak is singled out.

The E_γ background in the spectra in Figure 4.17 consists of a continuum structure and some significant peaks (e.g. lines from ^{39}K as shown in section 4.2.5). The ratio of the peak height to the continuous background changes with time due to the reduction of the target impurities that could be sputtered off by the ion beam. Therefore, it is not possible to scale the two sets of data in a way that the peaks and the continuum match simultaneously. The impurities on the target are not fully understood, but the rate of background reactions was highly reduced within the first 30 minutes of a new target position. Because of this effect, it is likely that the impurities sit on the surface of the target. The scaling has been optimized to reproduce the structures in the long tail of the line shape in the E_γ spectrum of the detector at 0° and therefore the background peak at 1340 keV peak was not fully removed in the subtracted spectra (see the arrow in figure 4.17(c) and 4.18(c)). Considering the analysis of the shape of the 1249 keV line, only the E_γ spectrum of the HPGe detector at 0° could be affected by the persistence of the 1340 keV peak. Therefore, the 1340 keV peak has been fitted and removed from

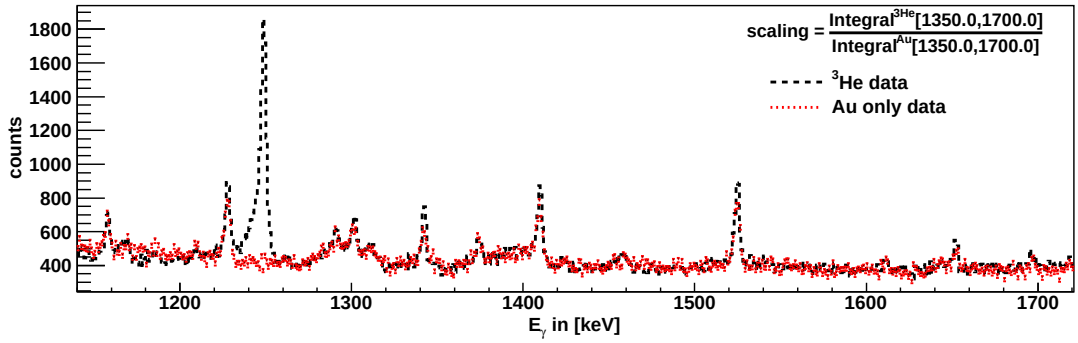

(a) HPGe detector at 110°

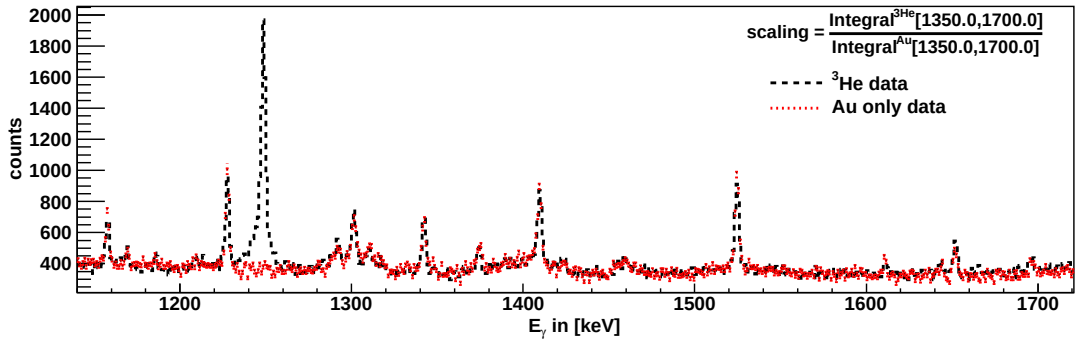

(b) HPGe detector at 90°

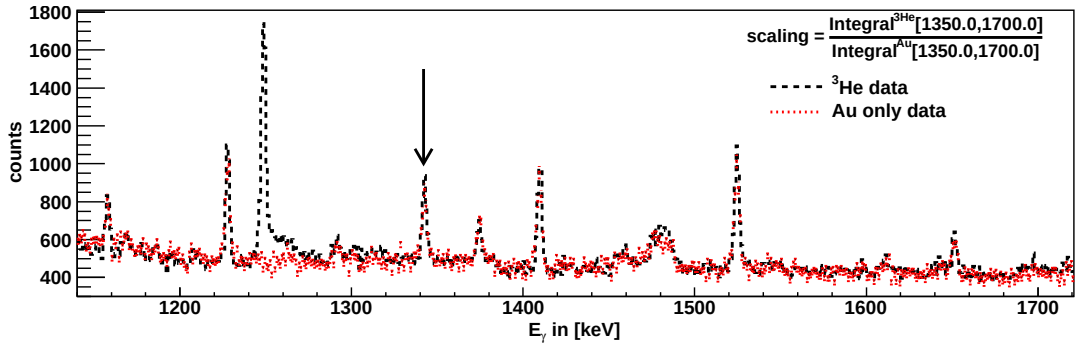

(c) HPGe detector at 0°. The arrow indicates a background peak that is not perfectly reproduced in the Au only data.

Figure 4.17: The background data from the runs with the ^{3}He implanted and Au-only targets has been scaled to each other to allow background subtraction. Data of the entire experiment is shown.

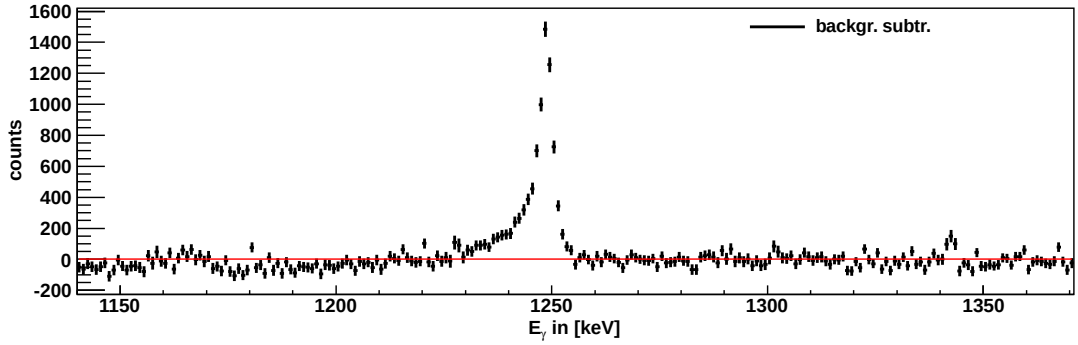

(a) HPGe detector at 110°

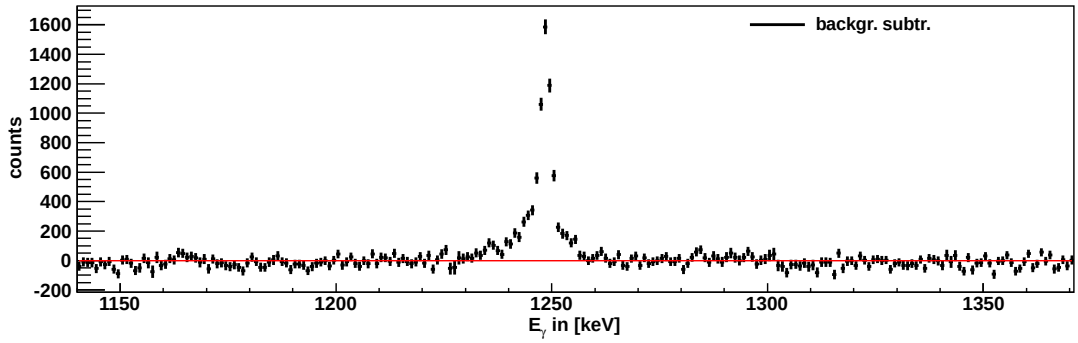

(b) HPGe detector at 90°

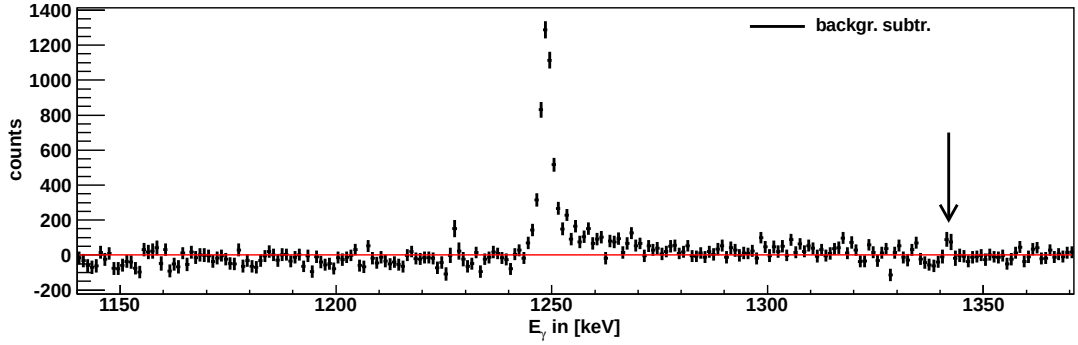

(c) HPGe detector at 0°. The arrow indicates the peak that could not be removed perfectly by background subtraction.

Figure 4.18: E_γ spectra background subtracted with a 1 keV binning from data of the entire experiment.

the data sets before the subtraction. The result is used for further lifetime analysis. Also the background peak at 1225 keV is not fully removed in the subtracted spectra and lies in the range of the line shapes for 110° and 90° (see Figures 4.18(a) and (b)). Because the underlying shape of the 1248 keV line is not known and an elimination with a fit could remove information on the lifetime, the peak will not be removed but excluded in the final fitting for the lifetime determination.

4.2.8 HPGe Efficiency Correction

The energy dependent efficiency change of the HPGe detectors within the energy range of the line shape is small and in the order of 4%. Nevertheless, this means that the detection efficiency of a fully shifted γ-ray ($\beta = 0.07c$) is 4% smaller than for a non shifted γ-ray and therefore, the number of counts in the bins of the line shapes of the HPGe detectors need to be corrected. For this, the entry of each bin has been divided by the efficiency function determined in section 3.3.1 and normalized to the efficiency of the HPGe detector at 110° at an energy of 1248.9 keV. The errors have been adopted. The normalization was done to keep realistic numbers for the detected γ-rays, representing the statistics of the data. The resulting spectra are used for the line shape fit and will be shown in Figure 5.1, 5.2 and 5.3 in chapter 5.

4.3 The Line Shape Analysis

The lifetime determination from the Doppler affected line shapes has been done using the analysis program APCAD (Analysis Program for Continuous Angle DSAM) [Sta11] and the simulation tool Geant4 [Ago03]. Three major steps were necessary to determine the lifetime:

1. The transfer reaction with its differential cross section and the stopping process of ^{31}S within the target have been simulated with Geant4. The velocity trajectories of the excited ^{31}S and the ^{4}He particles are saved for each time step of the simulation.

2. Simulated events of interest are selected, using the position and the geometry of the charged particle detectors with respect to the target. The velocity components of the ions into the directions of the HPGe detectors were determined for each time step of the simulation. These velocity components define the expected, simulated Doppler shifts of potentially emitted γ-rays.

3. The fitting procedure models the line shape in the E_γ spectra by convolving the lifetime and the expected Doppler shifts. The χ^2 of the modeled line shape and the experimental data is optimized by the variation of the free parameters in the model.

In the following, each of these steps is discussed in detail.

4.3.1 Monte Carlo Simulation

The Monte Carlo simulation tool Geant4 [Ago03] was used to simulate the transfer reaction and the energy losses in the target. If a transfer reaction occurs in the simulation, the event is saved to a file.

Considering a single event, the position and the velocities of all particles are calculated after each time step. The simulation accounts for the physical interactions, the geometry and the physical properties of the rotated target and the ion beam. The geometry of the target and the beam in the simulation is shown in Figure 4.19. The differential cross sections (see section 2.3) of the transfer reaction are read from tables and can be enhanced to boost the performance of the simulation. The used inputs of the simulation are listed below:

- Ion beam species and energy: A ^{32}S beam with E_{beam} = 85 MeV has been simulated.

- Ion beam position and direction: The beam is produced in the origin of the simulation's Cartesian coordinate system. The ions are emitted along the -z axis (see Figure 3.2 for the definition of the coordinate system). The beam spot intensity follows a Gaussian distribution in x and y with σ_x = 1.5 mm and σ_y = 2.0 mm, respectively.

- Target position: The beam-facing surface of the target is centered along the beam (z-) axis, and lies in the x/y plane of the right handed coordinate system. Two edges are parallel to the coordinate axis y.
- Target area and thickness: The target is 30×30 mm^2 with a total thickness of 6.2 μm and has two layers. The first layer consists of ^{3}He implanted gold and has a thickness of 0.15 μm. The second layer consists of pure gold with a thickness of 6.05 μm. The target area is larger than in the experimental setup, to avoid contour effects. The aim of the first layer is to provide ^{3}He for the transfer reaction, while the second layer serves as stopping material.
- Target rotation: The target is rotated around the y axis by 54° (see Figure 3.2 for the definition of the coordinate system). After the rotation, the position in z direction is shifted such that the x/y-axis plane is not penetrated by the target. Therefore it is assured that the beam is produced outside the target. This downshift of the target is corrected for in the ion position data written to file.
- Target species and densities: The ^{3}He implanted gold has a density of 19.395 g cm^{-3}. 0.3853% mass fraction is ^{3}He and 99.6147% mass fraction is ^{197}Au. The gold layer has a density of 19.32 g cm^{-3} (see section 2.2.2 for details).
- Transfer reaction: The population of the first excited state ($3/2^+$, 1248.9 keV) in ^{31}S via ^{32}S(^{3}He,^{4} He)^{31}S* is the only allowed nuclear reaction in the simulation. Multiple excitation is excluded explicitly. The energy and polar angle dependent differential cross sections are given in tables, calculated with Fresco [Tho88, Wim11] (see chapter 2.5). The Fresco differential cross section was calculated for different beam energies (see Figure 2.4(b)) and therefore the change in the cross section due to the beam energy loss within the ^{3}He implanted layer in gold was considered.
- Simulation control: In order to reduce the computational run time, an enhancement factor of the cross section of the transfer reaction has been set. 1000000 beam particles have been simulated, resulting in 200000 excited ^{31}S* nuclei. The fluctuation in the determined lifetimes from several sets of simulations with different random seeds with this statistic is smaller than their determined statistical errors. The maximum tracking time per event has been set to 6 ps with a step size of 0.001 ps.

The velocity vectors of the excited ^{31}S $\overrightarrow{\beta}(t_\mathrm{i})$ in units of c and of the ^{4}He particle were saved for each time step t_i of the simulation. The simulation of one million beam particles and the described settings took about 5 hours computer run time and created an output file of 22 Gb. The absolute speeds $|\overrightarrow{\beta}(t_\mathrm{i})|$ of the ^{31}S* as a function of the time after excitation are shown in Figure 4.20. The horizontal lines with $|\overrightarrow{\beta}(t_\mathrm{i})| > 0$ represent ions that are scattered at gold nuclei under large polar angles out of the target.

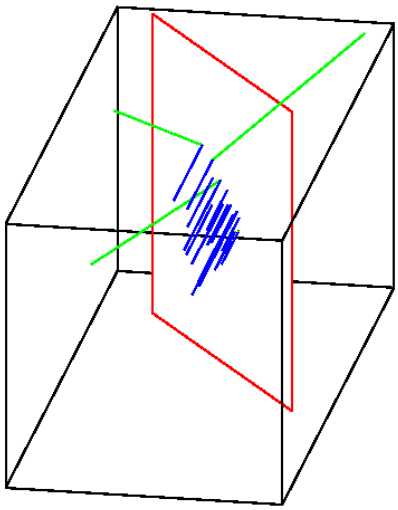

Figure 4.19: The black volume indicates the world volume of the simulation, wherein the particles are tracked. The red box indicates the rotated implanted target. The beam particles (blue) are produced in the x/y plane according to the beam spot intensity, heading to the back. The green lines indicate ^{4}He ejectiles from the simulated transfer reaction. This visualization was created with HepRApp [SLA09].

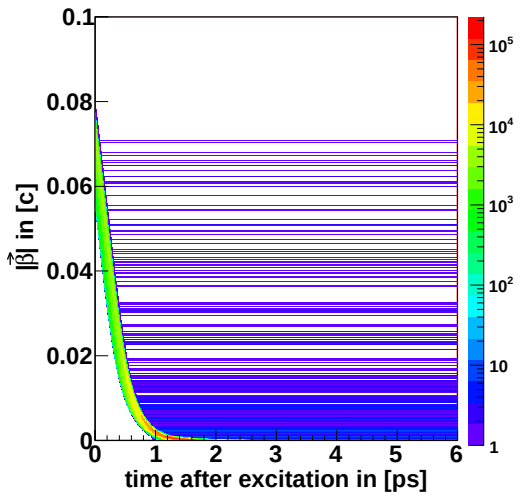

Figure 4.20: Stopping matrix - the absolute velocity of the excited ^{31}S* is plotted in units of c versus the time after excitation. All excited ^{31}S particles in forward direction are stopped within the target. The few horizontal lines describe ions that are scattered at gold nuclei and leave the target at large polar angles.

4.3.2 APCAD: From the Simulation to the Velocity Projections

The velocity component of the ^{31}S* in the direction of the γ-ray detection and the absolute speed $\beta = |\overrightarrow{\beta}|$ determine the observed Doppler shifted energy:

$$\begin{aligned} \mathrm{E}'_\gamma &= \mathrm{E}^0_\gamma \frac{\sqrt{1-\beta^2}}{1-\beta\cos\alpha} \\ &= \mathrm{E}^0_\gamma(1+\mathrm{m}) \end{aligned} \tag{4.3}$$

with the transition γ-ray energy E^0_γ and the angle α between the moving direction of the ion and the γ-ray detection and the Doppler shift factor m, defined by:

$$\begin{aligned} \mathrm{m} &= \frac{\mathrm{E}'_\gamma}{\mathrm{E}^0_\gamma} - 1 \\ &= \frac{\sqrt{1-\beta^2}}{1-\beta\cos\alpha} - 1 \\ &\approx \beta\cos\alpha \\ &= \frac{1}{|\overrightarrow{a}_\mathrm{k}|}\overrightarrow{\beta}(t_i)\cdot\overrightarrow{a}_\mathrm{k} \end{aligned} \tag{4.4}$$

Therefore, the Doppler shift factor m needs to be calculated for each individual detector. This section describes how a distribution of Doppler shift factors for each detector at each time step is calculated.

The simulation (see section 4.3.1) stores the velocity vectors of all excited ^{31}S and the corresponding ^{4}He particles at each time step of the simulation. Since the events in the experiment are triggered from ^{4}He particles in the Si telescopes, simulated events where the ^{4}He does not leave the target in a direction that is covered by the solid angle of the Si detectors are dismissed in the projection of $\overrightarrow{\beta}$ on the γ-ray emission direction.

Hence, the total number of created ^{31}S* in the simulation is reduced from ~ 200000 to ~ 10000. This is crucial, because the geometry of the setup is not symmetric and therefore observed γ-rays in coincidence with detected ^{4}He particles are emitted from ^{31}S nuclei that move along a priority direction, chosen by the covered solid angle of the Si detectors (see section 2.4). The projections of the velocity vectors of the residual ^{31}S*, determining the $\beta \cos\alpha$ term, and the calculation of the Doppler shift factor is demonstrated in the following.

The HPGe detectors cover a finite solid angle and therefore just one projection on the γ-ray emission line $\overrightarrow{a}$ through the center of each detector's surface would not be sufficient to reproduce the line shapes in the E_γ spectra. Instead, the detectors surfaces have been virtually divided into n pixels. The normalized vectors of observation and γ-ray emission $\overrightarrow{a}_{\mathrm{k}}$ are defined by the position of the ^{31}S nucleus and the pixel center on the HPGe detector's surface. The projection of the ion velocity vector $\overrightarrow{v}_{\mathrm{ion}}(t_{\mathrm{i}})$ on the vector of observation $\overrightarrow{a}_{k\epsilon n}$ is obtained as demonstrated in Figure 4.21. The schematic drawing is simplified and only two dimensions are taken into account.

The velocity projection in Figure 4.21 is indicated in red and corresponds to the scalar product $\vec{\beta}(t_i)\vec{a}_k$ in Equation 4.4. The Doppler shift factor $\mathrm{m_{i,k}}$ is determined by this scalar product and the absolute velocity $\beta(t_i)$ and is histogrammed in black below the schematic diagram. The result is a distribution of Doppler shift factors, determining the expected Doppler shift over all pixels. The histogram is scaled by 1/(number of pixels n). Considering the third dimension and the circular shape of the detector's surface, it is clear that there are less pixels for small and large θ angles than for the median θ angles at the center of the detector. Due to the solid angle effect in three dimensions, the distribution transforms to the green histogram.

If the velocity of the moving nucleus is high, relativistic effects become important. Although the beam like particles in the ^{31}S* experiment achieve only velocities of a few percent of the speed of light, the effective solid angles of the detectors change if the γ-ray is emitted in flight. Therefore, the HPGe detector at 0° covers a larger solid angle, if the γ-ray is emitted at high velocities (short time after excitation) than for a γ-ray emission at rest (long time after excitation). This is accounted for in the APCAD software for the covered solid angles of the HPGe detectors by weighting $\mathrm{m_{i,k}}$ with the relativistic change of the solid angle.

The corresponding histogram is filled with the Doppler shift factors $\mathrm{m_{i,k}}$ from all ^{31}S* for each time bin. The analogous histogram from the simulation will be shown in Figure 4.23(a) where the $\mathrm{m_k}$ factors in one time step of all simulated ions have been

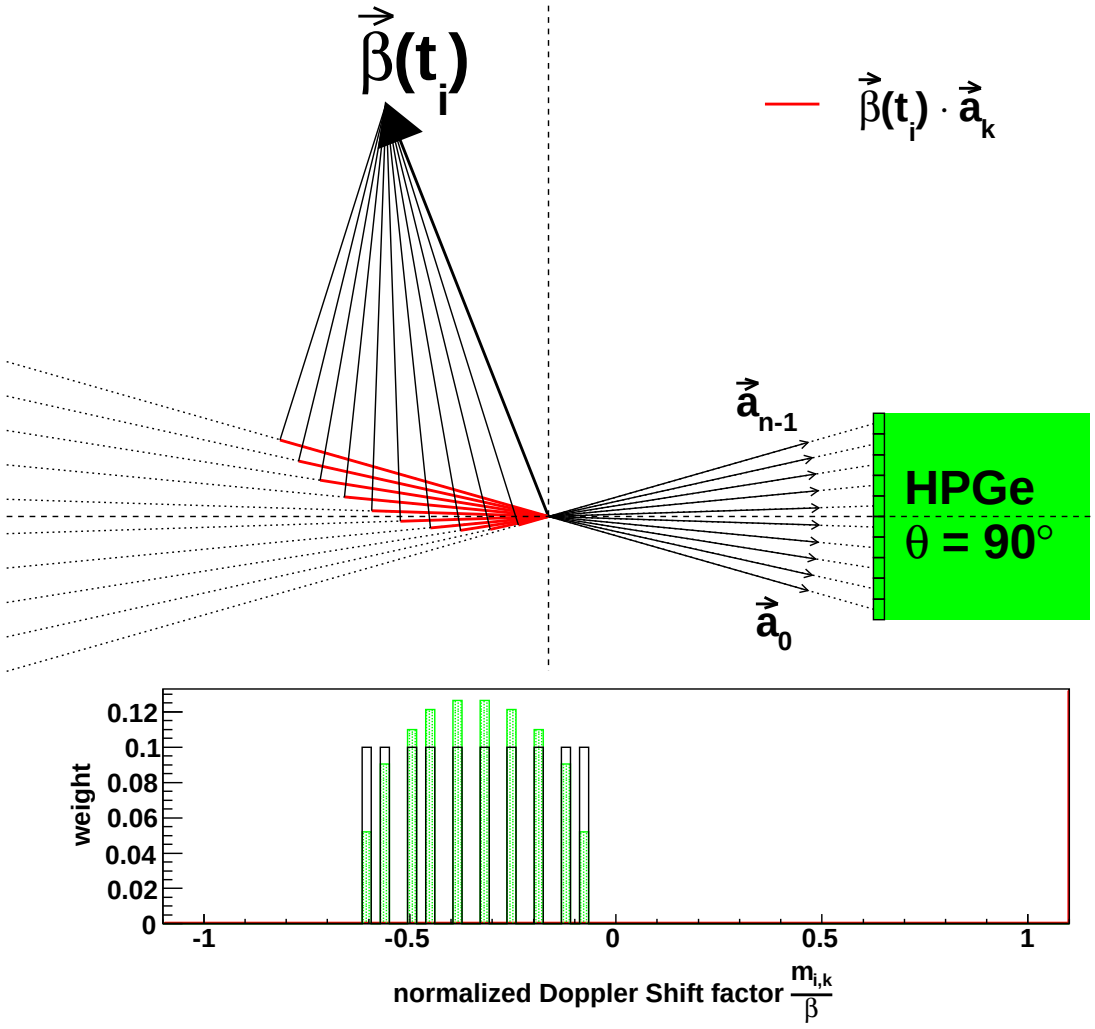

Figure 4.21: The dashed vertical and horizontal lines indicate the z-axis (beam) and x-axis, respectively. The green HPGe detector is positioned at 90° with respect to the beam axis. The black boxes on the detector's surface indicate the grid of n pixels. The vector of observation $\overrightarrow{a}_{\mathrm{k}}$ of each pixel is defined by the origin of $\overrightarrow{\beta}(t_{\mathrm{i}})$ and the pixel's center. The red lines $\mathrm{m_{i,k}}$ indicate the projections of the velocity vector on the observation vectors. The calculated Doppler shift factors $\mathrm{m_{i,k}}$ (see Equation 4.4) are histogrammed normalized to β below the schematic diagram (black). The green histogram considers the dimension of the HPGe detector in y and weights the contribution of each pixel by its solid angle.

accumulated. In first order, the m_k factor corresponds to the ion velocity projection $\overrightarrow{\beta}(t_i)$ on the vector of observation $\overrightarrow{a}_k$ (see approximation in Equation 4.4).

Each detector covers on opening angle of up to $\theta \approx 52°$. The line shapes can be reproduced by the simulation, because the projections on a fine grid of pixels ($1{\times}1$ mm^2) on the detector surface are histogrammed.

A one dimensional histogram for each detector and each time step is constructed. With thousands of simulated ions, a distinct distribution of expected Doppler shift factors is obtained. Combining those histograms of all time steps into a two dimensional histograms for each detector, the time is plotted on the x-axis and the Doppler shift factor m_k on the y-axis. The z-axis gives the probability to observe a certain Doppler shift factor at a certain time. The simulation accumulates 6000 time steps within 6 ps. The three histograms for the detectors at 0°, 90° and 110° are shown in Figure 4.22.

In Figure 4.22, it is noticeable that the mean of the $m_k(t)$ factors for the detector at 0° ((a), forward angles) is positive and for the detector at 110° ((c), backward angles) is negative, while the mean for the detector at 90° (b) is slightly negative, which can be explained by the position of the Silicon detectors as described in section 2.4. Even though the detector is positioned perpendicular to the beam axis, the majority of the γ-rays are observed under backward emission angles.

The histogram for the detector at 0° shows negative entries for the $m_k(t)$ factors, although the detector covers forward angles, only. The effect can be explained with angular straggling which increases for small energies. Considering the opening angle of the HPGe detector, negative projections come from ions with $\theta > 90° - 26° = 64°$. Depending on the lifetime, this can cause a tail in the E_γ line shape to low energies.

4.3.3 APCAD: From the Velocity Projections to the Line Shape

The following section describes how the line shape in the E_γ spectrum is calculated from the $m_k(t)$ matrix, evolved in section 4.3.2. As an example, spectra from the detector at 0° are shown. A reduced time resolution is chosen to demonstrate the procedure.

Figure 4.23(b) shows the $m_k(t)$ factor versus the time after excitation for all simulated ^{31}S* as described in the previous section. The projection onto the m_k axis of a showcase time bin is shown in (a). The integral (red) is normalized to the number of virtual pixels and the number of simulated ions, but weighted by the relativistic change in the solid angle. The showcase time bin in (a) is indicated in (b) by a red frame.

Assuming a lifetime of $\tau = 0.5$ ps, the number of nuclei de-exciting within a time bin is calculated applying the Equation 1.19, $A(t) = A_0 \exp(-t/\tau)$. The histogram with a total number of $A_0 = 10^6$ de-exciting nuclei is shown in Figure 4.24. The time binning is chosen to match the binning in the $m_k(t)$ histogram in Figure 4.23(b). The probability distribution for m_k of each time bin in Figure 4.23(a) is now scaled with the according number of de-excitations within the chosen time bin in the histogram in Figure 4.24 and plotted in a new histogram, showing the number of expected γ-rays and their Doppler shift factor distribution m in Figure 4.25. The red integral is the product of the m_k distribution multiplied with the number of de-exciting nuclei within the showcase time bin. The blank histograms originate from the other time bins.

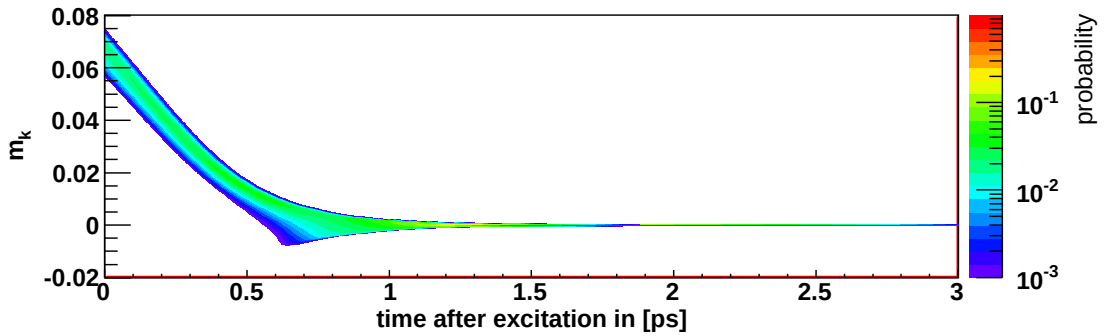

(a) HPGe detector at $(\theta, \phi) = (0°, 0°)$

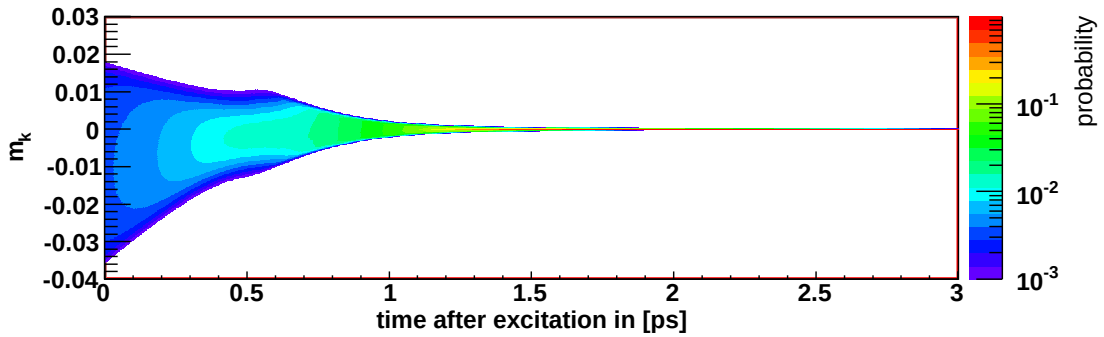

(b) HPGe detector at $(\theta, \phi) = (90°, 180°)$

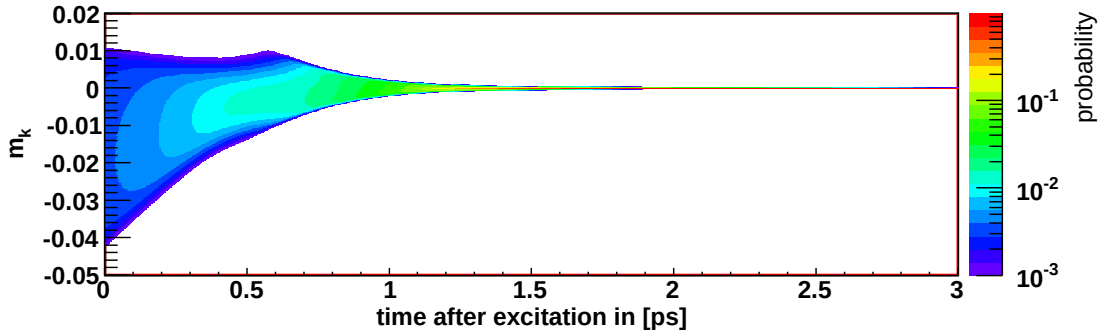

(c) HPGe detector at $(\theta, \phi) = (110°, 0°)$

Figure 4.22: The probability (color coded) of the observed Doppler Shift factor m_k is plotted on the y-axis versus the time on the x-axis.

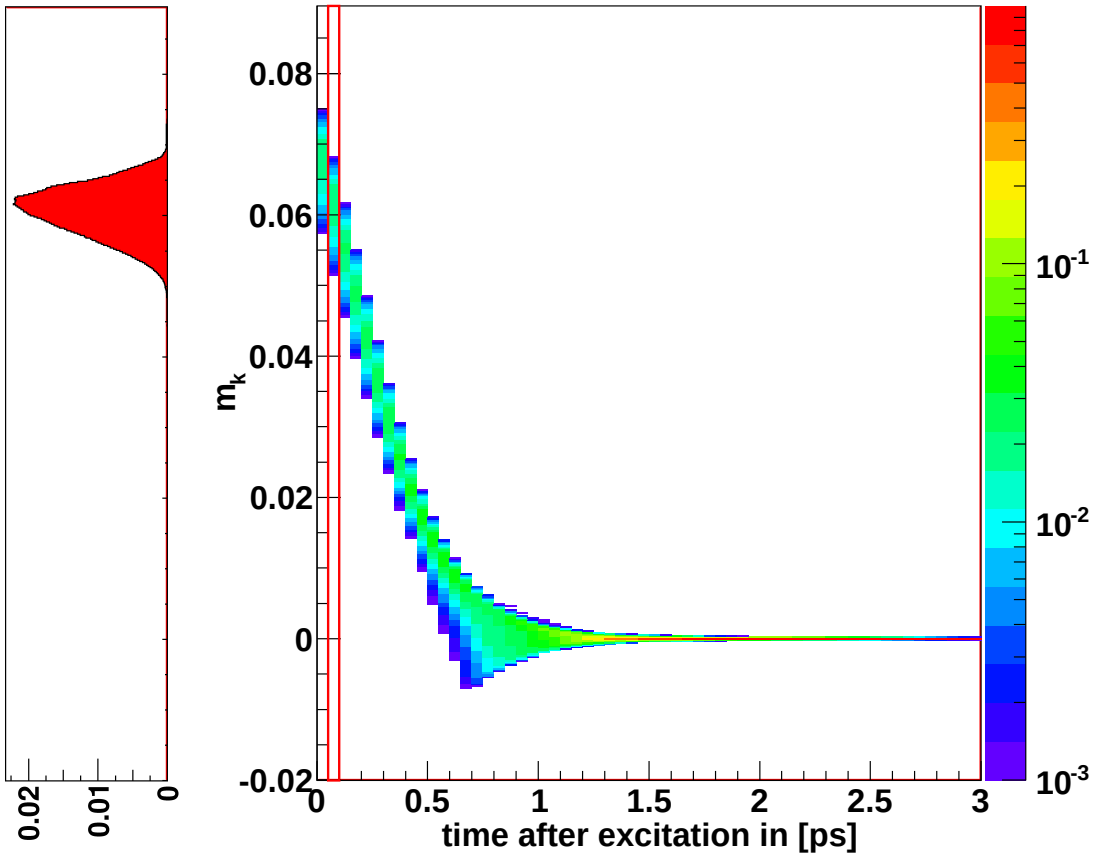

(a) (b)

Figure 4.23: (a) shows the projection of probability of the red marked time bin in (b) on the m_k axis. (b) shows the probability distribution of the Doppler shift factors m_k of the simulated ions (y-axis) and the time after excitation (x-axis). For demonstration, a low time resolution has been chosen.

The sum of the contributions of the histograms in Figure 4.25 is shown in Figure 4.26(a). The red area indicates the contribution of the showcase time bin marked in the previous histograms.

The energy distribution of a Doppler affected observation of a transition energy $E_0 = 1248.9$ keV is given by

$$(E_\gamma^{phys})_{bin} = (1 + m_{bin}) \cdot E_0 \tag{4.5}$$

with the Doppler shift factor m. This formula is applied on each bin center on the m-axis in Figure 4.26(a) and the bin entries are accumulated in a new E_γ^{phys} histogram as shown in Figure 4.26(b). The histogram shows the physical E_γ^{phys} distribution due to the lifetime and the Doppler shifts, which depend on the stopping process within the target.

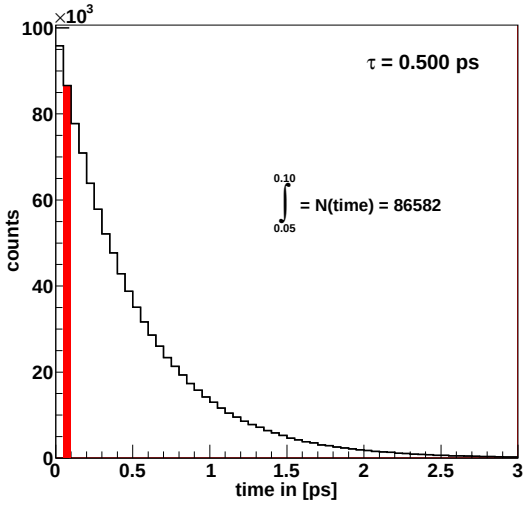

Figure 4.24: Activity function of one million excited nuclei with a lifetime of $\tau = 0.5$ ps. The integral of the red highlighted bin is quoted.

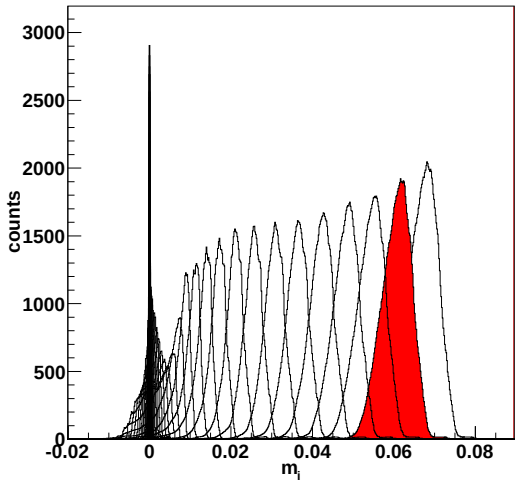

Figure 4.25: The m_i distribution of each time bin is scaled by the number of decays within this time bin. The results are plotted separately for each time bin. The red highlighted histogram in (b) originates from the red highlighted bin in the histograms in Figure 4.24 and Figure 4.23(a).

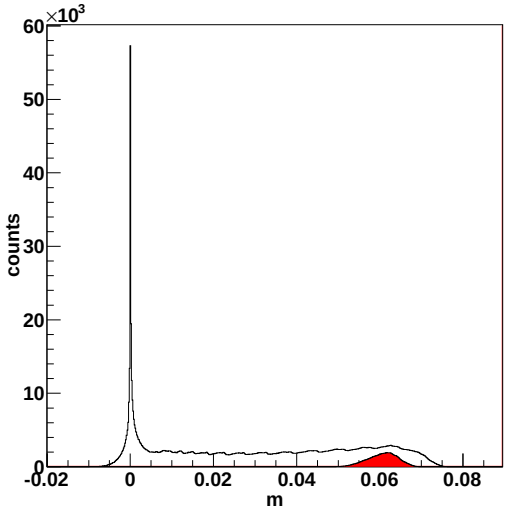

(a) The activity weighted m distributions of each time bin are accumulated in this histogram.

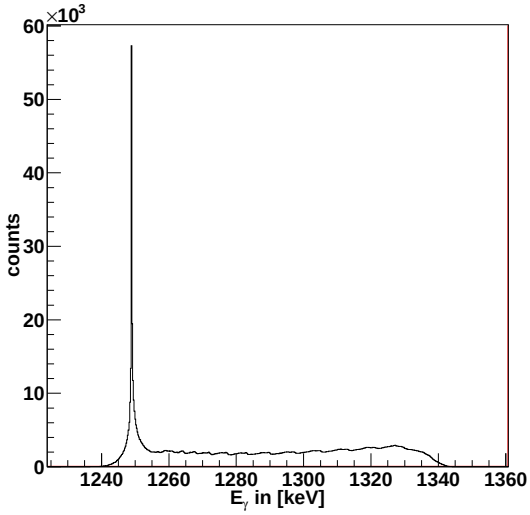

(b) E_γ^{phys} spectrum of the observed γ-rays in the detector at 0°.

Figure 4.26: The spectrum of the Doppler shifted γ-ray energies E_γ^{phys} emitted in the direction of the detector is calculated by applying Equation 4.5 on each m bin center m_{bin} in (a).

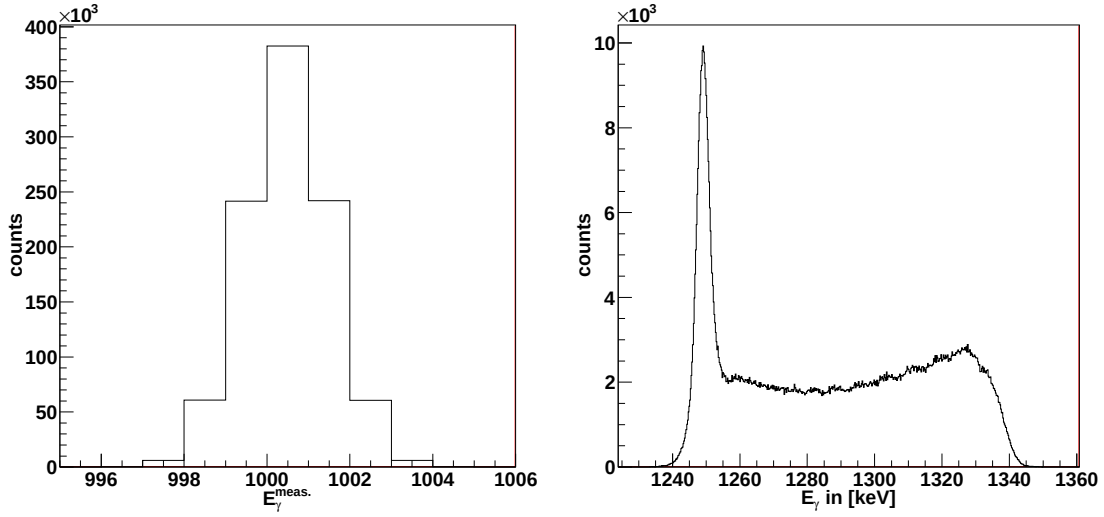

(a) HPGe Detector $E_\gamma^{meas.}$ response on a delta E_γ^{phys} peak.

(b) $E_\gamma^{meas.}$ spectrum of the observed γ-rays in the detector at 0°.

Figure 4.27: Effect of the HPGe detector response function on the measured energy.

In order to reproduce the line shape in the experimental measured E_γ spectrum, the response function of the HPGe detector needs to be applied on the E_γ^{phys} spectrum. For this demonstration, a Gaussian response function is chosen. Figure 4.27 shows such a detector response on a delta energy function. The centroid and the number of counts are conserved, but the peak is smeared out due to the limited energy resolution of the detector. The width is defined by the sigma of the Gauss function.

The response function is applied on the entries of each energy bin in the E_γ^{phys} spectrum and accumulated in a new $E_\gamma^{meas.}$ spectrum, which is shown in Figure 4.27 (b).

The final $E_\gamma^{meas.}$ line shape is the convolution of the spectrum of the Doppler shifted γ-rays emitted into the direction of the detector $E_\gamma^{phys.}$ with the detector response function. The energies $E_\gamma^{phys.}$ are calculated from the distribution of the Doppler shift factors shown in Figure 4.26(a), which in turn is the convolution of the decay function with the projected stopping matrix. The modeled line shape from Figure 4.27(b) can be fitted to the experimental data by varying the assumed lifetime in the decay function and the number of total events as it will be shown in the next section 4.3.4.

The APCAD program uses the described procedures to model the line shapes. It includes the following additional features (for more details, see [Sta11]):

- Support of γ array detector setups. Continuous angle (within some resolution of the detectors) E_γ spectra can be used to determine the lifetime.

- Spectra from all available angles are fitted simultaneously. This avoids local optimums in the parameter space of the fit.

- Relativistic effects on the opening angles of the HPGe detectors are considered.
- A spatial beam spread can be introduced in the simulation, which is taken into account for selecting the events, where the ejectiles hit the particle detectors.

4.3.4 Fitting: The Experimental Data and the Modeled Line Shape

The line shapes of the detectors at all angles have been fitted simultaneously. The individual line shapes are modeled as demonstrated in section 4.3.3 and are compared with the experimental data by calculating the χ^2 [Bev92] of all bins within the fit ranges r:

$$\chi^2 = \sum_{i \ \epsilon \ r} \left(\frac{y_{\mathrm{data,i}} - y_{\mathrm{model,i}}}{\sigma_{\mathrm{data,i}}} \right)^2 \tag{4.6}$$

with the content of the i^{th} bin $y_{\mathrm{data,i}}$ and its error $\sigma_{\mathrm{data,i}}$ of the experimental data and the modeled bin content $y_{\mathrm{model,i}}$.

A best fit is obtained by minimizing the χ^2, using the MIGRAD fitting routine which is included in ROOT. The following parameters are free fit parameters and are varied to minimize the χ^2:

- lifetime τ
- transition energy E_0
- number of events
- expansion coefficients of the γ-ray angular distributions $W(\theta)$ [Sta11]

$$W(\theta) = 1 + F_2 \cos(\theta) + F_4 \cos(\theta) \tag{4.7}$$

- offset of the horizontal background

Additional parameters have been fixed:

- The parameters of the HYPERMET HPGe detector response functions as quoted in A.3
- The linear slope in the background has been fixed to 0.

The best fit line shapes and the parameters are presented and discussed in chapter 5.

Chapter 5

Results and Discussion

After background subtraction, as discussed in section 4.2.7, the Doppler attenuated spectra of the ^{31}S first excited state to ground state transition (^{31}S: 1249 keV $\rightarrow$ GS) from all three HPGe detectors, were simultaneously fit by the previously described model spectra.

The fits were performed using a χ^2 minimization method, which applied the MIGRAD [Jam04] routine that is included in the ROOT libraries. The derived fit results for the HPGe detectors at 0°, 90° and 110°, are shown in Figures 5.1, 5.2 and 5.3, respectively. Only those data points contained within the blue brackets were used in the simultaneous fitting. The small peak at 1226 keV has been excluded, because it is caused by background γ-rays and is not part of the line shape (see section 4.2.7).

From the fits, the lifetime is found to be:

$$\boxed{\tau = (964 \pm 19(\text{stat.}) \, ^{+311}_{-89}(\text{syst.})) \text{ fs}}$$

with a reduced χ^2 of 1.4, for 208 degrees of freedom. The fit parameters are given in Table 5.1.

The negative values for the background offsets are caused by the background subtraction (see chapter 4.2.7) in the pre-processing of the data. The background consists

free parameter	value	±	stat. error
background offset 0°	−50.8	±	8.4
background offset 90°	−9.1	±	7.0
background offset 110°	−15.9	±	7.4
transition energy	(1248.79	±	0.03) keV
number of events	12338	±	247
lifetime τ	(964	±	19) fs
AngDistF2	0.346	±	0.024
AngDistF4	0.039	±	0.045

Table 5.1: Free fit parameters and their best fit values.

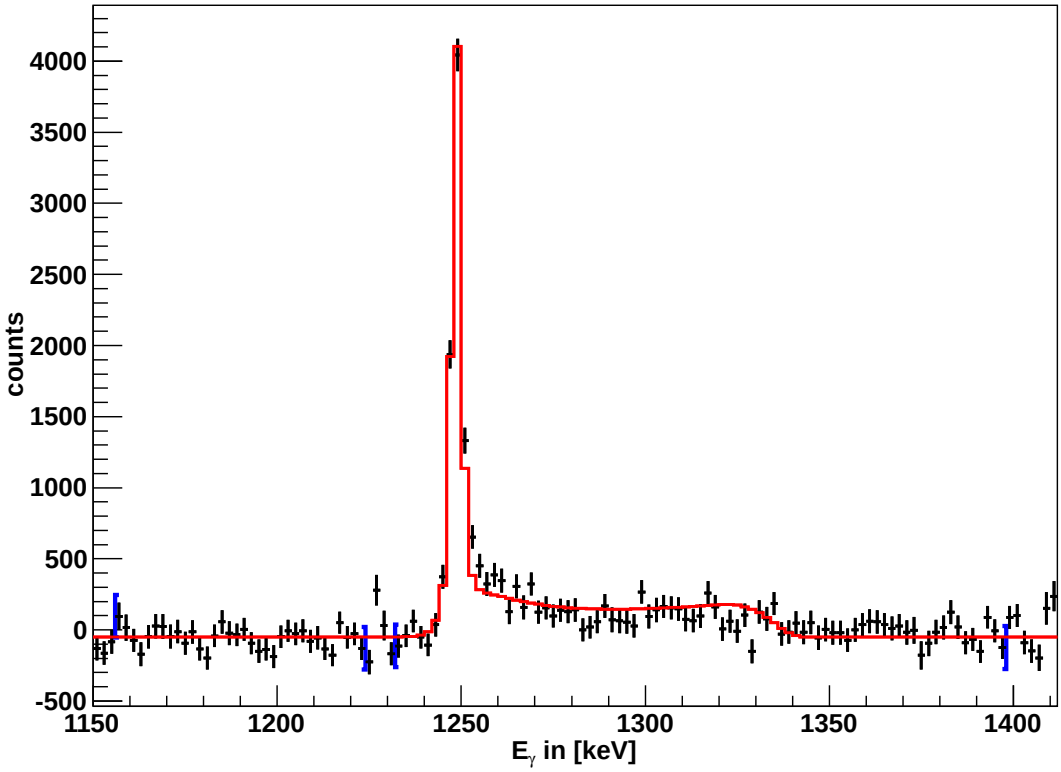

Figure 5.1: Experimental data and fitted line shape in the E_γ spectrum from the detector at $(\theta, \phi) = (0°, 0°)$.

of events, forming structures or peaks and a continuum in the E_γ spectra. Both components grow with different time dependences. The removal of the structures has been the priority because these could affect the determined lifetime by leading the fit routine into a wrong description of the real line shape. Removing those structures causes an offset that has been considered with free parameters for the background offset.

The parameters of the angular γ-ray distributions AngDistF2 and AngDistF4 control the number of the events in the spectra of the HPGe detectors at the different angles as described in Eq. 4.7. If HPGe detectors with a high angular resolution would be used (n angular bins), this reduces the number of free parameters that describe the number of events in each detector, to three (number of events, AngDistF2, AngDistF4) instead of having n free parameters. Because only three non-segmented detectors were used in the commissioning experiment, the number of free parameters is the same. The large statistical errors in AngDistF2 and AngDistF4 can be explained with the high correlation coefficients to other free parameters as the second AngDist factor and the total number of events.

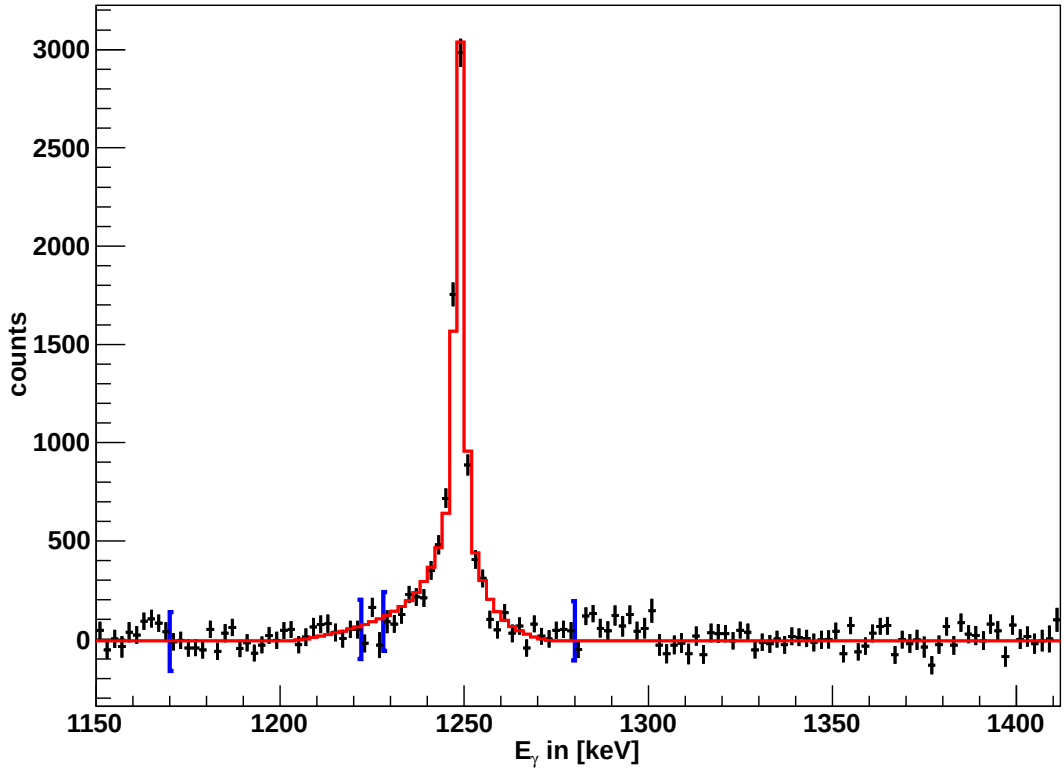

Figure 5.2: Experimental data and fitted line shape in the E_γ spectrum from the detector at $(\theta, \phi) = (90°, 0°)$.

5.1 The Discussion of the Errors

Compared to the dominating systematic errors, the statistical error in the determined lifetime is small. The statistical error has been determined from error matrices in the MIGRAD fit routine [Jam04].

The following section discusses possible systematic error sources and their influence on the determined lifetime. Three types of systematic effects have been studied:

- Uncertainties in the geometry of the setup: The positions of the Si telescopes, the HPGe detectors and the beam spot position on the target have been varied in the simulation that is used for the line shape modeling to study the effect on the determined lifetime.

- Uncertainties in the target: The stopping power of the ^{31}S ions in gold and the thickness of the ^{3}He implantation layer below the gold surface have been varied in the simulation.

- The effect of the applied differential cross section in the simulation has been studied in comparison to the Fresco differential cross section [Tho06], using a

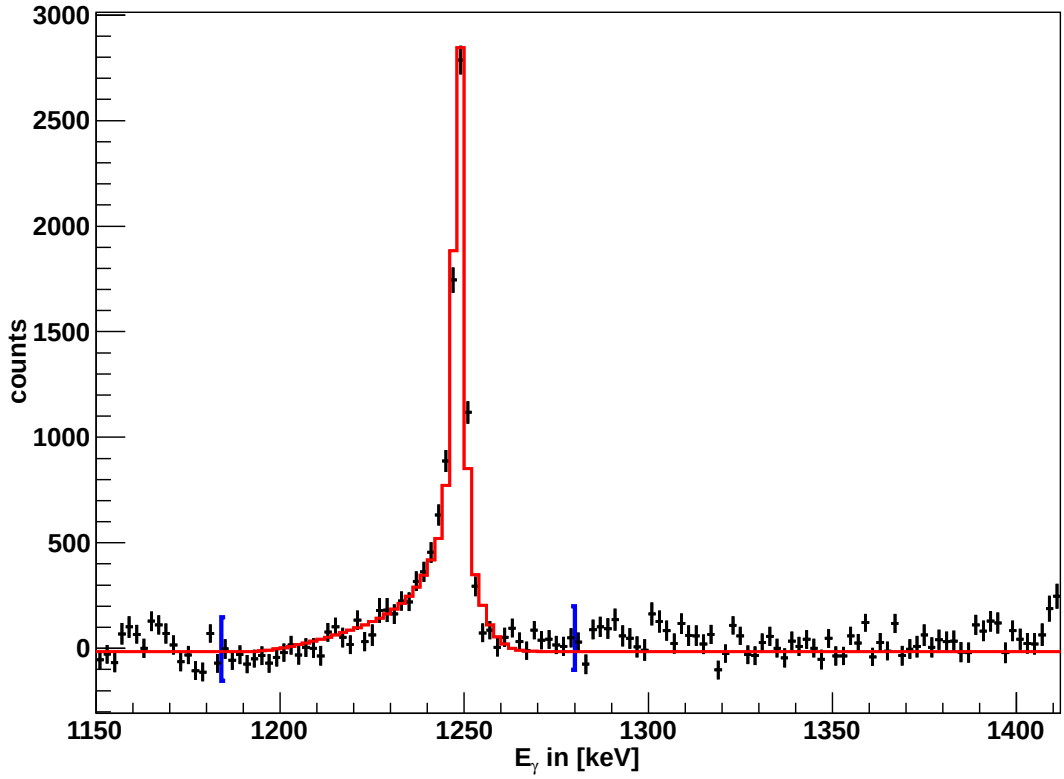

Figure 5.3: Experimental data and fitted line shape in the E_γ spectrum from the detector at $(\theta, \phi) = (110°, 180°)$.

hypothetical isotropic and the experimental cross section from McQueen et al. [McQ70] without an energy dependence.

The detailed variations and their influences on the determined lifetime are presented in Figure 5.4. The red horizontal line indicates the nominal result of the lifetime and the red belt indicates its statistical error. The plotted points show the effect of the systematic uncertainties on the determined lifetime. The corresponding, vertical error bars indicate their statistical errors.

The determined lifetime is insensitive to reasonable variations in the geometry of the setup such as small changes in the distances or positions in the detectors or the beam spot position. The deviations in the determined lifetime agree with the nominal result within the statistical errors. A 20% increase of the thickness of the ^{3}He implantation layer below the gold surface has no crucial effect, because the energy loss of the ion beam within this layer is small, and so the spread of initial velocities of the ^{31}S* nuclei is small.

The uncertainty in the stopping power of ^{31}S in gold dominates the systematic uncertainty in the lifetime. The Geant4 simulation applies stopping power data from the ICRU reports ("Stopping of Ions Heavier Than Helium (Report 73)" (2005/2009) that

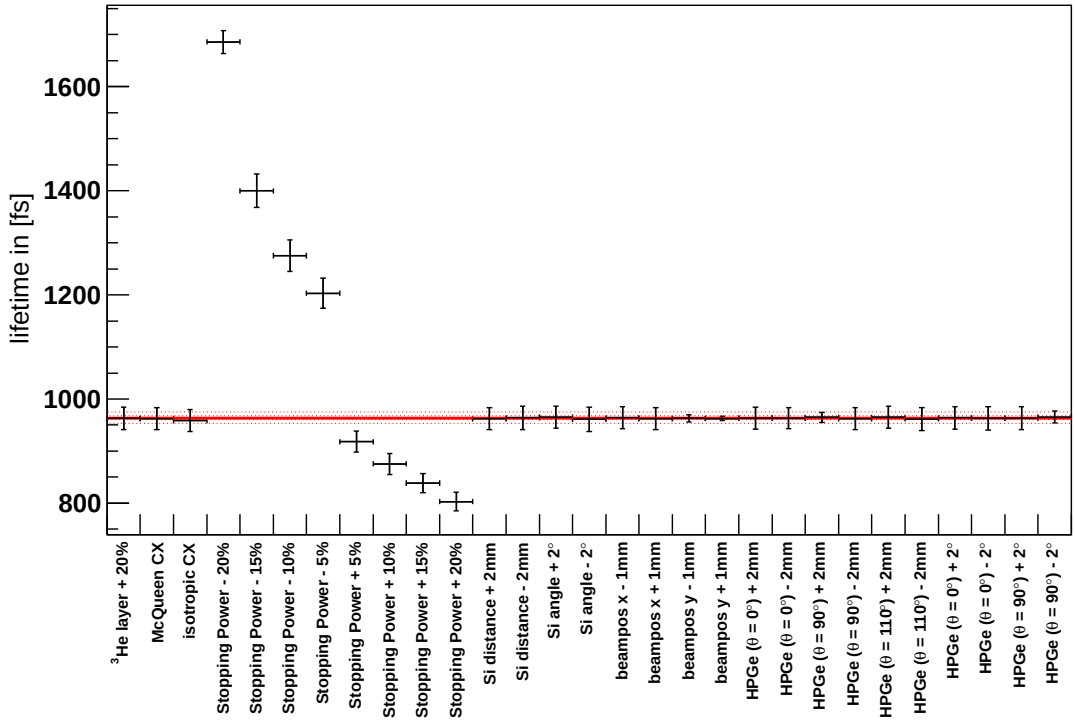

Figure 5.4: Statistical and systematic errors: the red horizontal line indicates the nominal result of the lifetime measurement of the first excited state in ^{31}S with its statistical uncertainty (red belt). The data points plot the determined lifetimes after the variations of possible systematic uncertainties.

"presents a critical survey on measurements and calculations of quantities governing the penetration of heavy ions through condensed and gaseous matter over an energy range from 1 keV/u upward" [RU09]. For the study of systematic errors, the dE(E)/dx was scaled upwards and downwards from its nominal value by ±20%, in steps of 5% (see Figure 5.4).

The simulations with different scaling factors for the stopping power allow the calculation of the fraction of stopped ^{31}S ions that correspond to detected ^{4}He ejectiles as a function of the scaling factor for the stopping power as shown in Table 5.2. The data points are plotted in Figure 5.5 and have been connected with a smooth line to guide the eye. A plateau is observed for scaling factors $> 95\%$ while a significant change is observed for scaling factors $< 95\%$. A ratio of 1.0 is not met because of back scattering of ^{31}S nuclei on the gold nuclei.

A six hour beam experiment was performed to demonstrate that all ^{31}S ions were stopped in the target, and the uncertainty in the stopping power must be in the range of the plateau in Figure 5.5. To do this, a Si detector was positioned downstream of the target foil and aligned on the beam axis. The target was rotated about the y-axis by

scaling	ratio of stopped ions
120%	99.991%
115%	99.938%
110%	99.954%
105%	99.940%
100%	99.956%
95%	99.814%
90%	98.991%
85%	94.351%
80%	82.803%

Table 5.2: Fraction of stopped ^{31}S in % in dependence of the stopping power scaling factor.

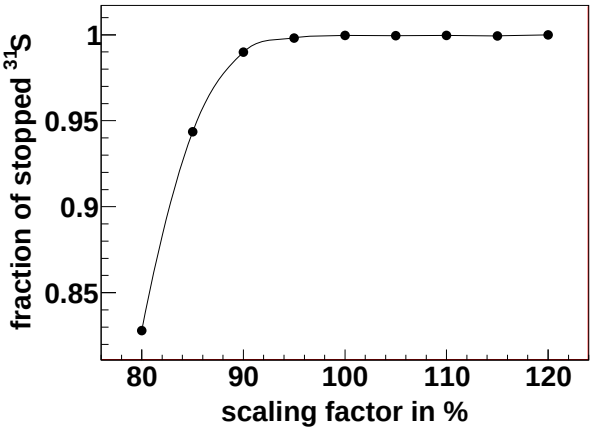

Figure 5.5: Fraction of stopped ^{31}S ions as a function of the stopping power scaling factor.

$\theta = 60°$ and $\theta = 40°$. The $\theta = 60°$ rotation was chosen, because the effective thickness in the beam direction at this rotation angle corresponds to the effective thickness of the target seen by the ^{31}S ions that are in coincidence with the detected ^{4}He ejectiles and a target rotation angle of $\theta = 54°$ during the commissioning experiment. The target rotation of $\theta = 40°$ was chosen to allow beam particles to penetrate through the target foil and be detected in the Si detector. The rates in the Si detectors for both target rotations have been normalized to the beam current and then have been compared to each other. The normalized rate with the target rotation of $\theta = 60°$ was in the order of 0.1 Hz/ppA while the rate with the target rotation of $\theta = 40°$ was at least 5000 times higher. Even though the beam current was too small to be measured with the sensitivity of a Faraday cup (an upper limit of the beam current of $I < 1$ epA with charge state 8^+ was estimated for the normalization), the rate in the Si detector was in the the kHz range. Both measurements were consistent for all used targets and show that all ^{31}S ions were stopped in the target during the commissioning experiment. The very low rate for the target rotation of $\theta = 60°$ can be explained with elastically scattered light particles (e.g. impurities on the target surface).

Besides the stopping power of ^{31}S in gold, the assumed target thickness in the simulation could also effect the fraction of target-penetrating ^{31}S ions. The target thicknesses were determined from the weights of the targets as well as from a measurement, where the energy loss of α- particles from a ^{241}Am source were measured. The results from both methods agreed within 5%.

Taking the results from the simulations in Table 5.2 and Figure 5.5 into account, the experimental data sets a limit to the uncertainty of the decreased stopping power. A first significant change in the fraction of stopped ^{31}S nuclei as a function of the stopping power scaling factor in Figure 5.5 can be observed for factors smaller than 95%. Therefore, to be conservative, an uncertainty of $\pm 10\%$ in the stopping power will be assumed to estimate the influence on the determined lifetime, resulting in $\Delta\tau_{\text{syst.}} = ^{+311}_{-89}$ fs.

The described estimations in the stopping power uncertainty neglect the ambiguous energy dependence in the stopping power. The comparison between parametrization models such as SRIM [Zie08] or "ICRU - Report 73" [RU09] among each other and measurements of stopping powers show that this is an active research area and significant deviations exist between the evaluations of stopping powers. Therefore, future DSAM experiments should include subsequent studies of the stopping power in the used target, achieving an independence on models and exact target compositions.

The deviations in the determined lifetime due to the applied differential cross sections in the simulation is small compared to the statistical errors. This is caused in the small angular range ($\Delta\theta_{\mathrm{lab}} = 1.5°$) of the excited ^{31}S ions in the lab frame (see Figure 2.7) that correspond to the detected ^{4}He ejectiles. The straggling of the ^{31}S ions during the stopping process of $\sigma = 3.4°$ (see Figure 2.2) smears out any angular dependence caused by the cross section.

5.2 The Commissioning of the Facility

The new facility has been commissioned successfully. The new setup has been tested extensively in all categories as the vacuum performance, the target cooling, the silicon detectors, the HPGe detectors, the front-end electronics, the trigger setup and the data acquisition. Also the design of the setup succeeded.

It has been shown that the use of inverse kinematics with its consequences such as complicated ^{3}He implanted targets works sufficiently and allows the observation of larger energy shifts at the same center of mass energy as in direct kinematics. The analysis of the experiment ^{32}S(^{3}He,^{4} He)^{32}S* shows the capability of the setup and the analysis procedures.

5.3 The Comparison of the Result with External Measurements

This section gives a brief overview of previous measurements by other workers of the lifetime of the first excited state in ^{31}S. Their results are quoted in Table 5.3.

After the first measurement in 1970 by Engmann et al. [Eng71] the next measurements were performed roughly 40 years later. Doornenbal et al. [Doo10] have determined the lifetime as a byproduct of in-beam γ-ray spectroscopy studies and with a setup that was not intended for this particular lifetime measurement. This explains their large errors. Another result by Tonev et al. was published in 2011 in a conference proceeding [Ton11].

The lifetime of an exponential decay can be converted to the half life time as shown in Eq. 5.1.

$$\tau = \frac{\mathrm{T}_{1/2}}{\ln(2)} \tag{5.1}$$

[1] I assume this to be the statistical error.

	τ	$\Delta\tau_{\text{stat}}$	$\Delta\tau_{\text{syst}}$
Engmann et al. 1970 [Eng71]	720 fs	108 fs	144 fs
Doornenbal et al. 2010 [Doo10] A	1.2 ps	0.7 ps	$^{+1.3}_{-0.9}$ ps
Doornenbal et al. 2010 [Doo10] B	3.2 ps	4.8 ps	5.2 ps
Tonev et al. 2011 [Ton11]	624 fs	24 fs [1]	
this thesis	964 fs	19 fs	$^{+311}_{-89}$ fs

Table 5.3: Comparison of the determined lifetime with the results from experiments by other work groups.

Engmann et al. [Eng71]: The ^{32}S(^{3}He,^{4} He)^{31}S reaction was applied in direct kinematics with a c.m. energy of $E_{c.m.} = 6.4$ MeV. Therefore, a 7 MeV ^{32}S beam was focused on a ZnS target with a carbon backing. A single 36 cm^3 Ge(Li) detector at $\theta = 90°$ and two Silicon detectors at $\theta = \pm 110°$ with respect to the beam axis were used to trigger on coincidences of γ-rays and ^{4}He ejectiles with the corresponding energy of the level of interest. Due to the kinematics, the detected γ-rays were observed at an average angle of $\theta = 50°$ and $\theta = 130°$ with respect to the trajectory of the emitting ^{31}S nucleus that corresponds to the detected ^{4}He ejectile, causing a difference in the observed Doppler shift.

Two E_γ spectra were compiled, gated on ^{4}He particles in the Si detector at $+110°$ and at $-110°$, respectively. Due to the Doppler effect, the observed peak energies in the two E_γ spectra were shifted relative to each other. The centroids of the two peaks were determined and their Doppler shifts were used to extract the lifetime. The stopping power of ^{31}S in ZnS and C were computed from theory. The systematic error in the lifetime caused by uncertainties in the stopping process has been estimated to be 20% of the lifetime. The lifetimes of the first and the second excited state in ^{31}S have been studied in two separate 3.5 day measurements. "An attempt to measure lifetimes of levels above $E_{ex} = 2.23$ MeV was unsuccessful because of the high background and the low yield of the reaction". This has been confirmed in the commissioning experiment of this thesis for $E_{c.m.} = 7.3$ MeV, since no feeding transitions were observed (see sub section 4.2.5).

The maximum velocity in forward direction is due to the direct kinematics $\beta = 0.015$ c. Inverse kinematics with the same $E_{cm} = 6.4$ MeV would have created a maximum velocity of the ^{31}S nucleus in forward direction of $\beta = 0.074$ c. The sensitivity of inverse kinematics is therefore higher for shorter lifetimes, but the direct kinematics avoids γ-ray background from fusion evaporation.

$$\boxed{\tau = [720 \pm 108(\text{stat.}) \pm 144(\text{syst.})] \text{ fs}}$$

The results of this thesis and Engmann et al. agree within the quoted errors.

Doornenbal et al. [Doo10]: In order to improve the analysis of in-beam γ-ray spectroscopy in ion beam experiments with relativistic energies, lifetime effects on Doppler shift corrections have been studied. In turn, the lifetime can be assumed to bring the simulation and the experimental data to a better agreement. The optimum agreement determines the lifetime of the observed state.

A two step fragmentation technique at relativistic energies has been used to populate the first excited states in ^{31}S and ^{34}Cl. A 420MeV/u ^{40}Ca beam was focused on a ^{9}Be target to provide a ^{37}Ca secondary beam with an energy of 195.7 MeV/u. The secondary beam was focused on a ^{9}Be target, where four (three) protons and two neutrons were removed from the ^{37}Ca to create ^{31}S (^{34}Cl). The excited ^{31}S nuclei have been decelerated from 0.51c to 0.46c within the target, but were not stopped.

For the γ-ray observation, eight highly segmented MINIBALL HPGe detectors [Ebe01] were positioned in two rings at angles of $\theta = 51°$ and $\theta = 85°$ with respect to the beam axis (set "B"). 15 additional Cluster HPGe detectors [Ebe96] were positioned in three rings at $\theta = 16°$, $\theta = 33°$ and $\theta = 36°$ with respect to the beam axis (set "A").

Two sets of data from both HPGe detector arrays (A and B) were acquired and analyzed separately. The position of the reaction and the direction of the outgoing particles were tracked with position sensitive Silicon detectors. Due to the segmentation of the HPGe detectors, the position of the detection of the γ-ray and the target center along the beam axis determined the emission angle. This has been used to correct the E_γ spectra for the Doppler effect. Depending on the lifetime of the observed state, the Doppler shift correction can be inaccurate, since the exact longitudinal position of the de-exciting nucleus and the velocity varies from event to event.

Therefore, a Monte Carlo simulation (GEANT4 [Ago03]) was used to study this effect. The (primary Doppler shift corrected) line shapes were modeled assuming a lifetime of the observed state. Thus, the lifetime could be determined by χ^2 minimization of the data from the experiment and the simulation. The results are quoted in the half life of the state:

$$\boxed{\text{A: } T_{1/2} = [0.8 \pm 0.5(\text{stat})^{+0.9}_{-0.6}(\text{syst})] \text{ ps}}$$

$$\boxed{\text{B: } T_{1/2} = [2.2 \pm 3.3(\text{stat}) \pm 3.6(\text{syst})] \text{ ps}}$$

The large systematic errors in both measurements are mainly caused by uncertainties in the position of the detectors relatively to the target and the determination of the velocity of the beam ions after the secondary target. The authors claim that "the secondary beam and target thickness were not designed to measure lifetimes specifically". The systematic error of the MINIBALL detectors is claimed to be "independent of the half life, offering an interesting tool to measure half

lives $\geqslant$ 20 ps". They emphasize that this study shows the limits of the setup and the lifetime determination of the first excited state in ^{31}S. For lifetimes below 1 ps, the authors suggest the usage of high density targets (e.g. Au) to increase the sensitivity.

Tonev et al. 2011 (Conference Series) [Ton11]: For a study of the isospin symmetry in the mirror nuclei ^{31}S and ^{31}P, a ^{20}Ne beam with an energy of 33 MeV has been focused on a ^{12}C target, allowing fusion evaporation reactions that populate states in both nuclei. The lifetime was determined, using the DSAM technique.

The γ-ray detector array GASP [Alv93] was used, covering a large solid angle. A 0.75 mg/cm^2 Carbon target was used on a 10 mg/cm^2 gold backing. The reactions of interest were ^{12}C(^{20}Ne, n)^{31}S and ^{12}C(^{20}Ne, p)^{31}P. For ^{31}S events, $\gamma\gamma$ coincidences were used and the state of interest (1249 keV) has been fed from higher states.

Therefore, it was necessary to know the lifetimes and transition probabilities of all feeding states, which introduces uncertainties in the determined lifetime. Additionally, the reaction could have taken place anywhere in the ^{12}C layer of the target. Even though the ^{20}Ne beam looses 6.5 MeV within this layer, the energy is sufficiently above the fusion barrier (PACE [Tar03]). This results in a 20% spread of the kinetic energy at the moment of the fusion and therefore, a large uncertainty in the velocity at the moment of the ^{31}S production.

The authors claim a systematic error in the lifetime of 10% due to uncertainties in the stopping power that is included in the final error.

$$\boxed{\tau = [624 \pm 24] \text{ fs}}$$

The result of the commissioning experiment in this thesis does not agree with the result from Tonev et al. Their errors quoted in the proceeding have not been discussed in detail by the authors, but they seem to be inconsistent with their own. The combined statistical and systematic errors of 4% of the determined lifetime is even smaller than the claimed 10% for the systematic error from uncertainties in the stopping power. Since the conference series is the only publication of this result, the analysis might be ongoing.

The major challenge in all DSAM experiments is the uncertainty in the stopping power of the used target. If fusion evaporation reactions are used, the direct population of the state of interest is not assured. Therefore, feeding effects need to be considered in the analysis, including the lifetimes of the feeding states and their transition probabilities. This introduces additional uncertainties in the determined lifetime.

Chapter 6

Conclusion and Outlook

The development of a new facility for lifetime measurements of excited states at the MLL using the Doppler Shift Attenuation Method (DSAM) has succeeded. For commissioning, the lifetime of the first excited state in ^{31}S has been determined and compared with measurements by other workers. On this date, the setup is in a ready-to-use state and can easily be extended with additional or segmented HPGe detectors to improve the γ-ray efficiency and the position sensitivity. In this context the MINIBALL campaign at the MLL will allow to use position sensitive HPGe detectors [Ebe01] that will make use of the full capability of the analysis software APCAD [Sta11].

In general, the error in the determined lifetime is not dominated by uncertainties in the experimental setup, but in the stopping power of the used target material. Future lifetime measurements could go along with studies of the stopping power of the used target material. This could be realized in measurements of the energy loss in a rotatable target. Hence, a dE/dx mapping can be acquired that can be consulted in the lifetime analysis.

The nuclei, whose lifetimes of their excited states can be studied are limited by the available (stable) ion beams at the laboratory and the targets. In order to access the full capability, the setup will be expanded with a neutron detector. While the present experimental setup requires charged particles in the outgoing channel, the neutron detector will widen the possible reactions and the accessible nuclei, by using (^{3}He, n) reactions for example.

The data acquisition system will be upgraded to a fully digital system that allows pulse shape analysis for the discrimination of γ-rays and neutrons that will be observed with the neutron detector. Using a sampling digitizer with time stamping, the electronic setup will be reduced and simplified. The accelerator at the MLL can provide a pulsed beam, which makes time of flight measurements of the ejected neutrons feasible, allowing the use of the kinematics to identify events of interest.

Appendix

A.1 The Target Cooling

The temperature of the target ladder has been monitored with a PT100 resistor that was glued to the target ladder. Because its resistance depends on the temperature, the temperature of the target ladder could be monitored by measuring the resistance. The temperature as a function of the time during a cool-down cycle is shown in Figure A.1. It started for $t = 0s$ at room temperature and no beam was focused on the target.

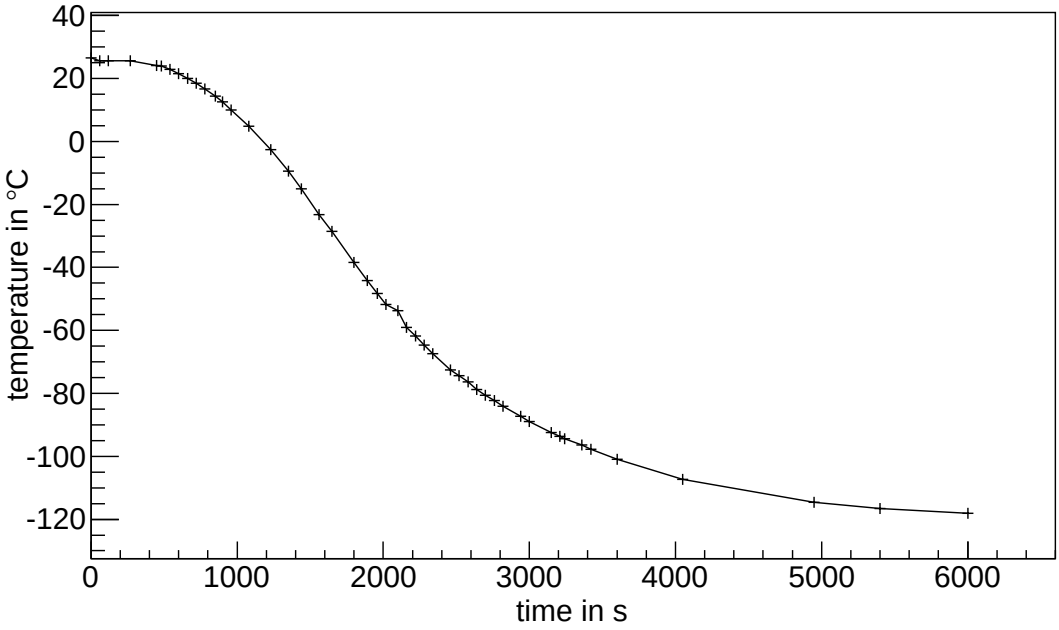

Figure A.1: The temperature of the target ladder as a function of time T(t) during the cool down cycle.

A.2 The Target Temperature

The diffusion of the implanted ^{3}He particles in the Au targets would cause a reduction in yield and prevent acquisition of DSAM E_γ spectra. The mobility of the ^{3}He particles in gold has not been studied in this thesis, but it is known from elastic recoil detection (ERD) analysis that no diffusion occurs at room temperature [Ber12, Ber95]. Therefore, the targets have been cooled with the aim to keep their temperatures below room temperature during the experiment.

The temperature in the target in the beam spot has been estimated with SolidWorks [Das11], which calculates the heat transport and shows the temperatures after an equilibrium has been established. A gold foil with the dimension of the target frames ($25 \times 12.5\text{mm}^2$) and a thickness of 6.3 μm has been assumed. A circular beam spot with a diameter of 3 mm at the center of the target was assumed. For boundary conditions the temperatures of the edges of the foil were fixed to the measured temperature of the target ladder, 174 K and the heat deposition at the beam spot has been set to 0.5 W, which corresponds to the power input from the 85 MeV ^{32}S beam.

The geometry of the target has been simplified in a conservative way in order to solve the problem in two dimensions instead of three. Usually, the gold foil is sandwiched in between two aluminum target frames with 0.2 mm thicknesses. The target frames are then pressed on the cooled, massive copper target ladder. The necessary distances of heat transfer in the thin target gold foil are therefore much smaller than assumed in this calculation. Also the temperature of the target ladder for the ^{3}He runs has been 157 K instead of the assumed 174 K and the beam power was always smaller than 0.5 W. Due to the target rotation the beam spot was larger than assumed in this estimation (see Figure A.5).

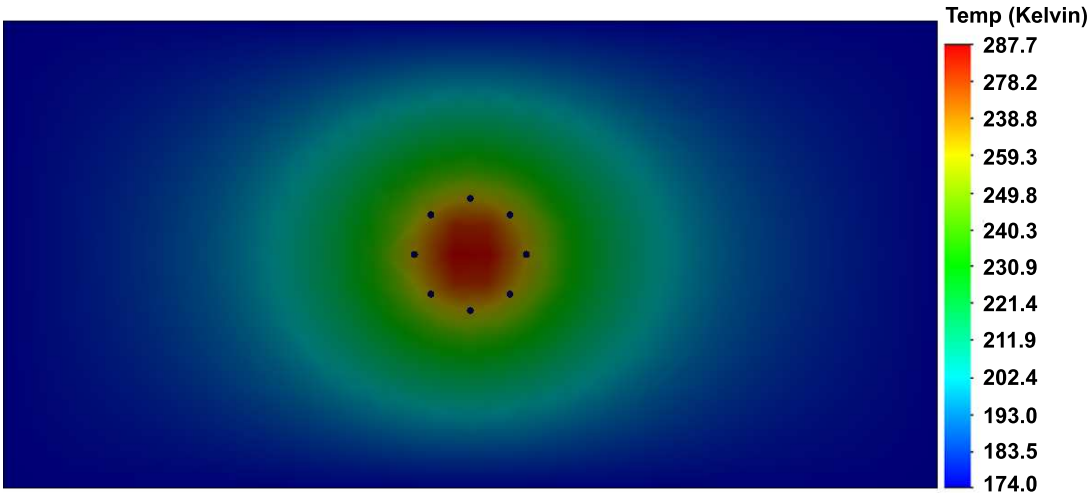

Figure A.2: The temperature distribution in the target after the equilibrium has been established, estimated with SolidWorks [Das11]. A heat power in the beam spot of 0.5 W and a temperature at the edges of 174 K were assumed.

The resulting temperatures in the equilibrium are shown in Figure A.2. The maximum temperature in the beam spot is 287.7 K and still lower than room temperature and therefore ^{3}He diffusion is unlikely.

A.3 The HPGe Detector Response Function

This section presents the HPGe detector response functions, determined from E_γ spectra which were acquired from a ^{152}Eu source. The 1112.1 keV line has been fitted with the HYPERMET function [Phi76] shown below. The individual fits and their parameters for the three detectors are presented in Figure A.3.

$$\mathrm{HYPERMET(E)} = f_{\mathrm{background}}(\mathrm{E}) + f_{\mathrm{sym.}}(\mathrm{E}) + f_{\mathrm{tail}}(\mathrm{E}) \tag{A.1}$$

with the linear background function:

$$f_{\mathrm{background}}(\mathrm{E}) = a + b\ \mathrm{E} \tag{A.2}$$

with the symmetric peak function:

$$f_{\mathrm{sym.}}(\mathrm{E}) = \frac{d(1-f)}{2}\left(\mathrm{Erf}\big[-\frac{1}{e}\ A'\big] - \mathrm{Erf}\big[-\frac{1}{e}\ B'\big]\right) \tag{A.3}$$

with the tail function:

$$\begin{aligned} f_{\mathrm{tail}}(\mathrm{E}) = & \frac{d\ f}{2}\Bigg(\mathrm{Erf}\big[E' + C'\big] - \mathrm{Erf}\big[G' + C'\big] \\ & + \exp\big[D\big]\Bigg(\exp\big[g\ B\big]\Big(1 - \mathrm{Erf}\big[E + F\big]\Big) \\ & - \exp\big[g\ A\big]\Big(1 - \mathrm{Erf}\big[G + F\big]\Big)\Bigg)\Bigg) \end{aligned} \tag{A.4}$$

with the place holders:

$$\begin{aligned} A' &= \mathrm{E} - c - \frac{i}{2} & E' &= \frac{1}{h\ e}B' \\ B' &= \mathrm{E} - c + \frac{i}{2} & F' &= \frac{1}{\sqrt{2}}\ g\ h\ e \\ C' &= \frac{\sqrt{2}-1}{2}\ g\ h\ e & G' &= \frac{1}{h\ e}\ A' \\ D' &= -\frac{g(1-2\sqrt{2})}{4}\ g\ h^2\ e^2 \end{aligned} \tag{A.5}$$

with the parameters "background offset" a, "background slope" b, "peak position" c, "scaling factor" d, "width sigma" e, "tail area" f, "tail steepness" g and the tail diffuseness h.

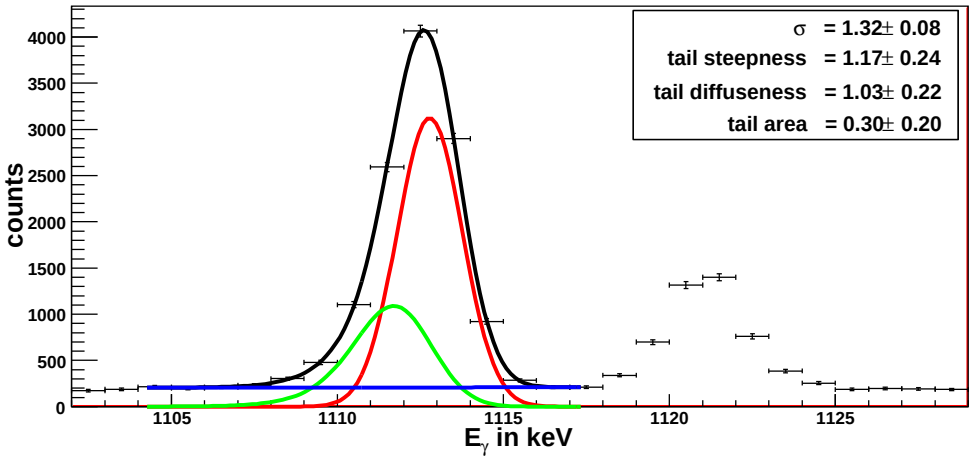

(a) Canberra HPGe detector at $(\theta, \phi) = (110°, 0°)$

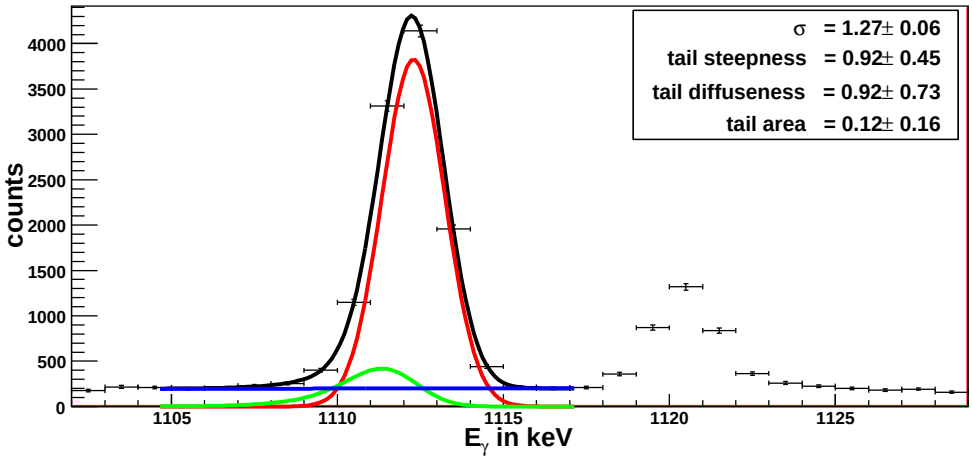

(b) Ortec HPGe detector at $(\theta, \phi) = (90°, 180°)$

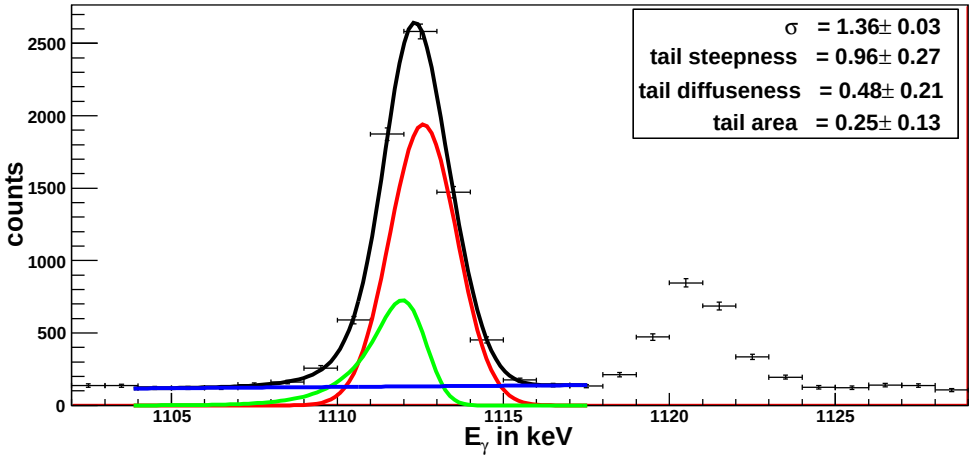

(c) Ortec HPGe detector at $(\theta, \phi) = (0°, 0°)$

Figure A.3: The HYPERMET [Phi76] function has been fitted to the 1112.1 keV line in the E_γ spectra from ^{152}Eu. The parameters characterize the peak shape and describe the detector response function. The components of the function are plotted in red, green and blue, for the symmetric peak, the tail and the linear background, respectively. Their sum is plotted in black.

A.4 The Position Sensitive Silicon Detectors

The so called pin cushion effect causes a non linear behavior of the functions for the hit position and the energy on the measured observables Q_{left} and Q_{right} (refer back to Figure 3.10 for the following section). Therefore, Eq. 3.2 is only correct in first order and higher order corrections are necessary. The effect is studied e.g. in [Sol07].

Only charge which is integrated on the capacities C_L or C_R in the preamplifiers is considered for the measurement of Q_{left} and Q_{right}. Because this capacity is in parallel with the virtual C_i capacities in the depletion layer of the Si detector, not all charge is integrated in the preamplifier, but some fraction remains in the detector. Depending on the particle hit position on the detector, the fraction of neglected charge that stays in the detector changes, which in turn corrupts the determined total charge Q_{total} and the position. If the detector is hit on the very left side for example, all charge flows to the left preamplifier (assuming R_L and R_R to be small) because of the resistive layer on the surface (R_i); the charge does not have to by pass any C_i capacities and all charge is integrated in the preamplifier capacities C_L or C_R. If the detector is hit in its center, half of the charge will flow to the left and to the right preamplifier. On its way, the charges will bypass the virtual capacities C_i and depending on the actual values of C_L and C_R, some fraction will be trapped.

Figure A.4(a) shows the determined Q_{total} from a ^{241}Am α source in arbitrary units on the z axis as a function on the measured x and y position on the detector. Instead of a horizontal plane with no energy dependence, non linear effects are observed. Figure A.4(b) shows a model of the described effect in one dimension, resulting in a sagging position dependence of the observed Q_{total}.

Figure A.4(a) shows that actually even higher effects occur. Therefore the acquired data from the ^{241}Am source has been applied to create a mapping for the energy correction.

The position determination that would normally be derived from Eq. 3.2 is corrupted as well. Therefore, the detectors were covered with a copper mask with 48 holes at defined positions in their active areas, and data from a triple α source (^{244}Cm,^{241}Am,^{239}Pu) was acquired. The real positions in x and y were then plotted as a function of the measured positions (x,y) and were used for the absolute position calibration of the detectors.

The following calibration functions were determined from the source data and used in the analysis of the ^{31}S experiment:

- x-position $X_{\text{real}}(x_{\text{measured}}, y_{\text{measured}})$
- y-position $Y_{\text{real}}(x_{\text{measured}}, y_{\text{measured}})$
- x-energy $E_x^{\text{corr}}(E_x^{\text{measured}}, x_{\text{measured}}, y_{\text{measured}})$
- y-energy $E_y^{\text{corr}}(E_y^{\text{measured}}, x_{\text{measured}}, y_{\text{measured}})$

with E_y^{measured}, x_{measured} and y_{measured} determined by Eq. 3.2. The energy E^{measured} can be determined from the front (y) or back side (x) of the detector.

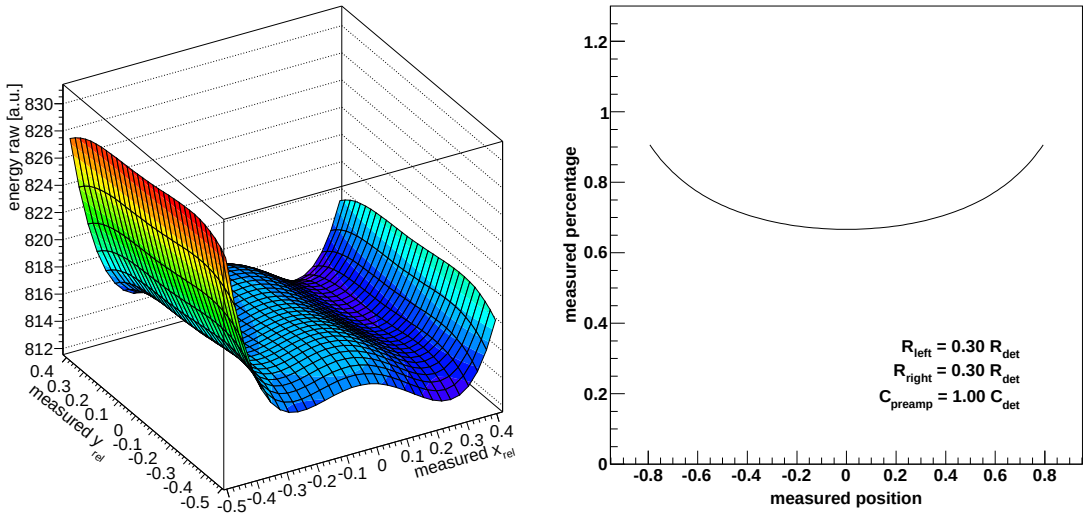

(a) (b)

Figure A.4: The data in (a) shows the energy dependence of quasi mono energetic α particles from a ^{241}Am source on the hit position in one of the used MSPSD detectors. The pin cushion effect is calculated for 1 dimension in (b). The capacities and resistances have been chosen to stress the energy/position dependence. The charge ratio that is integrated on the preamplifiers capacities is plotted on the y axis.

A.5 The Angular Resolution of the Setup due to the Beam Spot Size

The intrinsic position resolution of the MSPSD detectors is in the order of 200 μm [Soi10] which corresponds to an angular resolution in the polar angle θ in the setup of the ^{31}S experiment between 0.3° and 0.2°, if the target is assumed to be a pin point.

If the target is not assumed to be a pin point, but has a finite spot size, this causes a limitation in the angular resolution of the setup. Due to the beam optics on the beam line II/+10 where the DSAM setup is installed, the elliptical beam shape has a horizontal diameter of 3 mm and a vertical diameter of 4 mm. This has also been observed, using the CsI crystal at the uppermost target position. Figure A.5 shows the geometry (a) and the resulting angular uncertainty dependence on the detection angle for the setup of a rotated target (b).

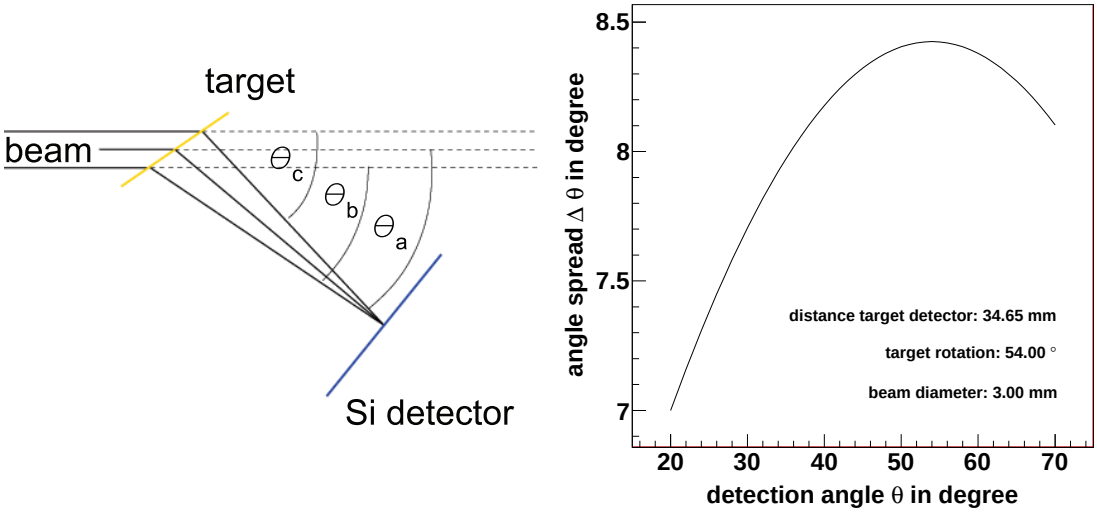

(a) Schematic diagram of the uncertainty of the scattering angle caused by the beam spread.

(b) The angular spread $\Delta\theta$ is calculated by the difference of the maximum and minimum possible polar angle θ_b and θ_c in dependence of the detection angle θ_a

Figure A.5: The polar angular uncertainty from the beam spread. The target rotation increases the effective broadness of the beam spot.

List of Figures

List of Tables

Bibliography

[Ago03] S. Agostinelli, et al., Nuclear Instruments and Methods in Physics Research Section A: Accelerators, Spectrometers, Detectors and Associated Equipment 506(3) (2003) 250 – 303 *Geant4 - A Simulation Toolkit*.

[Akh10] S. Akhmadaliev, *^{3}He Implantation into Gold at the Helmholtz-Zentrum Dresden-Rossendorf*, 2010, private communication.

[Ale81] T. Alexander, G. Ball, W. Davies, and I. Mitchell, Journal of Nuclear Materials 96(1 - 2) (1981) 51 – 56 *A Measurement of the Local Density of ^{3}He-Implanted Metal Foils by the Doppler Shift Attenuation Method*.

[Alv93] C. Alvarez, Nuclear Physics News 3(3) (1993) 012048 *The GASP Array*.

[Ang99] C. Angulo, et al., Nuclear Physics A 656(1) (1999) 3 – 183 *A Compilation of Charged-Particle Induced Thermonuclear Reaction Rates*.

[Aud03a] G. Audi, O. Bersillon, J. Blachot, and A. Wapstra, Nuclear Physics A 729(1) (2003) 3 – 128 *The Nubase Evaluation of Nuclear and Decay Properties*.

[Aud03b] G. Audi, A. Wapstra, and C. Thibault, Nuclear Physics A 729(1) (2003) 337 – 676 *The Ame2003 atomic mass evaluation: (II). Tables, graphs and references*.

[Ber95] A. Bergmaier, G. Dollinger, and C. Frey, Nuclear Instruments and Methods in Physics Research Section B: Beam Interactions with Materials and Atoms 99(1-4) (1995) 488 – 490 *Quantitative Elastic Recoil Detection*, application of Accelerators in Research and Industry '94.

[Ber12] A. Bergmaier, *ERD Density Measurement of ^{3}He Implanted Gold Targets*, 2012, private communication.

[Bev92] P. Bevington and K. Robinson, *Data Reduction and Error Analysis for the Physical Sciences*, WCB/McGraw-Hill, 1992.

[Bru97] R. Brun and F. Rademakers, Nuclear Instruments and Methods in Physics Research Section A: Accelerators, Spectrometers, Detectors and Associated Equipment 389(1 - 2) (1997) 81 – 86 *ROOT - An Object Oriented Data Analysis Framework*, new Computing Techniques in Physics Research V.

[Bur57] E. M. Burbidge, G. R. Burbidge, W. A. Fowler, and F. Hoyle, Rev. Mod. Phys. 29 (1957) 547–650 *Synthesis of the Elements in Stars.*

[Cad10] CadSoft, *Easily Applicable Graphical Layout Editor*, Website, 1988-2010, program available at `http://www.cadsoft.de`.

[Cam57] A. G. W. Cameron, *Stellar Evolution, Nuclear Astrophysics, and Nucleogenesis*, Chalk River Report CRL-41, 1957.

[Cla83] D. D. Clayton, *Principles of Stellar Evolution and Nucleosynthesis*, The University of Chicago Press, 1983.

[Cre11] Cremat, 2011, `http://www.cremat.com`.

[Cyg92] *Nova Cygni 1992 Photo from Hubble Space Telescope*, 1992, credit: NASA, ESA, HST, F. Paresce, R. Jedrzejewski (STScI).

[Das11] Dassault Systemes, *SolidWorks Lehr-Edition*, Website, 1995-2011, program available at `http://www.solidworks.de`.

[Deb79] K. Debertin, Nuclear Instruments and Methods 158(0) (1979) 479 – 486 *International Intercomparison of Gamma-Ray Emission-Rate Measurements by Means of Germanium Spectrometers and* ^{152}*Eu Sources.*

[Dev55] S. Devons, G. Manning, and D. S. P. Bunbury, Proceedings of the Physical Society. Section A 68(1) (1955) 18 *"Measurement of* γ *-Transition Lifetimes by Recoil Methods".*

[Doo10] P. Doornenbal, et al., Nuclear Instruments and Methods in Physics Research Section A: Accelerators, Spectrometers, Detectors and Associated Equipment 613(2) (2010) 218 – 225 *Lifetime Effects for High-Resolution Gamma-Ray Spectroscopy at Relativistic Energies and their Implications for the* $\{RISING\}$ *spectrometer.*

[Dun53] D. N. F. Dunbar, R. E. Pixley, W. A. Wenzel, and W. Whaling, Phys. Rev. 92 (1953) 649–650 *The 7.68-Mev State in* ^{12}C.

[Ebe96] J. Eberth, et al., Nuclear Instruments and Methods in Physics Research Section A: Accelerators, Spectrometers, Detectors and Associated Equipment 369(1) (1996) 135 – 140 *Encapsulated Ge Detectors: Development and Rirst Tests.*

[Ebe01] J. Eberth, et al., Progress in Particle and Nuclear Physics 46(1) (2001) 389 – 398 *MINIBALL A Ge Detector Array for Radioactive Ion Beam Facilities.*

[Eng71] R. Engmann, E. Ehrmann, F. Brandolini, and C. Signorini, Nuclear Physics A 162(2) (1971) 295 – 304 *Lifetime Measurements in sd Shell Nuclei: (V). Mean lives of* ^{31}S *and* ^{38}K *levels.*

[Fie10] J. Fiehl, *Calibration of a HPGe Detector and Geant4 Simulation for a Doppler Shift Attenuation Experiment*, Master's thesis, TU München, Physics Department, E12, Garching, Germany, 2010.

[Gei84] H. Geissel, et al., Nuclear Instruments and Methods in Physics Research Section B: Beam Interactions with Materials and Atoms 2(1 - 3) (1984) 770 – 773 *Influence of 1.3 MeV ^4He Post-Bombardment on the Depth Profiles of 35 keV ^3He Ions Implanted into Nb and Au.*

[H.-07] H.-Th. Janka and K. Langanke and A. Marek and G. Martnez-Pinedo and B. Müller, Physics Reports 442(16) (2007) 38 – 74 *Theory of Core-Collapse Supernovae.*

[Ham10] N. J. Hammer, H.-T. Janka, and E. Müller, The Astrophysical Journal 714(2) (2010) 1371 *Three-Dimensional Simulations of Mixing Instabilities in Supernova Explosions.*

[Har12] P. Hartung, *MLL Ground Plan*, 2012.

[Hei11] R. P. Heider, *Characterization of Three HPGe Detectors for a Doppler Shift Attenuation Experiment*, Master's thesis, TU München, Physics Department, E12, Garching, Germany, 2011.

[Her05] M. Hernanz, in J.-M. Hameury and J.-P. Lasota (editors), *The Astrophysics of Cataclysmic Variables and Related Objects*, volume 330 of *Astronomical Society of the Pacific Conference Series*, 265, 2005.

[Hoy54] F. Hoyle, The Astrophysical Journal Supplement 1 (1954) 121 *On Nuclear Reactions Occuring in Very Hot STARS.I. The Synthesis of Elements from Carbon to Nickel.*

[Ili02] C. Iliadis, A. Champagne, J. José, S. Starrfield, and P. Tupper, The Astrophysical Journal Supplement Series 142(1) (2002) 105 *The Effects of Thermonuclear Reaction-Rate Variations on Nova Nucleosynthesis: A Sensitivity Study.*

[Ili06] C. Iliadis, *Nuclear Physics of Stars*, WILEY-VCH Verlag GmbH & Co. KGaA, 2006.

[Ili10] C. Iliadis, R. Longland, A. Champagne, A. Coc, and R. Fitzgerald, Nuclear Physics A 841(1-4) (2010) 31 – 250 *Charged-Particle Thermonuclear Reaction Rates: II. Tables and Graphs of Reaction Rates and Probability Density Functions.*

[Jam04] F. James and M. Winkler, *MINUIT User's Guide*, 2004, MIGRAD CERN.

[Jos07] J. José and M. Hernanz, Journal of Physics G 34(12) (2007) R431 *Nucleosynthesis in Classical Nova Explosions.*

[Kan06] R. Kanungo, et al., Phys. Rev. C 74 (2006) 045803 *Lifetime of* ^{19}Ne* *(4.03 MeV).*

[Kno99] G. F. Knoll, *Radiation Detection and Measurement*, John Wiley & Sons, Inc, third edition, 1999.

[Kra87] K. S. Krane, *Introductory Nuclear Physics*, 1987.

[Kri85] J. E. Krizan, Phys. Rev. D 31 (1985) 3140–3143 *Relativistic Doppler-Shift Effects.*

[Lad06] C. J. Lada, The Astrophysical Journal Letters 640(1) (2006) L63 *Stellar Multiplicity and the Initial Mass Function: Most Stars Are Single.*

[Lod03] K. Lodders, The Astrophysical Journal 591(2) (2003) 1220 *Solar System Abundances and Condensation Temperatures of the Elements.*

[Lut11] R. Lutter, O. Schaile, S. K., Steinberger, and C. Broude, *MBS and ROOT Based Online/Offline Utility*, 2011, Marabou.

[McQ70] J. McQueen, J. Joyce, and E. Ludwig, Nuclear Physics A 151(2) (1970) 295 – 316 *The* (^3He,^4He) *Reaction with Nuclei in the s-d Shell.*

[Mes13] Mesytec, 2013, `http://www.mesytec.com`.

[Mic11] Micron, 2011, `http://www.micronsemiconductor.co.uk`.

[MLL08] MLL, *Jahresbericht*, 1992-2008.

[Mus88] G. Musiol, J. Ranft, R. Reif, and D. Seeliger, *Kern- und Elementarteilchenphysik*, VCH Weinheim, 1988.

[MW01] N. M. Weiss, *Nova Aquilae Illustration*, `http://chandra.harvard.edu/photo/2001/v1494aql`, 2001.

[Myt08] S. Mythili, et al., Phys. Rev. C 77 (2008) 035803 *Lifetimes of States in* ^{19}Ne *above the* ^{15}O + α *Breakup Threshold.*

[nud11] website, 2011, http://www.nndc.bnl.gov/nudat2.

[Pás81] F. Pászti, L. Pogány, G. Mezey, E. Kótai, A. Manuaba, L. Pócs, J. Gyulai, and T. Lohner, Journal of Nuclear Materials 98(1 - 2) (1981) 11 – 17 *Investigations on Blistering and Exfoliation in Gold by 3.52 MeV Helium Ions.*

[Phi76] G. W. Phillips and K. W. Marlow, Nuclear Instruments and Methods 137(3) (1976) 525 – 536 *Automatic Analysis of Gamma-Ray Spectra from Germanium Detectors.*

[Pow06] R. Powell, *Hertzsprung Russell Diagram*, Website, 2006, `http://www.atlasoftheuniverse.com`.

[Ras49] V. K. Rasmussen, C. C. Lauritsen, and T. Lauritsen, Phys. Rev. 75 (1949) 199 – 200 *Doppler Broadening of a Gamma-Ray Line.*

[Rol88] E. C. Rolfs and R. W. S., *Cauldrons in the Cosmos*, Chicago u.a., Univ. of Chicago Pr., 1988.

[RU09] I. C. for Radiation Units and Measurements, *Stopping of Ions Heavier Than Helium (Report 73)*, 2005/2009, http://www.icru.org/home/reports/stopping-of-ions-heavier-than-helium-report-73.

[Sal52] E. E. Salpeter, The Astrophysical Journal 115 (1952) 326–328 *Nuclear Reactions in Stars Without Hydrogen.*

[Sar82] D. Sargood, Physics Reports 93(2) (1982) 61 – 116 *Charged Particle Reaction Cross Sections and Nucleosynthesis.*

[Sch96] E. Schatzman, Annual Review of Astronomy and Astrophysics 34(1) (1996) 1–34 *The Desire to Understand the World.*

[Sch08] D. Schürmann, R. Kunz, I. Lingner, C. Rolfs, F. Schümann, F. Strieder, and H.-P. Trautvetter, Phys. Rev. C 77 (2008) 055803 *"Lifetime Measurement of the 6792 keV State in* ^{15}O*, Important for the Astrophysical S Factor Extrapolation in* $^{14}N(p,\gamma)^{15}O$*".*

[Sch11] O. Schaile, R. Lutter, S. K., Steinberger, and C. Broude, *HistPresent*, 2011.

[Sha97] A. W. Shafter, The Astrophysical Journal 487(1) (1997) 226 *On the Nova Rate in the Galaxy.*

[SLA09] SLAC, *High Energy Physics Representables Application*, 2009, hepRApp.

[Sne03] C. Sneden and J. J. Cowan, Science 299(5603) (2003) 70–75 *Genesis of the Heaviest Elements in the Milky Way Galaxy.*

[Soi10] S. Soisson, et al., Nuclear Instruments and Methods in Physics Research Section A: Accelerators, Spectrometers, Detectors and Associated Equipment 613(2) (2010) 240 – 244 *A Dual-Axis Dual-Lateral Position-Sensitive Detector for Charged Particle Detection.*

[Sol07] M. C. Solal, Nuclear Instruments and Methods in Physics Research Section A: Accelerators, Spectrometers, Detectors and Associated Equipment 572(3) (2007) 1047 – 1055 *The Origin of Duo-Lateral Position-Sensitive Detector Distortions.*

[Sta01] S. Starrfield, C. Iliadis, J. Truran, M. Wiescher, and W. Sparks, Nuclear Physics A 688(1 - 2) (2001) 110 – 117 *Nuclear Reaction Rates and the Nova Outburst.*

[Sta11] C. Stahl, *Winkel-Kontinuierliches DSAM: Lebensdauer-Messungen mit Ortssensitiven Detektorsystemen*, Master's thesis, TU Darmstadt, 2011.

[Tar03] O. Tarasov and D. Bazin, Nuclear Instruments and Methods in Physics Research Section B: Beam Interactions with Materials and Atoms 204(0) (2003) 174 – 178 *Development of the Program LISE: Application to Fusion Evaporation*, 14th International Conference on Electromagnetic Isotope Separators and Techniques Related to their Applications.

[Tar08] O. Tarasov and D. Bazin, Nuclear Instruments and Methods in Physics Research Section B: Beam Interactions with Materials and Atoms 266(19-20) (2008) 4657 – 4664 *LISE++: Radioactive Beam Production with In-Flight Separators*, proceedings of the XVth International Conference on Electromagnetic Isotope Separators an d Techniques Related to their Applications.

[Tho88] I. J. Thompson, Computer Physics Reports 7(4) (1988) 167 – 212 *Coupled Reaction Channels Calculations in Nuclear Physics.*

[Tho06] I. Thompson, *Coupled Reaction Channels Calculations*, 2006, fresco.

[Ton11] D. Tonev, et al., Journal of Physics: Conference Series 267(1) (2011) 012048 *Lifetime Measurements in Mirror Nuclei ^{31}S and ^{31}P: A Test for Isospin Mixing.*

[Wal54] M. Walker, Publications of the Astronomical Society of the Pacific 66 (1954) 230 *Nova DQ Herculis (1934): An Eclipsing Binary with Very Short Period.*

[Wim11] K. Wimmer, *Fresco Cross Section Calcucation: $^{32}S(^{3}He,^{4}He)^{31}S^{*}$*, 2011, private communication.

[Zie08] J. Ziegler, M. Ziegler, and J. Biersack, *The Stopping and Range of Ions in Matter*, 2008.

Acknowledgment

After years of working on this thesis, I want to thank everybody who contributed to the success of this project.

First of all, I want to thank my supervisor Prof. Ph.D. Shawn Bishop. He gave me the opportunity to work on a unique, challenging and interesting project by letting me build and commission a new experimental facility. He supported me in countless discussions and meetings to find solutions to just as many problems. Thank you!

I am grateful for the valuable support from my colleagues in the E12 chair. The office doors of Roman Gernhäuser, Thomas Faestermann and Jürgen Friese were always widely open and they were patient to discuss any kind of questions. The making of the experimental setup would not have been possible without the help and skills from Ralf Lang, Michael Klöckner and the staff of the central machine shop of the physics department. Thank you!

I also want to thank Dominik Seiler, Wolfgang Heimkes and especially Shavkat Akhmadaliev for the help with the complicated targets that were used for the commissioning experiment. Another ingredient for the successful experiment is the ion beam supply from the tandem accelerator. Thanks to Walter Carli, Peter Ring, and Wolfgang Hagn and all the operators and staff at the MLL Beschleunigerlabor this work became possible. Not to forget Rudi Lutter, who helped me so much with the data acquisition at the MLL and Christian Stahl for his help with the Geant4 simulation and the APCAD program. Thank you!

Thanks to everybody who helped me in the shifts during the beam times, had discussions about the problems in physics or off-topics or had a coffee with me, namely Michael Bendel, Vinzenz Bildstein, Michael Böhmer, Alan Chen, Thomas Dandl, Katrin Eppinger, Leticia Fimiani, José Manuel Gómez Guzmán, Karin Hain, Josef Homolka, Stefanie Klupp, Josef Lichtinger, Peter Ludwig, Ludwig Maier, Dennis Müchner, Katharina Nowak, Anuj Parikh, Georg Rugel, Konrad Steiger, Sigrid Weichs, Kathrin Wimmer, Max Winkel, Sonja Winkler and Petra Zweckinger.

I also want to thank former colleagues, advisers and supervisors Hendrik Schatz, Vladimir Henzl, Fernando Montes, Christoph Caesar and Karl-Ludwig Kratz, who had influence on my scientific development.

Finally, and maybe most important I want to thank my family and my friends - especially my wonderful girl friend Claire - who always supported me during all ups and downs on the path of this thesis work. I'm grateful that I'm part of your lives!

There are many more persons who supported me directly or indirectly, with and without my notice, with large effort or just with a smile. Thanks to all of you!